eXPRESS Polymer Letters Vol.3, No.6 (2009) 332
Available online at www.expresspolymlett.com
DOI: 10.3144/expresspolymlett.2009.41

Editorial corner – a personal view
Natural fibre reinforced polymer composites – are short natural fibres really reinforcements or just fillers?

*A. S. Luyt**

Department of Chemistry, University of the Free State (Qwaqwa Campus), Private Bag X13, Phuthaditjhaba, 9866, South Africa

Past research on natural fibre reinforced polymer composites, focused on the more well-known fibres e.g. wood, sisal, flax, hemp, jute, etc., but nowadays fibres are extracted from a large number of different plants. It is well-known that there is little interaction between untreated natural fibres and most synthetic polymers, and therefore fibre treatment, polymer modification and compatibilization have been investigated as means to improve polymer-fibre interaction to form an interphase that will induce effective stress transfer between the polymer and fibre.

When polymers are reinforced by long cellulosic fibres or fibre mats combined with effective treatment/modification of the fibre and/or polymer, most mechanical properties are significantly improved. This is, however, not necessarily true for polymers that are mixed with short fibres. Most publications that reported results on the properties of polymer composites containing untreated and treated short fibres, or on the influence of polymer modification or compatibilization on the composite properties, agree that treatment/modification/compatibilization generally improves polymer-fibre interaction with resultant improved mechanical properties. In many cases the reported properties were still worse than those of the neat polymer.

A number of papers, however, report considerably improved properties after polymer and/or fibre treatment. Many of these results are claimed to be related to transcrystallization of the polymer on the fibre surface as a result of the stronger interaction between the modified polymer and/or the treated fibre. There are, however, controversial views on the relationship between the thickness of the crystalline layer on the fibre surface and the effectiveness of stress transfer, and on the relationship between the extent of polymer crystallinity and the morphology of the interphase. Both these effects will determine whether there will be an improvement in mechanical properties, and whether the fibre may be regarded as a reinforcement of the polymer matrix. In many of the investigated systems, the treatment/modification/compatibilization is not effective enough in the creation of an interphase with the right lamellar architecture, and in these cases the fibre does not reinforce the polymer, but only act as a filler.

Prof. Dr. Riaan Luyt
Member of International Advisory Board

*Corresponding author, e-mail: luytas@qwa.ufs.ac.za

eXPRESS Polymer Letters Vol.3, No.6 (2009) 333–339
Available online at www.expresspolymlett.com
DOI: 10.3144/expresspolymlett.2009.42

Synthesis and properties on polyaniline in the presence of nickel chloride

*Y. Tan, Y. Zhang, J. Kan**

School of Chemistry and Chemical Engineering, Yangzhou University, Yangzhou, 225002, PR China

Received 18 January 2009; accepted in revised form 25 March 2009

Abstract. Both Conducting and Ferromagnetic polyaniline containing nickel (abbreviated as PANI-Ni) is synthesized in a solution containing aniline, HCl and $NiCl_2$, using peroxydisulphate as an oxidant and horseradish peroxidase as a catalyst. The conductivity of PANI-Ni is about 10^{-1} S cm^{-1}. The result of electron paramagnetic resonance (EPR) spectra indicated that there were unpaired electrons in PANI-Ni, and the spin density of the PANI-Ni was $1.09 \cdot 10^{19}$ spins g^{-1}. The plot of magnetization (M) against the magnetic field (H) indicated that the PANI-Ni was soft ferromagnetic at about 300 K, the saturation magnetization (M_s) and the coercive force (H_c) of which were 4.5 emu g^{-1} (electromagnetic unit per gram) and about 55 Oe, respectively. UV-Visible (UV-vis) and Fourier Transform Infrared (FTIR) spectra showed that there was strong interaction between Ni^{2+} and PANI chains, but the backbone chains of PANI-Ni were hardly changed compared with PANI. Cyclic voltammogram results indicated that the PANI-Ni film was of excellent electrochemical activity.

Keywords: *polymer synthesis, polyaniline, ferromagnetic, hysteresis loop, nickel*

1. Introduction

For many years chemists and physicists have striven to synthesize organic materials with both conducting and ferromagnetic properties due to their potential applications in batteries, electrical-magnetic shields, sensors and microwave-absorbants [1–3]. Several approaches such as electrochemical and in-situ chemical polymerizations have been reported to prepare conducting polymer with ferromagnetic property [4–7]. Wan and co-workers reported a method for synthesizing a composite of PANI/Fe_3O_4 with both conducting and ferromagnetic functions [8]. Aphesteguy *et al.* reported preparation and characterization of Ni-Gd ferrite polyaniline composite of both conducting and ferromagnetic characterizations [9]. Alam *et al.* reported the effect of ferrofluid concentration on electrical and magnetic properties of the Fe_3O_4/PANI nanocomposites [10]. As far as the composites were concerned, phase separation was a commonplace due to their poor compatibility between polymer matrix and inorganic particles [11]. Rajca and his colleagues reported a ferromagnetic phase below 10 K in a polymeric form of a high spin state aromatic molecule [12]. Recently Zaidi *et al.* reported the polymer of PANi-TCNQ (tetracyanoquinodimethane) produced from polyaniline and tetracyanoquinodimethane at ambient temperature. It is difficult to tell whether PANi-TCNQ is a polymer with both conducting and ferromagnetic properties because no conductivity data are available in the literature [13]. Ichinohe and co-workers reported that ferromagnetic poly(*m*-phenylenediamine) was synthesized by using H_2O_2 as an oxidant and horseradish peroxidase (HRP) as a catalyst in the mixture of aqueous buffer solution and 1,4-dioxane or in reversed micellar solution, and the obtained polymer was attracted to a permanent

*Corresponding author, e-mail: jqkan@yzu.edu.cn

magnet, but no conductivity data were available in the paper, either [14]. Niu and co-workers reported the oxidation of *m*-phenylenediamine by using H_2O_2 as an oxidant and horseradish peroxidase as a catalyst in 0.02 mol dm^{-3} B-R buffer solution, and 2,7-diaminophenazine was only obtained under the selected reaction condition [15]. We tried to duplicate the former results, however, only 2,7-diaminophenazine was still obtained and no precipitates were observed in the mixture of aqueous buffer solution and 1,4-dioxane.

Gosk and his colleagues reported that high-spin Fe^{3+} complex could be formed with imine and amine nitrogen in polyaniline [16]. Sun and co-workers presently reported that Co^{2+} ion might bind to more than one nitrogen site in a PANI chain or form inter-chain linkage among several adjacent PANI chains by coordination, and both intra-chain and inter-chain connections might lead to a more coil-like conformational change or a more twisted aggregation of PANI chains [17].

This paper will present a new and easy approach that synthesizes both conducting and ferromagnetic polyaniline with trace metal ions at ambient temperature. This is because there are unpaired electrons and vacant orbit in some metal ions [18] and donating ability of the lone-pair electrons on the nitrogen atom in conducting polyaniline chains [19]. When metal ions are added in the synthesized system of conducting polyaniline, the metal ions may interact with the nitrogen atoms in conducting polyaniline chains and form with both conducting and ferromagnetic polymers. The method is different from what Wan and co-workers described [8] and the resulting product is a complex rather than a composite entrapped with Fe_3O_4 as core and polyaniline as shell.

2. Experimental methods

2.1. Materials

The monomer aniline (reagent grade) was distilled into colorless under reduced pressure before use. Ammonium peroxydisulphate (APS), N,N-dimethylformamide (DMF) and other chemicals were reagent grade and used as received without further treatment. All of the aqueous solutions were prepared with double distilled water.

2.2. Polymerization

The PANI were synthesized in 0.1 dm^3 of solution containing 0.5 mol dm^{-3} HCl, 0.1 mol dm^{-3} aniline, 4 mg HRP, with and without 0.1 mol dm^{-3} $NiCl_2{\cdot}6H_2O$. APS of same molar ratio as aniline was added into the solution. The chemical polymerization of aniline was carried out for 24 hours at 30°C. The solution was stirred in an ultrasonic bath. The products were firstly separated by filtration, then washed with both double distilled water and ethanol, and finally dried at 65°C for 24 hours.

2.3. Analysis

The UV-vis spectra of all samples were obtained on UV-2550 spectrometer (Shimadzu) in the range of 250 ~ 900 nm. DMF was used as a solvent. Fourier Transform Infrared (FTIR) spectra were taken on a Tensor 27 FTIR spectrometer (Bruker) using KBr pellets at a resolution of 4 cm^{-1}. The morphologies of products were observed using a transmission electron microscope (TEM, TENCNAI-12). Conductivity of the resulting products was measured by using standard four-probe method. The standard deviation was less than 2.0% in our experiments using an YJ8312 model current source (Shanghai Huguang Instrument Works, China) and M92A digital multimeter (Mastech). Wide-angle X-ray diffraction patterns for the powder samples were taken on a M03XHF^{22} diffractometer (Mac Science, Japan) using Cu-K_α radiation (λ = 1.541 Å), which was used to analyze the crystallinity of polyaniline. The hysteresis loops were obtained on a Vibrating Sample Magnetometer (VSM, USA). The Electron Paramagnetic Resonance (EPR) spectra were carried out by using an A300-10/12 spectrometer (Bruker) operating in *X*-band (9.856 GHz). The microwave power was set at 0.2 mW and the amplitude was controlled at 2.00 G.. X-ray photoelectron spectroscopy (XPS) was performed with a VG EscaLab 220i spectrometer using a standard AlK_α X-ray source (300 W). The cyclic voltammogram (CV) was performed on a CHI 407 electroanalysis apparatus. An electrolytic cell for cyclic voltammetry consisted of a PANI working electrode, a platinum counter electrode and a saturated calomel electrode (SCE).

3. Results and discussion

3.1. Electrical and magnetic properties

Figure 1 shows the plots of magnetization (***M***) against the magnetic field (***H***) of PANI (curve a), deprotonated PANI with $NH_3 \cdot H_2O$ (curve b) and PANI-Ni (curve c), respectively. Curves (a) and (b) indicate that PANI and deprotonated PANI with $NH_3 \cdot H_2O$ are not ferromagnetic. Curve (c) clearly exhibits hysteresis loop at about 300 K, which indicates that the PANI-Ni is ferromagnetic. The inset in Figure 1 is ***M–H*** plot of $NiCl_2 \cdot 6H_2O$ under the same condition. It can be seen from the inset that the magnetization of $NiCl_2 \cdot 6H_2O$ increases linearly with increasing applied magnetic field and there is no hysteresis loop at ambient temperature, which imply that $NiCl_2 \cdot 6H_2O$ is just a paramagnetic salt. According to the result of XPS (Figure 2) of PANI-Ni, there is only trace amount of nickel in the PANI-Ni (<0.5%), so the nickel ions can't give noticeable contribution to the ferromagnetic property of the PANI-Ni. The result of EPR shows that there are unpaired electrons in the PANI-Ni and the spin density of the resulting product is $1.09 \cdot 10^{19}$ spins g^{-1}. It is well known that the ferromagnetic state not only requires (quasilocal) magnetic moments but also requires that the moments remain mutually aligned [20]. The results of VSM and EPR show that PANI-Ni is in keeping with the requirement of ferromagnetic state. The result of TEM in Figure 3 shows that the morphology of PANI-Ni (Figure 3b) is very similar with that of the PANI-Co, both of which are quasi-spherical morphologies. Sun and co-workers thought that Co^{2+} ion might bind to more than one nitrogen site in a PANI chain or form inter-chain linkage among several adjacent PANI chains by coordination, and both intra-chain and inter-chain connections might lead to a more coil-like conformational change or a more twisted aggregation of PANI chains [17]. It is deduced that the interaction between Ni^{2+} and PANI chains may be favorable to form ferromagnetic domain. The forming mechanism of conductive ferromagnetic PANI-Ni is suggested as Figure 4 [21]. However, more researches are needed to understand the behavior better.

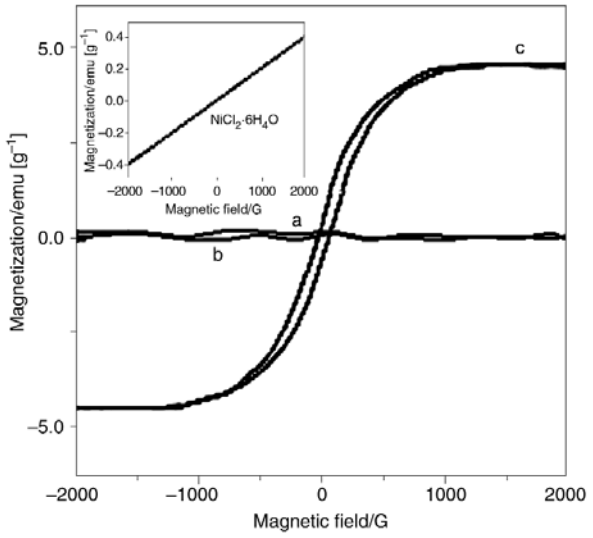

Figure 1. ***M-H*** plot of PANI (a), deprotonated PANI (b) and PANI-Ni (c)

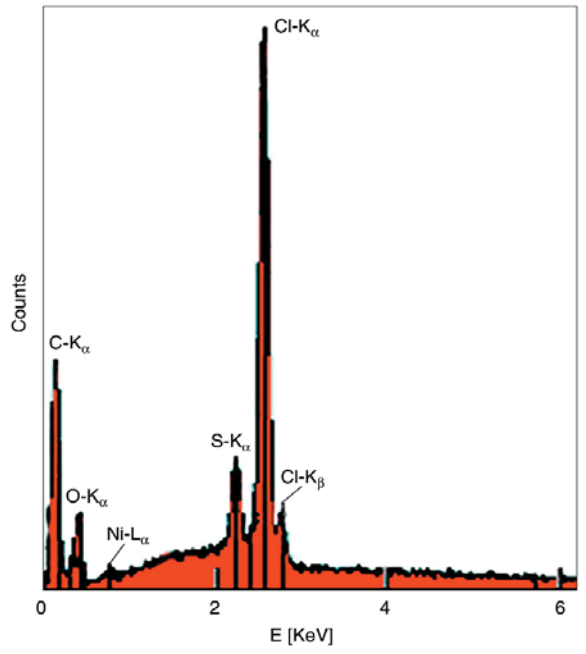

Figure 2. XPS spectrum of PANI-Ni

It is seen from Figure 1 that the saturation magnetization (M_s) and the coercive force (H_c) of the PANI-Ni are 4.5 emu g^{-1} (electromagnetic unit per gram) and about 55 Oe, respectively. The low coercive value implies that the PANI-Ni is a soft ferromagnetic material [14].

It is difficult to understand that the content of nickel in the resulting PANI is hardly related with the con-

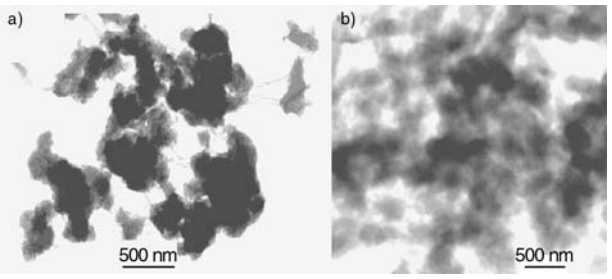

Figure 3. TEM morphology of PANI (a) and PANI-Ni (b)

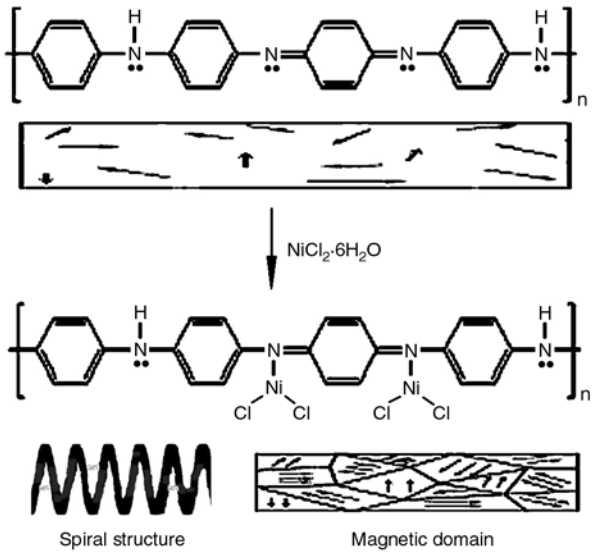

Figure 4. The possible forming mechanism of ferromagnetic PANI-Ni

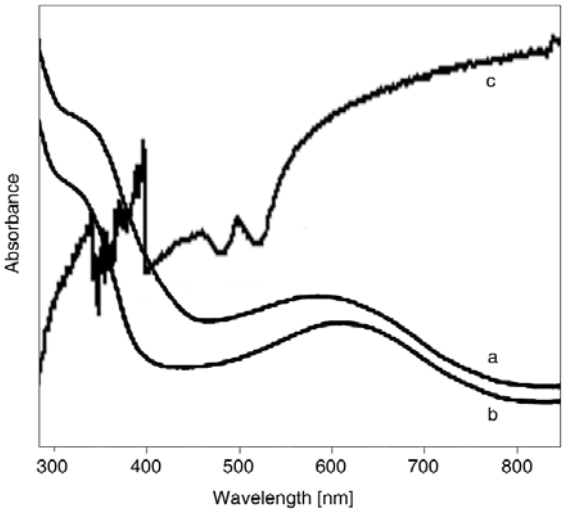

Figure 5. UV-vis spectra of PANI (a), PANI-Ni (b) and solid PANI (c)

centration of $NiCl_2$ in reaction system. We consider that this phenomenon can be easily explained with Peauson's theory of Hard and Soft acids and bases (HSAB), Hard acids prefer to bind to hard bases and soft acids prefer to bind to soft bases [22]. Based on similar system of HSAB's classification reported in the literature, H^+ [22] and PANI [23] are hard acid and hard base respectively, so PANI can be easily doped by H^+. Ni^{2+} is borderline acids [22], so PANI is just able to be coordinated with trace Ni^{2+} compared with H^+.

The conductivities of PANI-Ni and PANI are 0.22 and 0.13 S cm^{-1}, respectively. It indicates that Ni^{2+} has little effect on the conductivity of PANI.

As it is mentioned above, PANI-Ni is a conducting and ferromagnetic material at ambient temperature.

3.2. UV-vis spectra and FTIR spectra

Figure 5 is the UV-vis spectra of PANI (curve a), PANI-Ni (curve b) dissolved in DMF, and solid PANI (curve c), respectively. It is seen obviously from Figure 5a and Figure 5b that there are two absorption bands in the two curves: one location is ~350 nm and the other is ~600 nm. It was reported that PANI showed two strong absorptions at 320~340 and 600~660 nm respectively [24]. The first band was assigned as π-π^* transition and the other were associated with the transition of benzenoid rings into quinoid rings. In fact, the PANI we synthesized is in the protonated form, the absorption band of the transition of benzenoid rings into quinoid rings should be at more than 700 nm. This may be due to the presence of the hydrogen-bonding interaction of the C=O group in DMF with the NH group in PANI. Since the C=O group can interact or form hydrogen bond with the dopant, which could prevent the PANI from acid-doping [25]. This can be confirmed by a broad absorption band at more than 700 nm in the UV-vis spectrum of solid PANI (curve c).

Compared curve (b) with curve (a) in Figure 5, the peak of quinoid ring transition shifts from 585 to 621 nm when Ni^{2+} is added in the reactive system. The reason may be that 'compact coil' of PANI-Ni chain make the energy gap of quinoid ring transition narrower, thus transition of electrons becomes easier. The peak of π-π^* transition in PANI seldom shifts, so it can be inferred that the interaction of both Ni^{2+} and the nitrogen atoms on the quinoid ring is predominant.

Figure 6 shows the FTIR spectra of PANI (curve a) and PANI-Ni (curve b) respectively. IR spectra over 2500 cm^{-1} are omitted in Figure 6 because they are really identical with and without $NiCl_2$. 1570 and 1490 cm^{-1} are attributed to the stretching vibrations of N=Q=N ring and N–B–N ring respectively. The peak at 1300 cm^{-1} corresponds to C–N stretching vibration. The peaks at 1109 and 800 cm^{-1} can be attributed to bands characteristic of B–NH–Q or B–NH–B bonds, and out-of-plane bending vibration of C–H of benzene rings (where B refers to the benzenic-type rings and Q refers to

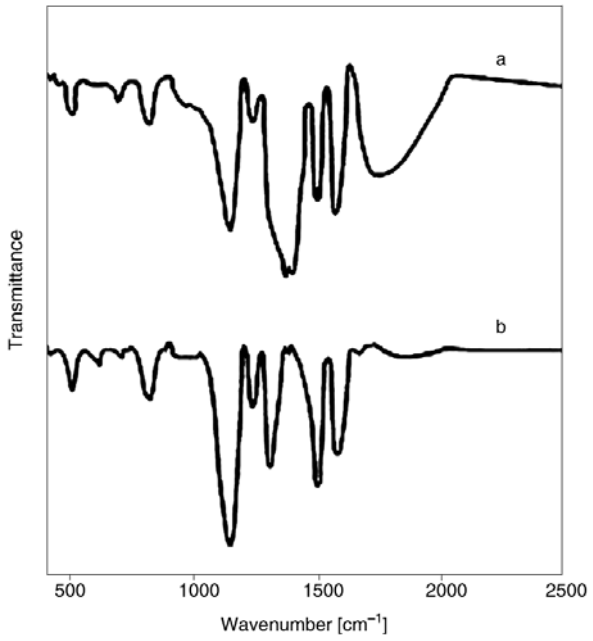

Figure 6. FTIR spectra of PANI-Ni (a) and PANI (b)

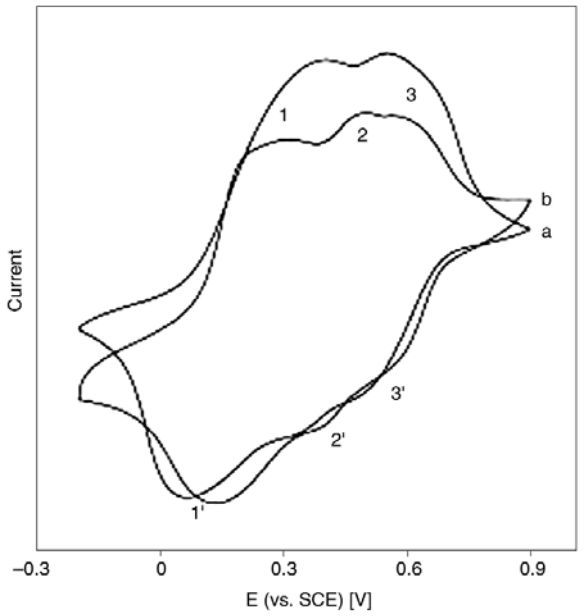

Figure 7. The cyclic voltammograms of PANI (a) and PANI-Ni film (b) 0.5 mol dm^{-3} HCl, 60 mV/s

the quinonic-type rings) [24, 26, 27]. It is confirmed by our result (as shown in Figure 6) that band at 1400 cm^{-1} assigned to N–H bending mode shifts to 1303 cm^{-1} when Ni^{2+} is added in the reactive system of PANI, which indicates that the Ni^{2+} can interact with nitrogen atoms of the PANI chains.

It can be inferred from the results of UV-vis and FTIR spectra that backbone chain of PANI-Ni hardly changes compared with that of PANI. So the PANI-Ni is a complex polymer under the aforementioned condition.

3.3. Cyclic voltammogram

Figure 7 is the cyclic voltammogram of PANI film (curve b) and PANI-Ni film (curve a) in 0.5 mol dm^{-3} HCl aqueous solution in the range from –0.2 to 0.9 V at 60 mV·s^{-1}. It can be seen obviously from Figure 7 that the PANI-Ni is of electrochemical activity.

There are three pairs of redox peaks in the two curves. Peaks 1 and 3 have been identified as oxidation of PANI to its radical cation (polaron) and further oxidation to quinoid (bipolaron) states, respectively [28]. Peaks 1′ and 3′ correspond to the inverse process of Peaks 1 and 3 [29, 30]. The 'middle' peaks 2 and 2′ have been attributed to the presence of ortho-coupled polymers [31] and the degradation of PANI (soluble species such as benzoquinone and hydroquinone) [28].

Compared curve (b) with curve (a), the two curves are similar in shape. The oxidation-reduction peaks show slight shifts. For example, the anodic peaks at 0.05 and 0.33 V for PANI film shift to 0.13 and 0.40 V for the PANI-Ni, respectively. These shifts may result from the interaction between Ni^{2+} and PANI chains.

3.4. X-ray diffraction spectra

Figure 8 shows the XRD patterns of $NiCl_2{\cdot}6H_2O$ (curve c) and PANI (curve b) and PANI-Ni (curve a). The X-ray diffractogram of $NiCl_2{\cdot}6H_2O$ (curve c) indicates the characteristic diffraction peaks of $NiCl_2{\cdot}6H_2O$ centered at $2\theta = 16.5$, 18.6, 29.2, 32.8, 35.5, 37.5°. However, these diffraction peaks didn't appear in the XRD patterns of PANI-Ni. This may be because there is only trace amount of nickel in PANI-Ni. The PANI (curve a) and PANI-Ni (curve b) have a broad hump peak at $2\theta = 20°$, which shows that PANI-Ni is an amorphous polymer [32]. This result is in agreement with those reported in literature [33]. Based on the similar diffractogram of curves (a) and (b) in Figure 8, it maybe because there is hardly effect of Ni^{2+} on the crystallinity of PANI-Ni.

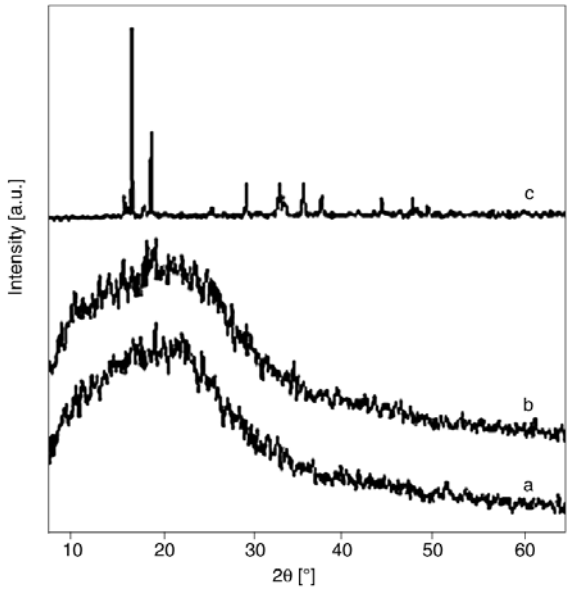

Figure 8. XRD pattern of PANI-Ni (a), PANI (b) and $NiCl_2 \cdot 6H_2O$(c)

4. Conclusions

The conductive and ferromagnetic PANI-Ni is synthesized successfully in the system containing $NiCl_2$ at ambient temperature. The result of VSM indicates that PANI-Ni is of ferromagnetism at about 300 K. The UV-vis and FTIR spectra show that the structure of backbone chains of PANI-Ni hardly changes compared with PANI. The PANI-Ni is a complex polymer rather than a composite.

Acknowledgements

This project was supported by National Science Foundation of China (No.20673095).

References

[1] Shen P. K., Huang H. T., Tseug A. C. C.: A study of tungsten trioxide and polyaniline composite films. Journal of The Electrochemical Society, **139**, 1840–1845 (1992).
DOI: 10.1149/1.2069508

[2] Kawaguch H.: Functional polymer microspheres. Progress in Polymer Science, **25**, 1171–1210 (2000).
DOI: 10.1016/S0079-6700(00)00024-1

[3] Kalinina O., Kumacheva E.: A 'core-shell' approach to producing 3D polymer nanocomposites. Macromolecules, **32**, 4122–4129 (1999).
DOI: 10.1021/ma981583o

[4] Bidan G., Jarjayes O., Fruchart J. M., Hannecart E.: New nanocomposites based on 'tailor dressed' magnetic particles in a polypyrrole matrix. Advanced Materials, **61**, 52–155 (1994).
DOI: 10.1002/adma.19940060213

[5] Yan F., Xue G., Chen J.: Lu Y.: Preparation of a conducting polymer/ferromagnet composite film by anodic-oxidation method. Synthetic Metals, **123**, 17–20 (2001).
DOI: 10.1016/S0379-6779(00)00572-5

[6] Liu J., Wan M. X.: Composites of polypyrrole with conducting and ferromagnetic behaviors. Journal of Polymer Science Part A: Polymer Chemistry, **38**, 2734–2739 (2000).
DOI: 10.1002/1099-0518(20000801)38:15<2734::AID-POLA130>3.0.CO;2-R

[7] Wan M., Li J. C.: Synthesis and electrical-magnetic properties of polyaniline composites. Journal of Polymer Science Part A: Polymer Chemistry, **36**, 2799–2805 (2003).
DOI: 10.1002/(SICI)1099-0518(19981115)36:15<2799::AID-POLA17>3.0.CO;2-1

[8] Wan M., Li W.: A composite of polyaniline with both conducting and ferromagnetic functions. Journal of Polymer Science Part A: Polymer Chemistry, **35**, 2129–2136 (1997).
DOI: 10.1002/(SICI)1099-0518(199708)35:11<2129::AID-POLA2>3.0.CO;2-T

[9] Aphesteguy J. C., Bercoff P. G., Jacobo S. E.: Preparation of magnetic and conductive Ni–Gd ferrite-polyaniline composite. Physica B: Physics of Condensed Matter, **398**, 200–203 (2007).
DOI: 10.1016/j.physb.2007.04.018

[10] Alam J., Riaz U., Ahmad S.: Effect of ferrofluid concentration on electrical and magnetic properties of the Fe_3O_4/PANI nanocomposites. Journal of Magnetism and Magnetic Materials, **314**, 93–97 (2007).
DOI: 10.1016/j.jmmm.2007.02.195

[11] Wang H., Xu P., Meng S., Zhong W., Du W., Du Q.: Poly(methylmethacrylate)/silica/titania ternary nanocomposites with greatly improved thermal and ultraviolet-shielding properties. Polymer Degradation and Stability, **91**, 1455–1461 (2006).
DOI: 10.1016/j.polymdegradstab.2005.10.008

[12] Rajca A., Wongsriratanakul J., Rajca S.: Magnetic ordering in an organic polymer. Science, **294**, 1503–1505 (2001).
DOI: 10.1126/science.1065477

[13] Zaidi N. A., Giblin S. R., Terry I. Monkman A. P.: Room temperature magnetic order in an organic magnet derived from polyaniline. Polymer, **45**, 5683–5689 (2004).
DOI: 10.1016/j.polymer.2004.06.002

[14] Ichinohe D., Muranaka T., Kise H.: Oxidative polymerization of phenylenediamines by enzyme and magnetic properties of the products. Journal of Applied Polymer Science, **70**, 717–721 (1998).
DOI: 10.1002/(SICI)1097-4628(19981024)70:4<717::AID-APP11>3.0.CO;2-U

[15] Niu S. Y., Jiao K.: Studies on the oxidation of m-phenlene diamine by H_2O_2 catalyzed by horseradish peroxidase. Acta Chimica Sinica, **58**, 617–621 (2000).
[16] Gosk J. B., Kulszewicz-Bajer I., Twardowski A.: Magnetic properties of polyaniline doped with $FeCl_3$. Synthetic Metals, **156**, 773–778 (2006).
DOI: 10.1016/j.synthmet.2006.02.003
[17] Tao S., Hong B., Kerong Z.: An infrared and Raman spectroscopic study of polyanilines co-doped with metal ions and H^+. Spectrochimica Acta Part A: Molecular and Biomolecular Spectroscopy, **66**, 1364–1368 (2007).
DOI: 10.1016/j.saa.2006.08.011
[18] Xiao H-P., Morsali A.: A new three-dimensional polymeric Pb^{II} complex involving holo- and hemidirected coordination spheres. Solid State Sciences, **9**, 155–158 (2007).
DOI: 10.1016/j.solidstatesciences.2006.09.005
[19] Trivedi D. C.: Observation of ferromagnetism in polyaniline. Synthetic Metals, **121**, 1780–1781 (2001).
DOI: 10.1016/S0379-6779(00)00759-1
[20] Billas I. M. L., Chatelain A., de Heer W. A.: Magnetism from the atom to the bulk in iron, cobalt, and nickel clusters. Science, **265**, 1682–1684 (1994).
DOI: 10.1126/science.265.5179.1682
[21] Zhang Y., Zhu C., Kan J.: Synthesis and characterization of ferromagnetic polyaniline with conductivity in an applied magnetic field. Journal of Applied Polymer Science, **109**, 3024–3029 (2008).
DOI: 10.1002/app.28414
[22] Pearson R. G.: Hard and soft acids and bases, Part I: Fundamental principles. Journal of Chemical Education, **45**, 581–587 (1968).
[23] Chehimi M. M., Abel M-L., Perruchot C., Delamar M., Lascelles S. F., Armes S. P.: The determination of the surface energy of conducting polymers by inverse gas chromatography at infinite dilution. Synthetic Metals, **104**, 51–59 (1999).
DOI: 10.1016/S0379-6779(99)00040-5
[24] Laska J., Widlarz J.: Spectroscopic and structural characterization of low molecular weight fractions of polyaniline. Polymer, **46**, 1485–1495 (2005).
DOI: 10.1016/j.polymer.2004.12.008
[25] Chen S. A., Lee H. T.: Polyaniline plasticized with 1-methyl-2-pyrrolidone: Structure and doping behavior. Macromolecules, **26**, 3254–3261(1993).
DOI: 10.1021/ma00065a002
[26] Zeng X-R., Ko T-M.: Structure - conductivity relationships of iodine-doped polyaniline. Journal of Polymer Science: Part B: Polymer Physics, **35**, 1993–2001 (1997).
DOI: 10.1002/(SICI)1099-0488(19970930)35:13<1993::AID-POLB1>3.0.CO;2-O
[27] Cheng D. M., Ng S. C., Chan H. S. O.: Morphology of polyaniline nanoparticles synthesized in triblock copolymers micelles. Thin Solid Films, **477**, 19–23(2005).
DOI: 10.1016/j.tsf.2004.08.105
[28] Shim Y-B., Won M-S., Park S-M.: Electrochemistry of conductive polymers VIII: In situ spectroelectrochemical studies of polyoniline growth mechanisms. Journal of The Electrochemical Society, **137**, 538–544 (1990).
DOI: 10.1149/1.2086494
[29] Stilwell D. E., Park S. M.: Electrochemistry of conductive polymers II. Electrochemical studies on growth properties of polyaniline. Journal of the Electrochemical Society, **135**, 2254–2262 (1988).
DOI: 10.1149/1.2096248
[30] Yan B., Yang J., Li Y., Cao Y.: Electrochemical adsorption of hydrogen and various ions on polyaniline film. Reactions concerning the first pair of cyclic voltammetric peaks. Synthetic Metals, **44**, 189–197 (1991).
DOI: 10.1016/0379-6779(91)91834-W
[31] Hand R. L., Nelson R. F.: Anodic oxidation pathways of N-alkylanilines. Journal of the American Chemical society, **96**, 850–860 (1974).
DOI: 10.1021/ja00810a034
[32] Yavuz O., Ram M. K., Aldissi M., Poddar P., Hariharan S.: Synthesis and the physical properties of MnZn ferrite and NiMnZn ferrite-polyaniline nanocomposite particles. Journal of Materials Chemistry, **15**, 810–817 (2005).
DOI: 10.1039/b408165j
[33] Pouget J. P., Jozefowicz M. E., Epstein A. J., Tang X., MacDiarmid A. G.: X-ray structure of polyaniline. Macromolecules, **41**, 723–789 (1991).
DOI: 10.1021/ma00003a022

eXPRESS Polymer Letters Vol.3, No.6 (2009) 340–351
Available online at www.expresspolymlett.com
DOI: 10.3144/expresspolymlett.2009.43

Relationships between nanostructure and dynamic-mechanical properties of epoxy network containing PMMA-modified silsesquioxane

S. Zaioncz[1], K. Dahmouche[2], C. M. Paranhos[1,2], R. A. S. San Gil[3], B. G. Soares[1]*

[1]Instituto de Macromoléculas, Universidade Federal do Rio de Janeiro Centro de Tecnologia, Bloco J, Ilha do Fundão, 21945-970, Rio de Janeiro, P.O.Box 68525, RJ, Brazil
[2]Universidade Estadual da Zona Oeste, Rio de Janeiro, RJ, Brazil
[3]Instituto de Quimica, Universidade Federal do Rio de Janeiro, RJ, Brazil

Received 24 January 2009; accepted in revised form 28 March 2009

Abstract. A new class of organic-inorganic hybrid nanocomposites was obtained by blending PMMA-modified silsesquioxane hybrid materials with epoxy matrix followed by curing with methyl tetrahydrophthalic anhydride. The hybrid materials were obtained by sol-gel method through the hydrolysis and polycondensation of the silicon species of the hybrid precursor, 3-methacryloxypropyltrimethoxysilane (MPTS), simultaneously to the polymerization of the methacrylate (MMA) groups covalently bonded to the silicon atoms. The nanostructure of these materials was investigated by small angle X-ray scattering (SAXS) and correlated to their dynamic mechanical properties. The SAXS results revealed a hierarchical nanostructure consisting on two structural levels. The first level is related to the siloxane nanoparticles spatially correlated in the epoxy matrix, forming larger hybrid secondary aggregates. The dispersion of siloxane nanoparticles in epoxy matrix was favored by increasing the MMA content in the hybrid material. The presence of small amount of hybrid material affected significantly the dynamic mechanical properties of the epoxy networks.

Keywords: *nanocomposites, epoxy, SAXS, sol-gel, dynamic-mechanical properties*

1. Introduction

Epoxy resins are widely used thermosets in several industrial applications because of their high mechanical and adhesion characteristics associated to the good chemical resistance. However their brittleness limits some important applications mainly as high performance adhesives and composites. The incorporation of liquid rubber components constitutes a usual approach for improving toughness of these materials, but with frequent detriment of stiffness and modulus [1–6]. The increased demand for higher performance materials which combine improved strength, hardness, toughness and heat resistance has motivated several investigations on the field of organic/inorganic nano-hybrid materials. The nano-sized inorganic fillers incorporated into an epoxy matrix are expected to provide a synergistic combination of individual organic/inorganic component properties, thanks to the dramatic increase of the interface area between the components [7–8]. Moreover, the dispersion of the filler in nano-size dimensions may also provide a homogeneous morphology throughout the composite, which greatly improves the reproducibility of its properties [9–10].

Among several inorganic nano-particles that can be incorporated into the epoxy resin, those constituted by polyhedral oligomeric silsesquioxane (POSS)

*Corresponding author, e-mail: bluma@ima.ufrj.br

have been emerging as a new and versatile technology because of the simplicity of their synthesis and processing. Moreover they offer a unique opportunity for preparing truly dispersed nanocomposites [10–12]. POSS is a class of important nanosized cage-like compounds, obtained by a sol-gel process involving hydrolysis and condensation of trialkoxy silanes bearing an organic group [13–16]. Depending on the reaction parameters it is possible to obtain molecules with different structures. Additionally, the POSS structure may be completely condensed, presenting a cube octameric framework constituted by an inorganic core formed by silica and surrounding by eight organic corner groups or be partially condensed, presenting some hydroxyl groups [17, 18]. The nature of the *R* groups is very important to provide good interaction between the filler and the epoxy matrix, which in turn affects the degree of dispersion, the local structure and mobility of the polymer chains. Consequently an improvement of thermal, oxidative and dimensional stability as well as mechanical performance of many polymeric resins is usually achieved. Mono- and multi-functionalized silsesquioxanes containing epoxy [7, 19–27], amino [28–32], mercapto [33], maleimido [34, 35], and isocyanate groups [36] have been successfully employed in the preparation of epoxy resin-based hybrid materials. Mono-functionalized silsesquioxanes are prepared by corner capping reaction of a trisilanol with a functionalized trialkoxy silane, and results in POSS molecules grafted onto the epoxy matrix [14]. Polyfunctional POSS is obtained from the hydrolysis/condensation of a functionalized trialkoxi silane resulting in polymer networks with the POSS cage acting as a crosslinking site [7]. Epoxy resin/POSS hybrid materials are prepared by mixing both components [23] or by performing the hydrolysis/condensation of the silane precursor in the presence of the epoxy matrix. When the POSS molecule is prepared in situ, the inorganic siloxane particles are more linked with the epoxy network because the alkoxy groups of the silane precursor can react with the hydroxyl groups formed by the ring opening reaction of the epoxy groups, through an ether exchange reaction [20].

Inorganic-organic hybrid compounds constituted by siloxane particles chemically linked to another polymer that is miscible with the epoxy matrix is also a good strategy for the development of new nanostructured epoxy hybrid networks. In this sense, an interesting family that fulfills this requirement is that obtained from the copolymerization between a vinyl-functionalized trialkoxysilane precursor and methyl methacrylate (MMA). Hybrid compounds have been prepared by different methodologies to develop materials with adjustable transparency, refractive index and hardness [37–40]. However, to the best of our knowledge, there are no reports in the accessible literature, regarding its use as epoxy modifier.

The present work aims for the first time to study the effect of Silsesquioxane-PMMA hybrid materials (SSO-PMMA) on the nanostructural features of the epoxy networks. The hybrid materials were synthesized by the hydrolysis/condensation of the (3-methacryloxypropyl) trimethoxy silane (MPTS) precursor simultaneously to its free radical copolymerization with methyl methacrylate. This process gives rise to a crosslinked hybrid compound with the PMMA chains surrounding the inorganic siloxane particles [41–43]. This structural feature contributes for a better filler-epoxy matrix interaction since the PMMA chains chemically linked to the silsesquioxane moiety can physically interact with the epoxy matrix, providing a good anchorage between the components. Moreover, when the MMA is employed as the co-monomer, their chains help to keep the inorganic particle away from each other, decreasing the chance of filler aggregation. The nanoscopic features of the epoxy network modified with these hybrid materials were determined by small angle X-ray scattering (SAXS) and were related to the dynamic mechanical properties.

2. Experimental

2.1. Materials

3-methacryloxypropyltrimethoxysilane (MPTS) was purchased from Fluka and used without further purification. The monomers methyl methacrylate (MMA) was obtained from Methacryl do Brasil S.A. and distilled under reduced pressure. Benzoyl peroxide (BPO), supplied by Vetec Ind. Quim. Ltda (Rio de Janeiro, Brazil) was used as the free radical initiator, and was recrystallized from chloroform/ether. The epoxy resin used in this study was diglycidyl ether of bisphenol-A (DGEBA), DER 331 (Dow Chemical) and presents the following characteristics: $<M_n>$ = 384; viscosity = 12,000 mPa·s;

epoxide equivalent = 192 g·eq^{-1}. Methyl tetrahydro phthalic anhydride (Aradur HY 2123) used as the curing agent was supplied by Hunstman (São Paulo, Brazil). This agent contains 2% in weight of 2-ethyl-4-methyl-imidazole, used as catalyst of the curing process.

2.2 Synthesis of Silsesquioxane-PMMA hybrid materials

0.4 g (1.68 mmol) of MPTS was mixed with 0.2 ml of ethanol containing 0.10 ml of concentrated hydrochloric acid. This proportion corresponds to a H_2O/MPTS molar ratio of 3:1 and a pH of solution of 1.0. Then, desired amounts of MMA and BPO were added into the flask. (The amount of BPO related to the vinyl monomer content was 3 mol%). The reaction medium was stirred at 45°C for 144 h, until gelation. The ethanol and H_2O used as solvents, the methanol produced from the silane precursor condensation, as well as the remaining non reacted MMA monomers were removed under vacuum, and the resulting monolithic dried gel was milled and stored under nitrogen. Table 1 presents the Silsesquioxane-PMMA compositions obtained theoretically from the initial formulations. The values are close to those obtained experimentally from TGA measurements, which were also presented in the same table.

2.3. Preparation of epoxy-based nanocomposites

6 parts of Silsesquioxane-PMMA was dispersed into 100 parts of anhydride used as the hardener, at 50°C under intensive mixing. Then, 100 parts of DGEBA was added. The mixture was stirred, degassed, poured into an open silicon mold and cured at 80°C for 3 h, followed by a post curing treatment at 110°C for 3 h.

2.4. Characterization and testing

^{29}Si MAS solid state nuclear magnetic resonance (NMR) spectra of the hybrid materials were recorded on a Bruker DRX-300 (7.05 Tesla) spectrometer equipped with an 4 mm ZrO_2 rotor, operating at 4000 Hz and 1000 scans. The chemical shifts positions are referenced to kaolinite.

Dynamic mechanical analyzer (Q-800, TA Scientific) was employed for measuring dynamic mechanical properties of cured epoxy networks, at a fixed frequency of 10 Hz, with a heating rate of 3°C/min. A single cantilever clamp was used for samples of size 25×10×2 mm^3.

Thermogravimetric analysis was performed on a Q-50 thermogravimetric analyzer, TA Scientific, operating from 30 to 750°C, under nitrogen atmosphere and a heating rate = 5°C·min^{-1}.

The Small Angle X-ray Scattering (SAXS) study was performed at room temperature using synchrotron the beam line of National Synchrotron Light Laboratory (LNLS), Campinas, Brazil. This beamline is equipped with an asymmetrically cut and bent silicon (111) monochromator that yielded a monochromatic (λ = 1.608 Å) and horizontally focused beam. A position sensitive X-ray detector and a multichannel analyzer were used to record the SAXS intensity, $I(q)$, as a function of modulus of scattering vector q, $q = (4\pi/\lambda)\sin(\theta/2)$, θ being the scattering angle. Each SAXS pattern corresponds to a data collection time of 900 s.

3. Results and discussion

3.1. Condensation degree of silicon species in POSS-PMMA hybrid materials

The hydrolysis/condensation of MPTS simultaneously to the free radical copolymerization of MPTS and MMA gives rise to a crosslinked hybrid structure as illustrated in Figure 1 [42, 43]. The structural features of the silsesquioxane moieties of the Silsesquioxane-PMMA (SSO-PMMA) hybrids prepared in this study were investigated by ^{29}Si MAS

Table 1. Composition Silsesquioxane-PMMA hybrid materials

Code	MPTS		MMA		BPO [mmol]	Silsesquioxane-PMMA composition		
	[g]	[mmol]	[g]	[mmol]		Siloxane [%]	PMMA [%]	Siloxane [%] from TGA
PM1	0.4	1.68	0.00	0.0	0.05	44	56	38.7
PM2	0.4	1.68	0.34	3.4	0.15	20	80	18.4
PM3	0.4	1.68	0.68	6.8	0.25	14	86	13.9
PM4	0.4	1.68	1.36	13.6	0.45	8	92	10.2

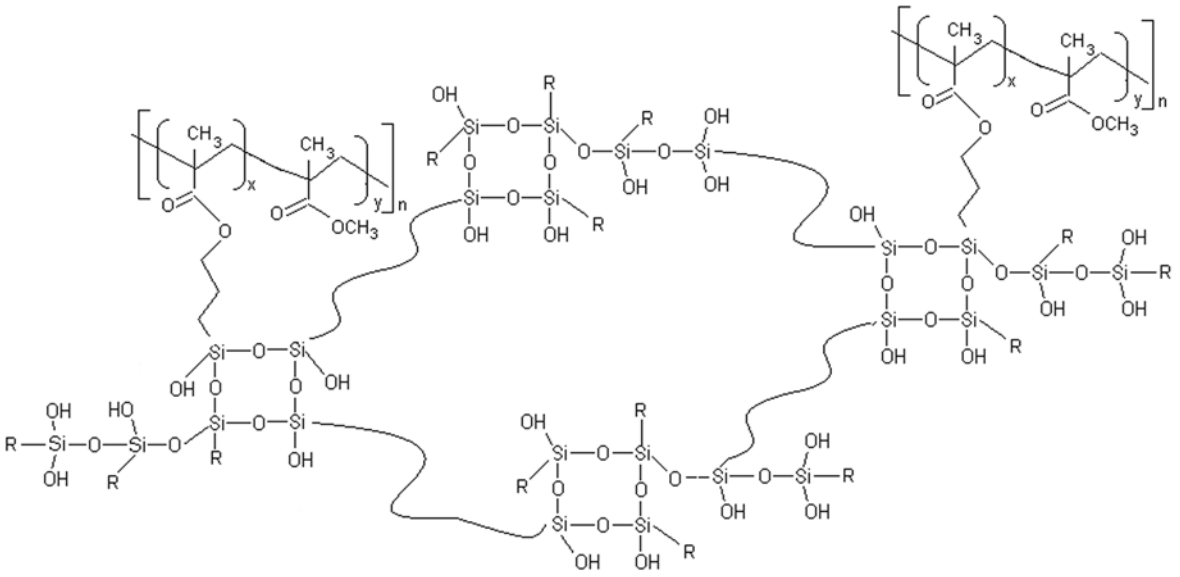

Figure 1. Proposal structure for the Silsesquioxane-PMMA hybrid material

solid state NMR spectroscopy. Figure 2 presents a typical spectrum of the hybrid compound containing 56% of MMA (PM1).

The MMA content in the PM1 comes from the methacrylate moiety in the silane precursor, since there was no added MMA. The different species are identified according to the conventional T^n notation, where T designs the trifunctional units and n corresponds to the number of neighboring silicon interconnected through the oxygen atoms of the first sphere of coordination [20, 44]. Therefore, T^0, T^1 and T^2 design the non condensed, monomeric and dimeric species, respectively, while the T^3 units refer to the completely condensed species. The ^{29}Si NMR spectra exhibits three resonance peaks at around –50 ppm, –59 ppm and –66 ppm associated to the presence of T^1 [$RSi(OSi)(OH)_2$], T^2 [$RSi(OSi)_2(OH)$] and T^3 [$RSi(OSi)_3$], respectively. Table 2 presents the proportion of the Si in different environment together with the degree of condensation. The degree of condensation (D) is given by Equation (1):

$$D\,[\%] = \frac{1}{3}T^1 + \frac{2}{3}T^2 + \frac{3}{3}T^3 \qquad (1)$$

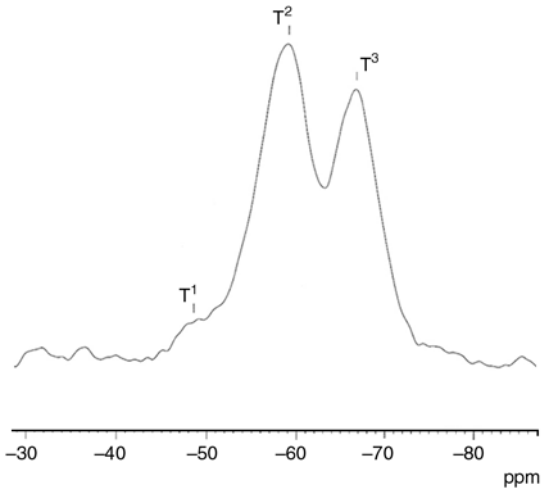

Figure 2. ^{29}Si MAS NMR spectrum of the Silsesquioxane-PMMA hybrid compound containing 56% of MMA (PM1)

All hybrid materials present a high amount of silicon as dimeric species (high T^2 amount), that is, high amount of silicon bearing one hydroxyl group, indicating that the silsesquioxane prepared in this work is partially condensed. It is important to point out that the copolymerization with MMA resulted in a significant increase of the fraction of monomeric T^1 species and a pronounced decrease of the proportion of T^3 species, resulting on a

Table 2. Peak area of T^1, T^2 and T^3 species in Silsesquioxane-PMMA hybrid material, determined from ^{29}Si MAS solid state NMR spectroscopy

Code	Silsesquioxane-PMMA composition		^{29}Si solid state NMR area [%]			Degree of condensation [%]
	Siloxane [%]	PMMA [%]	T^1	T^2	T^3	
PM1	44	56	6	53	41	79
PM3	14	86	18	61	21	68

decrease of the average condensation degree (Table 2). It is well known that acid pH conditions, as used in this study, promote hydrolysis of silicon alkoxydes but inhibit polycondensation between hydrolyzed species [45]. As a consequence, during the synthesis of Silsesquioxane-PMMA hybrids the hydrolysis of the methoxy groups of the MPTS precursor occurs firstly, but the condensation of the hydroxyl groups is slower than the free radical polymerization of MMA [46]. Therefore, the PMMA chains linked to the inorganic siloxane particles exert some hindrance towards the –SiOH condensation.

3.2. Nanostructural characterization of the epoxy-based hybrid nanocomposites

The epoxy resin was modified with SSO-PMMA hybrid compound with different compositions as described in Table 1. The epoxy network modified with the hybrid materials were transparent indicating no discernible phase separated morphology, regardless the hybrid composition. This behavior suggests that the SSO-PMMA hybrid materials are dispersed inside the epoxy matrix in nanometric dimension.

SAXS technique is a very important tool for characterizing the nanoscopic structure of complex systems containing nanoparticles and their aggregates and/or agglomerates and provides information regarding hierarchical structures and particle size distribution [47, 48]. This technique was employed in this work to investigate the nanostructure of the epoxy-based composites.

3.2.1. Method of SAXS analysis

Both asymptotic q-dependences, at low and high q, of the scattering intensity produced by a dilute set of isolated particles with no long-range correlation embedded in a homogeneous matrix having a sharp and locally flat interface, are known. In the low q region, the scattering intensity produced by N isolated nanoparticles is described by the Guinier law described by Equation (2):

$$I(q) = G\exp\left(\frac{-q^2R_g^2}{3}\right) \tag{2}$$

where R_g is the radius of gyration of the particles and G is given by Equation (3):

$$G = N(\rho_p - \rho_m)^2 v^2 \tag{3}$$

where ρ_p and ρ_m are the average electron densities of the particles and the matrix, respectively, and v the average particle volume.

At high q region Porod's law holds, see Equation (4):

$$I(q) = Aq^{-P} \tag{4}$$

where $A = 2\pi(\rho_P - \rho_m)^2 S$, S being the interface area between particles and matrix and P an exponent that depends of the sharpness of the interface and on the detailed geometry of the particles [48].

Dilute systems with nano-objects with different complex shapes and some polydispersivity yield a scattering intensity function $F(q)$ also obeying both Guinier and Porod laws over the low and high q ranges, respectively. A semi-empirical equation proposed by Beaucage [49] that applies to the whole scattering curves and have both asymptotic behaviours described above is given by Equation (5):

$$F(q) = G\exp\left(\frac{-q^2R_g^2}{3}\right) + B\left[\frac{\left(erf\left(\frac{qR_g}{2.499}\right)\right)^3}{q}\right]^P \tag{5}$$

In Equation (5), the asymptotic Guinier and Porod laws are merged. The erf function acts as a low q cut-off that brings to zero the Porod low contribution at a point depending on the R_g parameter. For globular nano-objects (neither flat disks nor thin cylinders) with smooth surface the exponent P is equal to 4 while for fractal objects $1<P<3$ (in this case the exponent P is the fractal dimensionality of the object).

The total intensity produced by a concentrated (not dilute) set of particles is no longer the sum of the intensity scattered by each particle. For the particular case of centro-symmetrical particles, the total intensity can be written as the product of the intensity $F(q)$ produced by a dilute system of particles (form factor) by the structure function, $S(q)$, that accounts for interference effects (Equation (6)):

$$I(q) = F(q)\cdot S(q) \tag{6}$$

Equation (6) applies, for example, to a set of identical spheres and can be used as a more or less good approximation for not too anisometric nano-objects. Applying the Born-Green theory, Beaucage [49] proposed a semi-empirical and simple structure function $S(q)$ given by Equation (7):

$$S(q) = \frac{1}{1 + k\theta} \tag{7}$$

where k and θ are the so-called packing factor and a form function, respectively. The packing factor k describes the degree of correlation that measures the number of nearest neighbor particles and it is equal to $8V/V_0$ where V is the average 'hard-core' volume and V_0 is the average available volume to each sphere. The form function θ depends on the average inter-particle distance d as follows (Equation (8)):

$$\theta = \frac{3\left[\sin(qd) - qd\cos(qd)\right]}{(qd)^3} \tag{8}$$

Furthermore, the total scattering intensity produced by a two-level structure can be described, under certain assumptions [49], as additive contributions from the individual levels. Nanometric domains (clusters or islands), each of them composed of a dense set of particles, embedded in a low-density matrix, give a contribution to the total intensity at very small q. This contribution to SAXS intensity from the second level, coarse, can also be described by Equation (2). The scattering intensity produced by domains with an average radius of gyration R_{g_2} composed of smaller particles with an average radius of gyration R_{g_1} is given by Equation (9) [49, 50]:

$$I(q) = \left[G_1 \exp\left(\frac{-q^2 R_{g_1}^2}{3} \right) + B_1 \left[\frac{\left(erf\left(\frac{qR_{g_1}}{2.449} \right) \right)^3}{q} \right]^{P_1} \right] \cdot S_1(q) + \left[G_2 \exp\left(\frac{-q^2 R_{g_2}^2}{3} \right) + B_2 \exp\left(\frac{-q^2 R_{g_1}^2}{3} \right) \left[\frac{\left(erf\left(\frac{qR_{g_2}}{2.449} \right) \right)^3}{q} \right]^{P_2} \right] \cdot S_2(q) \tag{9}$$

When the secondary domains are non spatially correlated, we have $S_2(q) = 1$. In some cases, due to the experimental limitation imposed by the minimum accessible q-value, only the asymptotic Porod range of the secondary coarse level can be practically observed.

3.2.2. SAXS results

Figure 3 shows the SAXS patterns in log-log plot for the SSO-PMMA/epoxy composites as a function of the SSO-PMMA composition, as described in Table 1. All spectra exhibit a large broad band with a maximum located around 0.44 $Å^{-1}$ attributed to local fluctuations density of epoxy resin [51]. Moreover, it is possible to identify two other scattering regions: a decreasing linear regime at low q-range ($q \leq 0.08$ $Å^{-1}$) whose lower and upper limits change with SSO-PMMA composition and an interference peak located at higher q-range (q around 0.09 $Å^{-1}$). Since the density of the siloxane phase is much higher than those of both PMMA and epoxy phases, it is possible to assume that the X-ray scattering in these two q-ranges is related to the electronic density contrast between the siloxane and the polymeric phases. The presence of such two regimes has already been observed in other siloxane-polymer hybrid and composites [52] and is characteristic of the existence of a hierarchical structure consisting of two structural levels: the siloxane primary nanoparticles (first level) forming secondary aggregates distributed inside the polymer matrix (second level). Therefore, a first analysis of our SAXS results lead us to the conclusion that the primary siloxane particles concentrate in

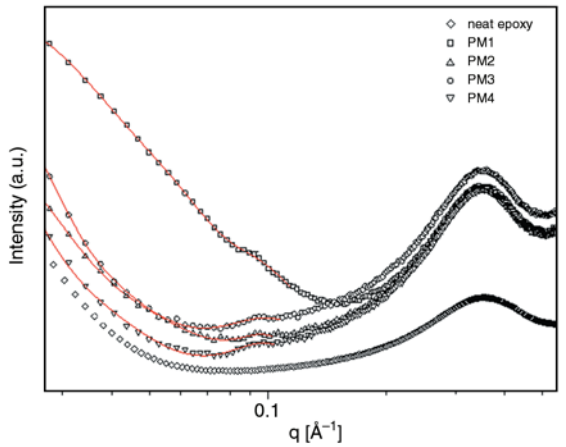

Figure 3. SAXS patterns in log-log plot for the SSO-PMMA/epoxy composites as a function of the SSO-PMMA composition

relatively large nanometric domains embedded in a particles-depleted polymeric matrix.

Furthermore, for all SSO-PMMA modified epoxy systems prepared in this work, the experimental SAXS intensity curves $I(q)$ (points in Figure 3) are well fitted by the theoretical function given by Equation (8) that considers two structural levels with $S_1(q)\neq1$ and $S_2(q)\neq1$ (red line in Figure 3). This well fitting confirms the validity of the model of large secondary nanometric domains composed of spatially correlated quite spherical siloxane primary nanoparticles embedded in a polymeric matrix.

As discussed below, the Beaucage equation also allows obtaining quantitative information about the structural parameters of epoxy-based nanocomposites. Table 3 shows the structure parameters G_1, R_{g_1}, k_1, d_1, G_2, R_{g_2} and P_2 determined from the best fitting procedure. The parameter P_1 has been fixed to the value 4, assuming a smooth surface for siloxane nanoparticles. For the nanocomposite containing the PM1 hybrid (with 44% of siloxane in the hybrid (Figure 3), the siloxane particle radius was determined as around 2 Å, revealing the interpenetration of the SSO-PMMA with epoxy matrix at a nanometric scale. Since for this sample a tendency to Guinier plateau is observed in log-log plot, the determination of the average gyration radius R_{g_2} of the secondary domains dispersed in the polymer matrix is possible (R_{g_2} = 90 Å, Table 3). Furthermore the value of P_2 is 1.3, revealing that the structure of the secondary domains is a very poorly ramified (quite linear) fractal structure [53].

By increasing MMA content in the SSO-PMMA a clear decrease of the packing factor k_1 simultaneously with a shift towards lower q-range of the linear regime associated to the secondary large domains with a disappearance of the Guinier plateau are observed for the epoxy-based composites (Table 3 and Figure 3). The decrease of the packing factor by increasing MMA content in the hybrid copolymer is consistent with the decrease in intensity of the interference peak located around 0.09 $Å^{-1}$ as the PMMA amount in the hybrid material increases (Figure 3), both trends revealing the progressive loss of the spatial correlation between the siloxane nanoparticles located inside the secondary hybrid aggregates. This better dispersion of siloxane particles in epoxy matrix by increasing PMMA content in SSO-PMMA should be related to the lower condensation degree of the hybrid compounds containing higher MMA fraction (Table 2). As a matter of fact, the reaction between the hydroxyl groups present in the partially condensed SSO-PMMA and the anhydride used as the hardener during epoxy curing should promote chemical affinity between SSO-PMMA and epoxy, favoring siloxane nanoparticles dispersion. Another contribution should be the probable increase in PMMA chains length bonded to siloxane particles by adding more MMA in the hybrid, inhibiting siloxane particles aggregation. Note that the latter interpretation is consistent with the observed growth of the secondary aggregates size, attested by the shift of the Guinier plateau towards a q-range lower than the limit accessible using the setup of our experiment, as the PMMA fraction in the hybrid material increases (Figure 3). Unfortunately, the very short extension of the linear regime at low q values and the absence of a trend toward a

Table 3. Structure parameters of the epoxy network modified with SSO-PMMA hybrid materials (6%), obtained by SAXS

SSO-PMMA composition [%]		G_2	R_{g_2}	G_1	R_{g_1}	k_1	d_1
Siloxane	PMMA	(arb.units)	[Å]	(arb.units)	[Å]		[Å]
44	56	$3.7\cdot10^{-6}$	90	$1.5\cdot10^{-7}$	1.9	4.4	54
20	80	–	–	$1.6\cdot10^{-7}$	1.2	2.6	53
14	86	–	–	$2.8\cdot10^{-7}$	1.8	1.3	53
8	92	–	–	$2.0\cdot10^{-7}$	1.4	0.8	54

constant value for decreasing q for these samples impede the determination of the average gyration radius R_{g2} of the secondary aggregates and also the P_2 and G_2 values. As a matter of fact in absence of Guinier plateau the values of these parameters obtained from the fit of Equation (9) have no physical meaning.

3.3. Scanning electron microscopy

The scanning electron micrographs of epoxy modified with PMMA and the corresponding SSO-PMMA hybrid materials are illustrated in Figure 4. Epoxy network modified with PMMA presents some dispersed domain phase, whose size stayed in the range of 1–1.5 μm (Figure 4c). The size domains are micrometric because of the quite good compatibility between epoxy matrix and PMMA. Epoxy network modified with PM1 hybrid material presents a homogeneous morphology without discernible phase separation, indicating that all the SSO-PMMA hybrid material is dispersed inside the epoxy matrix in nanometric dimension. This behavior is in agreement with the SAXS results since the average size of the aggregates in this system was calculated to be around 9 nm. These results evidence a better interaction between the hybrid organic-inorganic PM1 compound and the epoxy network than between PMMA and epoxy, due to low PMMA content in PM1.

As the amount of PMMA in the SSO-PMMA hybrid material increases, the phase separation at a micrometric scale is observed (Figure 4b). This phenomenon of microphase segregation of PMMA in an epoxy matrix is well-known and occurs during the cure of the epoxy resin, due to the fact that hydroxyl and epoxy groups, which promote chemical affinity between non-cured epoxy resin and PMMA, are changed into other groups during this process [54]. The microdomain sizes are even a little bit larger than that observed for epoxy/PMMA network, suggesting the presence of epoxy resin inside the domains, increasing their size. This result is consistent with the low condensation degree of PM3 determined from ^{29}Si NMR, which should induce a reaction between the hydroxyl groups present in the partially condensed SSO-PMMA and the anhydride used as the hardener. This phenomenon promotes good chemical affinity between the hybrid and epoxy, favoring epoxy penetration in the microdomains. Note that the increase of PMMA content in SSO-PMMA leads to opposite effects on microstructure (investigated by SEM) and nanostructure (investigated by SAXS) of the epoxy-based composites: while larger PMMA amounts promotes microphase separation of PMMA-rich domains, they avoid nanophase segregation of siloxane-rich regions.

3.4. Dynamic mechanical properties

The effect of the addition of SSO-PMMA hybrid material on the dynamic mechanical properties of modified epoxy networks was evaluated in terms of storage modulus and loss factor (tanδ). Figure 5 illustrates the dependence of these dynamic mechanical properties as a function of temperature. The glass transition temperature (T_g) was taken as the temperature at the maximum of the tanδ peak. The curves of the neat epoxy resin and that modified with PMMA were also included for comparison.

The epoxy resin modified with pure PMMA displayed lower T_g compared with the neat epoxy network. Since epoxy chains extremities contain acrylate groups, the number of epoxy groups available to react with anhydride is lower than in neat epoxy, leading to a less efficient curing process and conse-

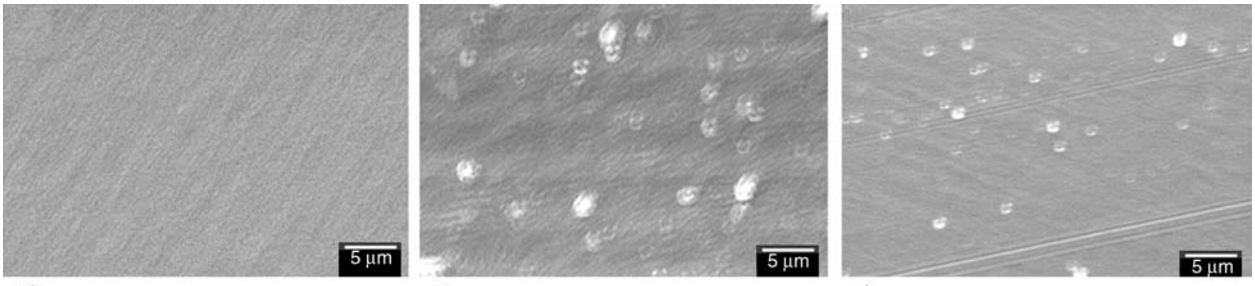

Figure 4. SEM micrographs of epoxy modified with SSO-PMMA hybrid materials containing 56% of PMMA (PM1) (a) 86% of PMMA (PM3) (b) and modified with pure PMMA (c)

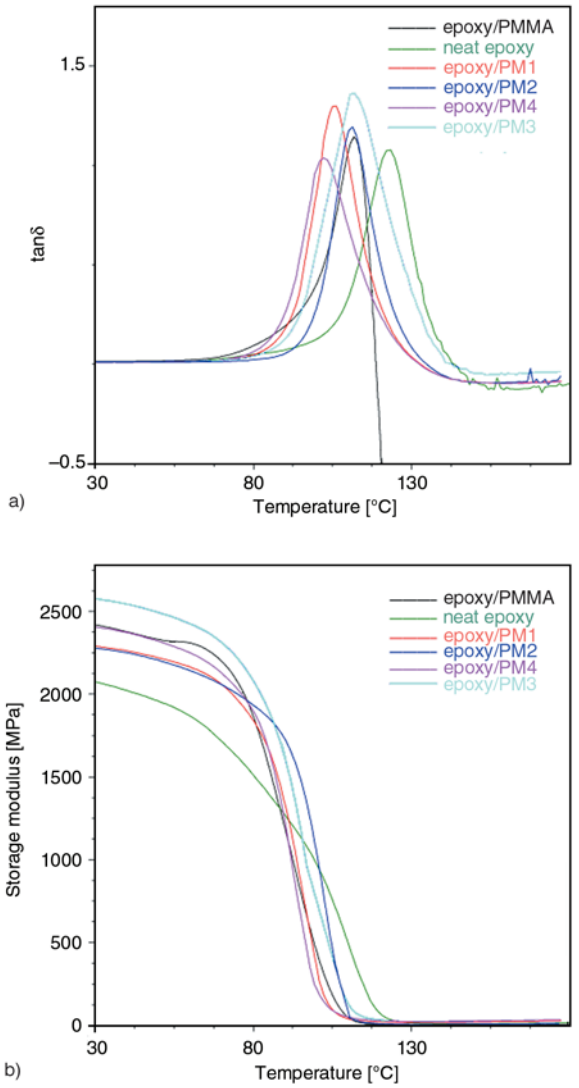

Figure 5. Dynamic mechanical properties of epoxy network modified with PMMA and SSO-PMMA hybrid materials

quently diminishing T_g. However, a plasticizing effect of PMMA because of its lower glass transition temperature than epoxy and its good compatibility with the epoxy matrix [54–56] should not be discarded.

All nanocomposites also presented lower T_g values than the neat epoxy resin. Besides the plasticizing effect of PMMA already described, this behavior should also be due to the possible chemical reaction between silanol groups of the SSO-PMMA and anhydride. The lower amount of anhydride available for the curing process of epoxy resin induce a decrease of T_g.

A surprising result that can be observed is a significant decrease of T_g for the nanocomposite containing PM1, which has the lowest PMMA content in the SSO-PMMA hybrid material. This phenomenon may be attributed to an increase of the free volume caused by the presence of the hybrid siloxane-rich aggregates, evidenced by SAXS experiments. As a matter of fact, it has been shown that the presence of inorganic nanodomains or nanoparticles in epoxy matrix should lead to the increase of the free volume of epoxy [57].

The presence of the SSO-PMMA resulted in a significant increase of the storage modulus taken at temperature lower than the glass transition temperature, indicating a reinforcing action of the hybrid material on the epoxy matrix. The increase of PMMA content in the hybrid increased the modulus and the highest value was achieved by using the PM3 hybrid material. The epoxy network containing the PM4 hybrid material (with higher PMMA content) presented a storage modulus comparable with that modified with pure PMMA. These results are directly correlated with the hierarchical nature of the nanostructure of the composites detected by SAXS. As a matter of fact SAXS results have revealed an increase in size of the secondary hybrid aggregates (formed by the segregation of primary siloxane particles in the epoxy matrix) by increasing the fraction of PMMA in the hybrid compound. Consequently, at least up to a PMMA fraction corresponding to PM3, the presence of siloxane-rich secondary hybrid domains acts as reinforcing heterogeneities dispersed in epoxy resin and consequently the increase in size of these secondary aggregates leads to higher values of storage modulus. The modulus of the composite containing PM4 is lower than the one containing PM3 due to the quite absence of particles aggregation for this sample, evidenced by SAXS.

4. Conclusions

This work describes for the first time the modification of epoxy network by SSO-PMMA hybrid materials prepared by simultaneous hydrolysis/condensation of the silane precursor and polymerization of MMA. The addition of low amount of the SSO-PMMA hybrid material containing low amount of PMMA resulted in nanocomposites with no discernible phase separation. From SAXS experiments it was possible to suggest the presence of hierarchical structure characterized by organically modified siloxane nanoparticles forming larger hybrid nanoaggregates uniformly dispersed

inside the epoxy matrix. The spatial correlation between the siloxane nanoparticles inside the aggregates were lost as the amount of PMMA in the hybrid material increased, indicating an increased ability of epoxy chains in diffusing through the hybrid aggregates as a consequence of the good affinity between the hybrid material and the epoxy matrix promoted by the reaction between the hydroxyl groups of the non condensed SSO-PMMA and the anhydride which was employed as the hardener. The structural model proposed concerning the nanostructural features of epoxy/SSO-PMMA composites obtained by SAXS is consistent with the thermomechanical properties of the materials investigated by DMA. The good interaction between the components resulted in a significant decrease of the glass transition temperature but an increase of the storage modulus of the epoxy network. These results are important since they show that it is possible to achieve epoxy networks with increased modulus by adding a small amount of hybrid material.

Further investigations are planned to establish the relationships between the method used in the SSO-PMMA synthesis and the nanostructure and properties of the resulting epoxy-based network.

Acknowledgements

This work has been sponsored by Conselho Nacional de Desenvolvimento Científico e Tecnológico (CNPq) and Fundação de Amparo à Pesquisa do Estado do Rio de Janeiro (FAPERJ). The authors would like to thank the Brazilian Synchrotron Light Laboratory (LNLS) for the help in SAXS measurements.

References

[1] Nigam V., Setua D. K., Mathur G. N.: Failure analysis of rubber toughened epoxy resin. Journal of Applied Polymer Science, **87**, 861–868 (2003). DOI: 10.1002/app.11519

[2] Thomas R., Abraham J., Thomas S. P., Thomas S.: Influence of carboxyl-terminated (butadiene-co-acrylonitrile) loading on the mechanical and thermal properties of cured epoxy blends. Journal of Polymer Science Part B: Polymer Physics, **42**, 2531–2544 (2004). DOI: 10.1002/polb.20115

[3] Kar S., Banthia A. K.: Use of acrylate-based liquid rubbers as toughening agents and adhesive property modifiers of epoxy resin. Journal of Applied Polymer Science, **92**, 3814–3821 (2004). DOI: 10.1002/app.20397

[4] Barcia F. L., Abrahao M. A., Soares B. G: Modification of epoxy resin by isocyanate-terminated polybutadiene. Journal of Applied Polymer Science, **83**, 838–849 (2002). DOI: 10.1002/app.10079

[5] Barcia F. L., Amaral T. P., Soares B. G.: Synthesis and properties of epoxy resin modified with epoxy-terminated liquid polybutadiene. Polymer, **44**, 5811–5819 (2003). DOI: 10.1016/S0032-3861(03)00537-8

[6] Kumar K. D., Kothandaraman B.: Modification of (DGEBA) epoxy resin with maleated depolymerized natural rubber. Express Polymer Letters, **2**, 302–311 (2008). DOI: 10.3144/expresspolymlett.2008.36

[7] Li G. Z., Wang L., Toghiani H., Daulton T. L., Koyama K., Pittman C. U.: Viscoelastic and mechanical properties of epoxy/multifunctional polyhedral oligomeric silsesquioxane nanocomposites and epoxy/ladderlike polyphenylsilsesquioxane blends. Macromolecules, **34**, 8686–8693 (2001). DOI: 10.1021/ma011117q

[8] Zhou Y. X., Wu P. X., Cheng Z-Y., Ingram J., Jeelani S.: Improvement in electrical, thermal and mechanical properties of epoxy by filling carbon nanotube. Express Polymer Letters, **2**, 40–48 (2008). DOI: 10.3144/expresspolymlett.2008.6

[9] Crosby A. J., Lee J-Y.: Polymer nanocomposites: The 'nano' effect on mechanical properties. Polymer Reviews, **47**, 217–229 (2007). DOI: 10.1080/15583720701271278

[10] Pielichowski K., Njuguna J., Janowski B., Pielichowski J.: Polyhedral oligomeric silsesquioxanes (POSS)-containing nanohybrid polymers. Advances in Polymer Science, **201**, 225–296 (2006). DOI: 10.1007/12_077

[11] Zhang J., Xu R., Yu D.: A novel poly-benzoxazinyl functionalized polyhedral oligomeric silsesquioxane and its nanocomposite with polybenzoxazine. European Polymer Journal, **43**, 743–752 (2007). DOI: 10.1016/j.eurpolymj.2006.11.012

[12] Ikeda M., Saito H.: Improvement of polymer performance by cubic-oligosilsesquioxane. Reactive and Functional Polymers, **67**, 1148–1156 (2007). DOI: 10.1016/j.reactfunctpolym.2007.08.008

[13] Baney R. H., Itoh M., Sakakibara A., Suzuki T.: Silsexquioxanes. Chemical Reviews, **95**, 1409–1430 (1995). DOI: 10.1021/cr00037a012

[14] Feher F. J., Budzichowski T. A.: New polyhedral oligosilsesquioxanes via the catalytic hydrogenation of aryl-containing silsesquioxanes. Journal of Organometallic Chemistry, **373**, 153–163 (1989). DOI: 10.1016/0022-328X(89)85041-7

[15] Agaskar A. P.: Facile, high-yield synthesis of functionalized spherosilicates: Precursors of novel organolithic macromolecular materials. Inorganic Chemistry, **29**, 1603 (1990). DOI: 10.1021/ic00334a005

[16] Sellinger A., Laine R. M.: Silsesquioxanes as synthetic platforms. 3. Photocurable, liquid epoxides as inorganic/organic hybrid precursors. Chemistry of Materials, **8**, 1592–1593 (1996). DOI: 10.1021/cm9601493

[17] Mascia L., Prezzi L., Lavorgna M.: Peculiarities in the solvent absorption characteristics of epoxy-siloxane hybrids. Polymer Engineering and Science, **45**, 1039–1048 (2005). DOI: 10.1002/pen.20372

[18] Liang K., Li G., Toghiani H., Koo J. H., Pittman C. U.: Cyanate ester/polyhedral oligomeric silsesquioxane (poss) nanocomposites: Synthesis and characterization. Chemistry of Materials, **18**, 301–312 (2006). DOI: 10.1021/cm051582s

[19] Teo J. K. H., Teo K. C., Pan B., Xiao Y., Lu X.: Epoxy/polyhedral oligomeric silsesquioxane (POSS) hybrid networks cured with an anhydride: Cure kinetics and thermal properties. Polymer, **48**, 5671–5680 (2007). DOI: 10.1016/j.polymer.2007.07.059

[20] Ochi M., Matsumura T.: Thermomechanical properties and phase structure of epoxy/silica nano-hybrid materials constructed from a linear silicone oligomer. Journal of Polymer Science Part B: Polymer Physics **43**, 1631–1639 (2005). DOI: 10.1002/polb.20465

[21] Çopuroglu M., O'Brien S., Crean G. M.: Effect of preparation conditions on the thermal stability of an epoxy-functional inorganic-organic hybrid material system with phenyl side group. Polymer Degradation and Stability, **91**, 3185–3190 (2006). DOI: 10.1016/j.polymdegradstab.2006.07.017

[22] Lee A., Lichtenahn J. D.: Viscoelastic responses of polyhedral oligosilsesquioxane reinforced epoxy systems. Macromolecules, **31**, 4970–4974 (1998). DOI: 10.1021/ma9800764

[23] Jones I. K., Zhou Y. X., Jeelani S., Mabry J. M.: Effect of polyhedral-oligomeric-sil-sesquioxanes on thermal and mechanical behavior of SC-15 epoxy. Express Polymer Letters, **2**, 494–501 (2008). DOI: 10.3144/expresspolymlett.2008.59

[24] Choi J., Harcup J., Yee A. F., Zhu Q., Laine R. M.: Organic/inorganic hybrid composites from cubic silsesquioxanes. Journal of American Chemical Society, **123**, 11420–11430 (2001). DOI: 10.1021/ja010720l

[25] Matejka L., Strachota A., Plestil J., Whelan P., Steinhart M., Šlouf M.: Epoxy networks reinforced with polyhedral oligomeric silsesquioxanes (POSS). Structure and morphology. Macromolecules, **37**, 9449–9456 (2004). DOI: 10.1021/ma0484577

[26] Liu Y., Zheng S., Nie K.: Epoxy nanocomposites with octa(propylglycidyl ether) polyhedral oligomeric silsesquioxane. Polymer, **46**, 12016–12025 (2005). DOI: 10.1016/j.polymer.2005.09.056

[27] Dias Filho N. L., Cardoso C. X., Aquino H. A.: Relationships between the curing conditions and some mechanical properties of hybrid thermosetting materials. Journal of Brazilian Chemical Society, **17**, 935–943 (2006). DOI: 10.1590/S0103-50532006000500018

[28] Zhang Z., Liang G., Wang X.: The effect of POSS on the thermal properties of epoxy. Polymer Bulletin, **58**, 1013–1020 (2007). DOI: 10.1007/s00289-007-0732-6

[29] Chang K-C., Lin C-Y., Lin H-F., Chiou S-C., Huang W-C., Yeh J-M., Yang J-C.: Thermally and mechanically enhanced epoxy resin-silica hybrid materials containing primary amine-modified silica nanoparticles. Journal of Applied Polymer Science, **108**, 1629–1635 (2008). DOI: 10.1002/app.27559

[30] Lee T-M., Ma C-C. M., Hsu C-W., Wu H-L.: Effect of molecular structures and mobility on the thermal and dynamical mechanical properties of thermally cured epoxy-bridged polyorganosiloxanes. Polymer, **46**, 8286–8296 (2005). DOI: 10.1016/j.polymer.2005.06.069

[31] Zhang Z., Gu A., Liang G., Ren P., Xie J., Wang X.: Thermo-oxygen degradation mechanisms of POSS/epoxy nanocomposites. Polymer Degradation and Stability, **92**, 1986–1993 (2007). DOI: 10.1016/j.polymdegradstab.2007.08.004

[32] Choi J., Kim S. G., Laine R. M.: Organic/inorganic hybrid epoxy nanocomposites from aminophenylsilsesquioxanes. Macromolecules, **37**, 99–109 (2004). DOI: 10.1021/ma030309d

[33] Fu J., Shi L., Chen Y., Yuan S., Wu J., Liang X., Zhong Q.: Epoxy nanocomposites containing mercaptopropyl polyhedral oligomeric silsesquioxane: Morphology, thermal properties and toughening mechanism. Journal of Applied Polymer Science, **109**, 340–349 (2008). DOI: 10.1002/app.27917

[34] Liu Y-L., Chang G-P., Wu C-S., Chiu Y-S.: Preparation and properties of high performance epoxy-silsesquioxane hybrid resins prepared using a maleimide-alkoxysilane compound as a modifier. Journal of Polymer Science Part A: Polymer Chemistry, **43**, 5787–5798 (2005). DOI: 10.1002/pola.21057

[35] Ni Y., Zheng S.: Epoxy resin containing octamaleimidophenyl polyhedral oligomeric sil-sesquioxane. Macromolecular Chemistry and Physics, **206**, 2075–2083 (2005).
DOI: 10.1002/macp.200500267

[36] Chang R-C., Chiang C-L., Chiu Y-C.: Synthesis, characterization, and properties of novel organic/inorganic epoxy hybrids containing nitrogen/silicon via the sol-gel method. Journal of Applied Polymer Science, **106**, 3290–3297 (2007).
DOI: 10.1002/app.26994

[37] Saravanamuttu K., Du X. M., Najafi S. I., Andrews M. P.: Photoinduced structural relaxation and densification in sol-gel-derived nanocomposite thin films: Implications for integrated optics device fabrication. Canadian Journal of Chemistry, Revue Canadienne de Chimie, **76**, 1717–1729 (1998).

[38] Tadanaga K., Ellis B., Seddon A.: Near- and mid-infrared spectroscopy of sol-gel derived ormosil films for photonics from tetramethoxysilane and trimethoxysilylpropylmethacrylate. Journal of Sol-Gel Science and Technology, **19**, 687–690 (2000).
DOI: 10.1023/A:1008714806606

[39] Sarmento V. H. V., Frigério M. R., Dahmouche K., Pulcinelli S. H., Santilli C. V.: Evolution of rheological properties and local structure during gelation of siloxane-polymethylmethacrylate hybrid materials. Journal of Sol-Gel Science and Technology, **37**, 179–184 (2006).
DOI: 10.1007/s10971-005-6625-y

[40] Amir N., Levina A., Silverstein M. S.: Nanocomposites through copolymerization of a polyhedral oligomeric silsesquioxane and methyl methacrylate. Journal of Polymer Science Part A: Polymer Chemistry, **45**, 4264–4275 (2007).
DOI: 10.1002/pola.22168

[41] Wei Y., Yang D., Bakthavatchalam R.: Thermal stability and hardness of new polyacrylate-SiO_2 hybrid sol-gel materials. Materials Letters, **13**, 261–266 (1992).
DOI: 10.1016/0167-577X(92)90228-C

[42] Sarmento V. H. V., Dahmouche K., Santilli C. V., Pulcinelli S. H., Craievich A. F.: Small-angle X-ray scattering and nuclear magnetic resonance study of siloxane-PMMA hybrids prepared by the sol-gel process. Journal of Applied Cristallography, **36**, 473–477 (2003).
DOI: 10.1107/S0021889803000384

[43] Cornu J. F: Synthèse et Etude de la Relation Microstructure-Propriétés de Matériaux Hybrides Organiques-Inorganiques à base TMSM et Application au Renforcement des Verres. PhD Thesis, Institut National des Sciences Appliquées (INSA), Villeurbanne, France (1993).

[44] Joseph R., Zhang Z., Ford W. T.: Structure and dynamics of a colloidal silica-poly(methacrylate) composite by ^{13}C and ^{29}Si MAS NMR spectroscopy. Macromolecules, **29**, 1305–1312 (1996).
DOI: 10.1021/ma951111z

[45] Brinker J. C., Scherer G. W.: Sol-gel science: The physics and chemistry of sol-gel processing. Academic Press, San Diego (1989).

[46] Sarmento V. H. V.: Estrutura e Propriedades de Materiais Híbridos de Siloxano-PMMA preparados pelo processo sol-gel. PhD Thesis, Universidade Estadual Paulista (UNESP), Araraquara, Brazil (2005).

[47] Guinier A., Fournet G.: Small angle scattering of X-rays. Wiley and Sons, New York (1955).

[48] Glatter O., Kratky O.: Small-angle scattering of X-ray. Academic Press, New York (1982).

[49] Beaucage G.: Approximations leading to a unified exponential power-law approach to small-angle scattering. Journal of Applied Crystallography, **28**, 717–728 (1995).
DOI: 10.1107/S0021889895005292

[50] Beaucage G., Ulibarri T. A., Black E. P., Schaefer D. W.: Multiple size scale structures in silica-siloxane composites studied by small-angle scattering. in 'Hybrid organic-inorganic composites' (eds.: Seddon A. B., Turner M. L.) ACS Symposium Series, Albuquerque, Vol 585, 97–111 (1995).

[51] Prado L. A. S. A., Cascione M., Wichmann M. H. G., Gojny F. H., Fiedler B., Schulte K., Goerigk G.: SAXS studies on nanocomposites based on epoxy resins reinforced with Aerosil(r) nanoparticles. Hasylab Annual Report, 945–946 (2005).

[52] Dahmouche K., Carlos L. D., Bermudez V. Z., Ferreira R. A. S., Santilli C. V., Craievich A. F.: Structural modelling of Eu3+-based siloxane-poly(oxyethylene) nanohybrids. Journal of Materials Chemistry, **11**, 3249–3257 (2001).
DOI: 10.1039/b104822h

[53] Schaefer D. W., Keefer K. D.: Fractal geometry of silica condensation polymers. Physical Review Letters, **53**, 1383–1386 (1984).
DOI: 10.1103/PhysRevLett.53.1383

[54] Gomez C. M., Bucknall C. B.: Blends of poly(methyl methacrylate) with epoxy resin and an aliphatic amine hardener. Polymer, **34**, 2111–2117 (1993).
DOI: 10.1016/0032-3861(93)90737-U

[55] Ritzenthaler S., Girard-Reydet E., Pascault J. P.: Influence of epoxy hardener on miscibility of blends of poly(methyl methacrylate) and epoxy networks. Polymer, **41**, 6375–3686 (2000).
DOI: 10.1016/S0032-3861(99)00817-4

[56] Remiro P. M., Marieta C., Riccardi C. C., Mondragon I.: Influence of curing conditions on the morrphologies of a PMMA-modified epoxy matrix. Polymer, **42**, 9909–9914 (2001).
DOI: 10.1016/S0032-3861(01)00564-X

[57] Ni Y., Zheng S., Nie K.: Morphology and thermal properties of inorganic-organic hybrids involving epoxy resin and polyhedral oligomeric silsesquioxanes. Polymer, **45**, 5557–5568 (2004).
DOI: 10.1016/j.polymer.2004.06.008

eXPRESS Polymer Letters Vol.3, No.6 (2009) 352–358
Available online at www.expresspolymlett.com
DOI: 10.3144/expresspolymlett.2009.44

Synthesis and characterization of novel organotin carboxylate maleimide monomers and copolymers

C. Gaina, V. Gaina*

'Petru Poni' Institute of Macromolecular Chemistry, 41 A Gr.Ghica Voda Alley, Iasi, RO-700487, Romania

Received 3 February 2009; accepted in revised form 28 March 2009

Abstract. Two novel tributyltin carboxylate maleimide monomers, tributyltin(maleimido)acetate and tributyltin(4-maleimido)benzoate, were synthesized by condensation reaction of maleimidoacetic acid or 4-maleimidobenzoic acid with bis(tributyltin) oxide. Copolymerization of these monomers with styrene was carried in dioxane at 70°C using asobisisobutyronitrile as free radical initiator. The structures of monomers and copolymers were confirmed by FT-IR (Fourier Transform Infrared), ^{1}H and ^{13}C NMR (nuclear magnetic resonance) spectroscopy and elemental analysis. The copolymers were characterized by solubility and thermal analysis.

Keywords: *polymer synthesis, molecular engineering, tributyltin polymeric carboxylate, tin coordination, maleimide copolymer*

1. Introduction

Organotin derivatives of a compound containing the bioactive alkyltin groups, attached to organic compound *via* O–Sn and N–Sn bonds, have considerable interest in several research fields. Apart from academic concern related to fundamental research, tin derivatives are widely used as components for antifouling paints [1–4], as catalysts in organic synthesis of polyesters, polyurethanes and crosslinking silicone [5–7], as well as anti-tumor drugs [8, 9] and ion carriers in electrochemical membrane building [10]. Generally, tin derivatives suffer of some toxicity and applications involving tin leaching should be improved, or even avoided. By minimize this drawback, successful results may be obtained by anchoring organotin functionality to a macromolecular chain [11], which prevents the leaching of the toxic residue and facilitates the recovery of the organo-metallic material after its use. Acrylic copolymers with pendant organotin carboxylate moieties have found wide-spread applications as antifouling agents [12–14] and fungicides [15]. Two types of organotin maleimide derivatives have been prepared and their biological activity was investigated [16, 17].

The present investigation deals with synthesis and characterization of new maleimide monomers containing tributyltin carboxylate units linked to the aromatic ring or aliphatic rest, and their copolymers with styrene.

2. Expermental

2.1. Measurements

The Fourier transform infrared (FTIR) spectra were recorded on a Bruker Vertex 70 Instruments equipped with a Golden Gate single reflection ATR (attenuated total reflection) accessory, spectrum range 600–4000 cm^{-1}.

*Corresponding author, e-mail: gcost@icmpp.ro

The proton and carbon nuclear magnetic resonance (^{1}H-NMR and ^{13}C-NMR) spectra were recorded on a Bruker NMR spectrometer, Avance DRX 400 MHz, using DMSO-d_6 (dimethyl sulfoxide) and $CDCl_3$ as solvents and tetramethylsilane as an internal standard.
Melting and softening points were determined with a Gallenkamp hot-block point apparatus.
Differential scanning calorimetry (DSC) measurements were done using a Mettler TA Instrument DSC 12E with a heating rate of 10°C/min, in nitrogen.
Thermogravimetric analysis (TGA) was carried out in air with an F. Paulik Derivatograph at a heating rate of 10°C/min.
Gel permeation chromatographic (GPC) analyses were carried out on a PL-EMD 950 Evaporative light Detect instrument using N,N-dimethylformamide (DMF) as the eluant and standard polystyrene sample for calibration.

2.2. Reagents and materials

Chemicals were supplied by Fluka and Aldrich and used as received. Solvents were purified using standard purification techniques [18]. Maleimidobenzoic acid was prepared according to the method described in the literature [19]. *N*-maleimidoacetic acid was prepared according to Rich method [20], *mp* = 112–113°C.

2.2.1. General procedure for the preparation of tributyltin caboxylate maleimide monomers 2(a-b)

*Tributyltin (2,5-dioxo-2,5-dihydro- 1H-pyrrol-1-yl)acetate (**2a**)*

In a 250 ml flask equipped with a Dean Stark apparatus, maleimidoacetic acid (2.5 g, 16.10 mmol), benzene (120 ml) and bis(tributyltin) oxide (8.20 ml, 16.10 mmol) were added. The reaction mixture was heated until no more water evolution was observed and benzene was further distilled under reduced pressure. The monomer **2a** gives stable white crystals by crystallization from dioxane, yield 84%, *mp* = 99–100°C.
Elemental analysis calcd. for $C_{18}H_{31}NO_4Sn$ (444.10): C, 48.68; H, 7.04; N, 3.15; Sn, 26.72%. Found: C, 48.78; H, 7.11; N, 3.23; Sn, 26.90%.
FT-IR spectrum (KBr, cm^{-1}): 3100, 2980, 2920, 2860, 1720, 1605, 1580, 1425, 1390, 1315, 1150, 910, 840, 695, 675, 640.
^{1}H-NMR spectrum ($CDCl_3$, TMS), δ(ppm): 6.78 (s, 2H, maleimide protons), 4.21 (s, 2H, CH_2 of acetic rest), 1.70 (t, 6H, Sn–C<u>H</u>$_2$–CH_2–CH_2–CH_3), 1.45 (m, 12H, Sn–CH_2–C<u>H</u>$_2$–C<u>H</u>$_2$–CH_3) and 0.95 (t, 9H, Sn–CH_2–CH_2–CH_2–C<u>H</u>$_3$).
^{13}C-NMR spectrum ($CDCl_3$, TMS), δ(ppm):
13.52 (Sn–CH_2–CH_2–CH_2–<u>C</u>H_3),
16.60 (Sn–CH_2–CH_2–<u>C</u>H_2–CH_3),
27 (Sn–CH_2–<u>C</u>H_2–CH_2–CH_3),
27.58 (Sn–<u>C</u>H_2–CH_2–CH_2–CH_3),
39.21 (CH_2 of imide rest),
134.28 (CH of maleimide),
170.04 (C=O of maleimide ring),
171.45 (C=O of ester group).

*Tributyltin 4-(2,5-dioxo-2,5-dihydro-1H-pyrrol-1-yl)benzoate (**2b**)*

The same synthesis system as previously described was used and charged with 4-maleimidobenzoic acid (3.5 g, 16.10 mmol), acetone (50 ml), toluene (80 ml) and bis(tributyltin) oxide (8.20 ml, 16.10 mmol). The reaction mixture was heated at 56°C for 2 hours and then at reflux until no more water evolution was observed and toluene was further distilled under reduced pressure. The monomer **2b** was separated as white crystals by recrystallization from dioxane, *mp* = 119–123°C, yield 88%.
Elemental analysis calcd. for $C_{23}H_{33}NO_4Sn$ (506.17): C, 54.57; H, 6.57; N, 2.77; Sn, 23.45%. Found: C, 54.61; H, 6.81; N, 2.63; Sn, 23.36%.
FT-IR spectrum (KBr, cm^{-1}): 3110, 2980, 2960, 2860, 1715, 1655, 1605, 1510, 1396, 1340, 1210, 1150, 840, 695, 598, 440.
^{1}H-NMR spectrum (DMSO-d_6, TMS), δ(ppm): 8.02 (d, 2H, aromatic protons), 7.45 (d, 2H, aromatic protons), 7.20 (s, 2H, maleimide protons), 1.61 (t, 6H, Sn–C<u>H</u>$_2$–CH_2–CH_2–CH_3), 1.30 (m, 12H, Sn–CH_2–C<u>H</u>$_2$–C<u>H</u>$_2$–CH_3) and 0.85 (t, 9H, Sn–CH_2–CH_2–CH_2–C<u>H</u>$_3$).
^{13}C-NMR spectrum (DMSO-d_6, TMS), δ(ppm):
13.64 (Sn–CH_2–CH_2–CH_2–<u>C</u>H_3),
18.59 (Sn–CH_2–CH_2–<u>C</u>H_2–CH_3),
26.43 (Sn–CH_2–<u>C</u>H_2–CH_2–CH_3),
27.69 (Sn–<u>C</u>H_2–CH_2–CH_2–CH_3),
126.08 (2C, aromatic carbons),
127, 129, 130.40 (aromatic carbons),

134.82 (CH of maleimide),
169.65 (3C, C=O of maleimide and ester groups).

2.2.2. Copolymerization procedure

Copolymerization of monomers **2(a–b)** with styrene was carried out in dry dioxane (10 ml) in the presence of 2,2′-azobis(2-methylpropionitrile) (AIBN) as radical initiator (2% by weight with respect to the monomer mixtures). The total amount of monomers (**2(a–b)** and styrene) was 1 g, quantities calculated in order to have molar compositions in the feed of 70, 50, 30 and 20% monomer **2b** and 80, 60, 50 and 30% monomer **2a**.

All solutions were prepared under inert atmosphere into a polymerization vial, and then were degassed by the freeze-thaw technique. The inlet of the ampoule was sealed with gas-oxygen mixture under nitrogen atmosphere at low pressure and then transferred to a thermostated oil bath at 70°C for 24 hours. The copolymer was obtained by precipitation into a large amount of methanol. The precipitated polymer was purified twice by reprecipitation into chloroform/n-pentane mixture for copolymers **3(a–d)** and into chloroform/methanol mixture for copolymers **4(a–d)**.

3. Results and discussion

The tributyltin carboxylate monomers **2(a–b)** were synthesized by the condensation reaction of *N*-maleimidoacetic acid (**1a**) or 4-maleimidobenzoic acid (**1b**) with bis(tributyltin) oxide in benzene or toluene at reflux (Figure 1).

Structures of these monomers were confirmed by FT-IR and ^{1}H and ^{13}C NMR spectroscopy and elemental analysis. FT-IR spectra of monomers showed absorption bands characteristic to: imide ring at 3100 cm^{-1} (=CH stretching), 1725 cm^{-1} (asymmetric C=O stretching), 1385 and 1150 cm^{-1} (maleimide C–N–C stretching symmetric and asymmetric), 839 cm^{-1} (maleimide symmetric C–H out-of-plane bending) and 697 cm^{-1} (deformation of maleimide ring in plane), tributyltin carboxylate groups at 2980–2880 cm^{-1} (CH stretching of aliphatic butyl groups) and 1697 cm^{-1} (asymmetric stretching COO of carboxylate group). In addition, the spectrum of monomer **2b** shows absorption bands for *p*-substituted aromatic ring.

The ^{1}H-NMR spectra of monomers **2(a–b)** showed the signals for all types of protons. The spectrum of monomer **2a** presents a singlet at 6.78 ppm attributed to maleimide protons, a singlet at 4.21 ppm for >N–CH$_2$–COO– protons and three multiple signals at 1.70, 1.45 and 0.95 ppm corresponding to butyl group protons. In addition, the spectrum of monomer **2b** shows aromatic protons as two doublets at 7.45 and 8.02 ppm. The butyl group protons of monomer **2b** appear upfield shifted due to the solvent (DMSO). The ^{13}C-NMR spectra of monomers **2(a–b)** (Figures 2 and 3) show signals for aliphatic carbon atoms at 13.52, 16.60, 27 and 27.58 ppm for butyl group carbons and at 39.21 ppm for –CH$_2$– from acetyl group. HC= carbons of maleimide appear at 134.30 or 134.82 ppm respectively, C=O carbons of maleimide appear at 170 ppm and COO

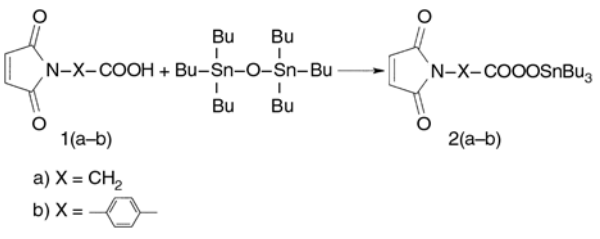

Figure 1. The synthesis of monomers **2(a–b)**

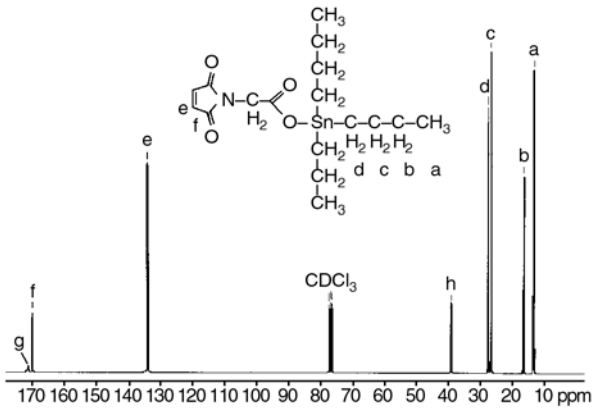

Figure 2. The ^{13}C-NMR spectra of monomer **2a**

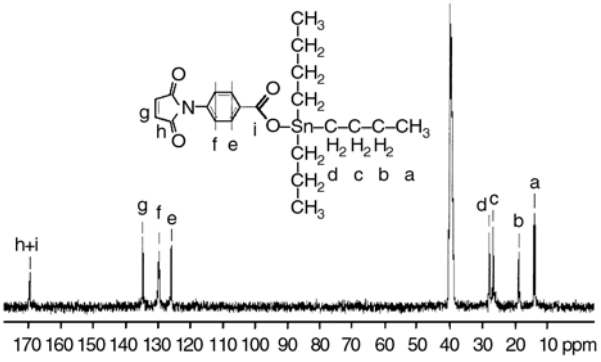

Figure 3. The ^{13}C-NMR spectra of monomer **2b**

carbon at 171.447 ppm. The aromatic carbons from monomer **2b** appear in the range 126.077–129.849 ppm.

The copolymerization of monomers **2(a–b)** was carried out in the presence of significant amount of thermal initiator (2% AIBN). The general structure of the copolymers is illustrated in Figure 4. The experimental copolymerization conditions results and copolymer compositions determined by elemental analysis data are shown in Table 1. The copolymers were insoluble in water, methanol and soluble in chloroform, acetone and dimethylsulfoxide (DMSO). The yield was lower than 83% for all the copolymerization reactions and there was not an important effect of the monomer feed composition on the yield. The average molecular weight ranged between 34 800 and 129 000 g/mol and the polydispersity varied in the range of 1.36–2.35.

The chemical structures of the copolymers were confirmed by FT-IR and ^{1}H-NMR spectroscopy and elemental analysis. The FT-IR spectra of copolymers as shown in Figure 5, revealed the absorption bands at 1778, 1720 cm^{-1} (corresponding to symmetrical and asymmetrical C=O stretching of the imide ring), 1377, 1172 cm^{-1} (maleimide C–N–C stretching symmetric and asymmetric), 695 cm^{-1} (imide ring), 3060, 1600, 820 cm-1(aromatic rings), 2958-2853 cm^{-1} (vibration of aliphatic rest) and new absorption bands at 1570, 1455, 1418 cm^{-1} for copolymers **3(a–d)** and at 1647, 1463, 1474, 1407 cm^{-1} for copolymers **4(a–d)**

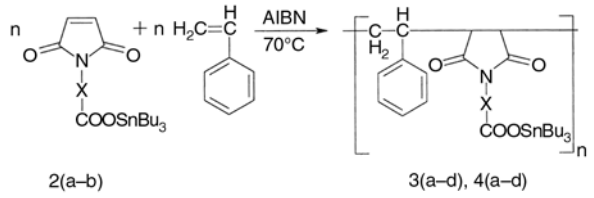

Figure 4. The synthesis of copolymers **3(a–d)** and **4(a-d)**

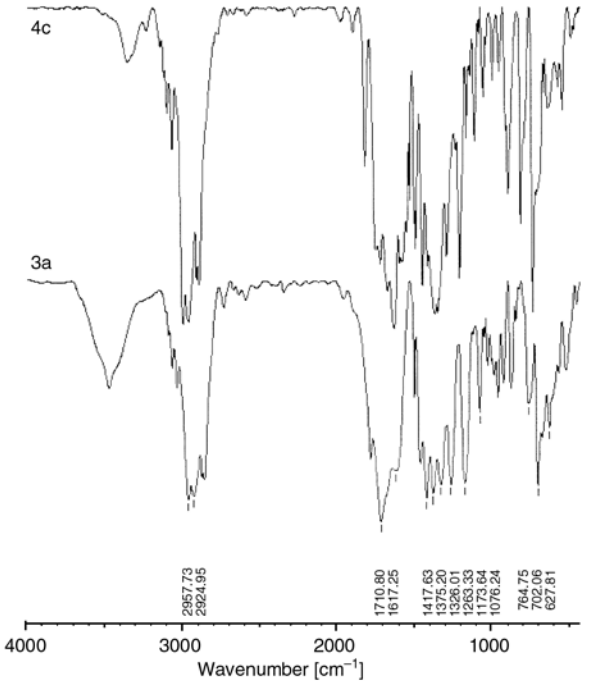

Figure 5. The FT-IR spectra of copolymers **3a** and **4c**

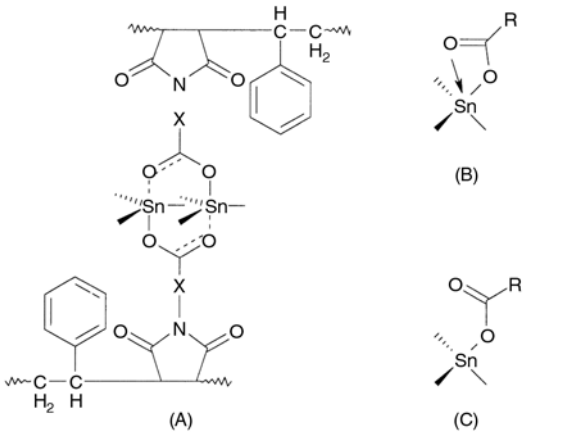

Figure 6. The possible structures for non-polymeric tributyltin carboxylates in the solid state

Table 1. Copolymerization of monomers **2(a–b)** (M_1) with styrene (M_2) in dioxane at 70°C, in the presence of AIBN[a]

Copolymer	Monomer feed		Conversion [wt%]	Copolymer composition		$\overline{M}_n$ (×10^{-4})[c] [g/mol]	$\overline{M}_w/\overline{M}_n$[d]
	M_1 [mol%]	M_2 [mol%]		N[b] [mol%]	M_1 [mol%]		
3a	80	20	53.0	2.65	55.5	4.52	1.36
3b	60	40	71.7	2.57	53.5	3.48	1.77
3c	50	50	72.0	2.43	44.0	4.27	1.57
3d	30	70	63.0	2.40	43.0	6.23	1.89
4a	70	30	83.0	2.26	48.0	5.20	1.87
4b	50	50	80.0	1.79	27.0	12.90	2.98
4c	30	70	75.0	1.95	33.0	4.37	2.35
4d	20	80	68.0	1.48	19.0	7.22	1.42

[a]AIBN concentration = 2% by weight with respect to the monomer mixtures; total monomer concentration = 10%.
[b]The average nitrogen content in the copolymer which was determined by elemental analysis.
[c]Number-average molecular weight by GPC measurement.
[d]Polydispersities by GPC measurement.

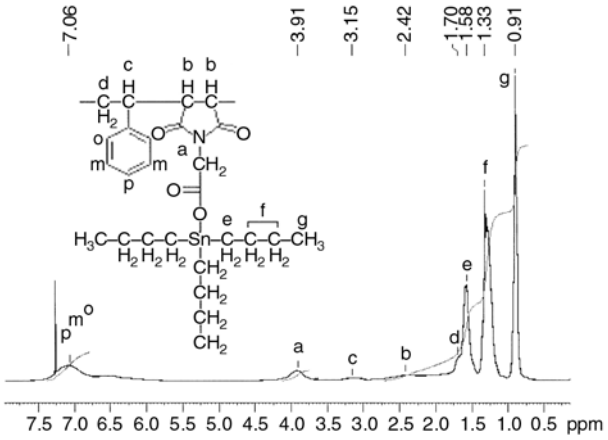

Figure 7. [1]H-NMR spectra of copolymer **3a**

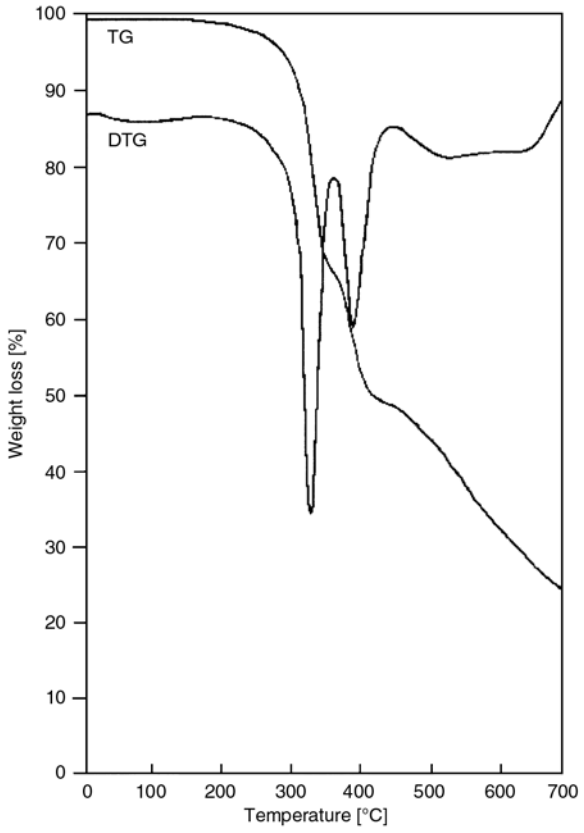

Figure 8. TGA curve of copolymer **3c**

attributed to the nonpolymeric trialkyltin carboxylate in the solid state (Figure 6) [11, 21–23]. A similar behaviour was found in other tin functionalized copolymers [24]. The [1]H-NMR spectra of copolymers displayed the expected resonance at 7.06 ppm (aromatic protons), 3.91 ppm (–COO–C<u>H</u>$_2$–N<), 3.15 ppm (C<u>H</u> of succinimide ring units), 2.42 ppm (C<u>H</u> of styrene units), 1.70 (C<u>H</u>$_2$ of styrene units), 1.58, 1.33 and 0.91 ppm (butyl rest) (Figure 7). Additionally, copolymers **4(a–d)** exhibited resonances in the range of 7.8–7.2 ppm attributed to p-substituted aromatic protons.

3.1. Thermal characterization

By processing TGA curves, thermal data presented in Table 2 resulted. The thermogravimetric curves of the copolymers showed three stages of decomposition. The first stage corresponding to the decomposition of tributyltin carboxylate groups range between 285–350°C for copolymers **3(a–d)** and 267–350°C for copolymers **4(a–d)**, and the weight loss varied with the content of tributyltin units in copolymer. The second stage of decomposition varied in the range of 335–415°C for copolymers **3(a–d)** and 345–440°C for copolymers **4(a–d)** and corresponded to the decomposition of polystyrene. The third stage of decomposition ranged between 375–750°C for copolymers **3(a–d)** and 415–750°C for copolymers **4(a–d)**. A representative TGA curve for copolymer **3** is presented in Figure 8. The inorganic residue left after heating at 750°C in air constituted by SnO_2, has a lower mass than that calculated for the copolymer structure which is clearly attributed to the sample volatility.
DSC measurements have been performed on the as prepared products, without any preliminary thermal conditioning, in order to avoid alterations of the materials and to obtain results directly comparable

Table 2. TGA data for copolymers **3(a–d)** and **4(a–d)**

Copolymer	IDT [°C]	Weight losses [%]/decomposition temperature ranges [°C]				Inorganic residue [%]	
		Global [%]	Step I	Step II	Step III	Calcd	Found
3a	303	80	38/303–355	23/355–415	19/415–750	23.6	20
3b	300	77	36/300–350	22/350–410	19/410–750	29.9	23
3c	298	78	32/298–350	18/350–410	28/410–750	26.1	22
3d	285	79	30/285–335	19/335–375	30/375–750	25.9	21
4a	267	79	28/267–345	12/345–440	39/440–750	24.4	21
4b	286	82	29/286–350	13/350–420	35/420–750	19.2	18
4c	295	80	28/295–345	12/345–415	30/415–750	21.0	20
4d	308	86	27/308–345	25/345–415	34/415–750	15.9	14

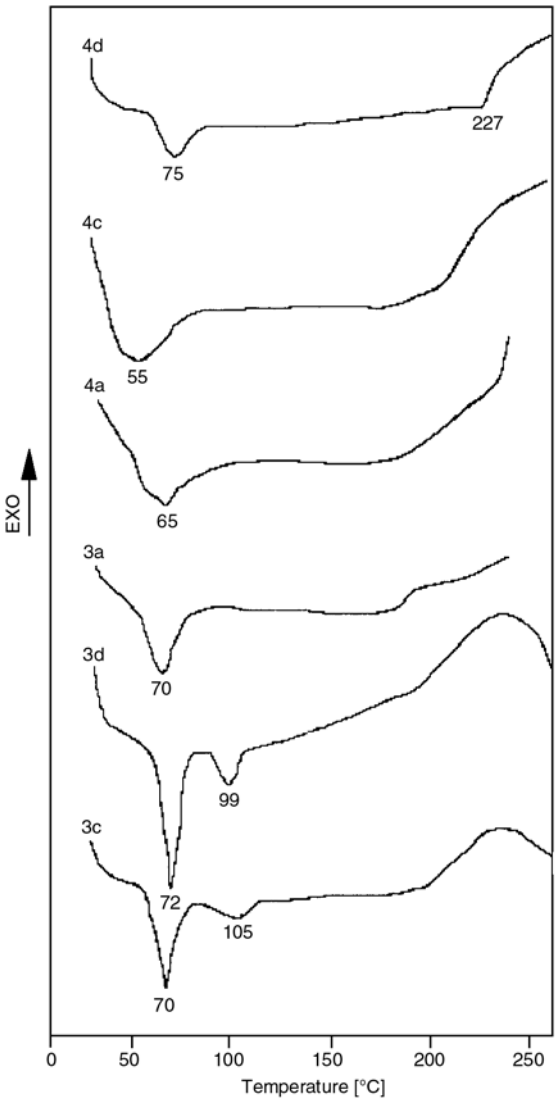

Figure 9. DSC scans of copolymers **3(a, c, d)** and **4(a, c, d)**

to the data afforded by the other solid state measurements. The copolymers **4(a–d)** showed broad endothermic peaks in the range of 55–75°C (Figure 9), whereas the copolymers **3(a–d)** displayed a sharp signal around 70–72°C, due to the crystalline domains in the materials, and a small endothermic peak around 100°C only for copolymers **3(c, d)** attributed to atactic polystyrene [11]. The crystalline domains in the materials can be attributed to oligomeric or polymeric tin moiety aggregation of variable extent, generating pentacoordinated tin atoms of the type depicted in Figure 6, structure A, connecting pendant triorganotin carboxylates bound to the polystyrene side-chains with one other [11].

4. Conclusions

New functional tributyltin carboxylate maleimide monomers were synthesized, characterized and copolymerized. The copolymerization with styrene under radical conditions affords in good yields the corresponding polymers having tributyltin carboxylate moiety covalently linked to the side chain of polystyrene backbone.

References

[1] Pellerito C., Nagy L., Pellerito L., Szorcsik A.: Biological activity studies on organotin(IV)$^{n+}$ complexes and parent compounds. Journal of Organometallic Chemistry, **691**, 1733–1747 (2006). DOI: 10.1016/j.jorganchem.2005.12.025

[2] Seyferth D., Masterman T. C.: Novel polymers containing carbon-anchored organotin groups. Applied Organometallic Chemistry, **8**, 335–349 (1994). DOI: 10.1002/aoc.590080408

[3] Mahmoud A. A., Shaaban A. F., Azab M. M., Messiha N. N.: Organotin polymers-XVI. Synthesis of *p*-acryloyloxybenzoic acid and *n*-methacryloyloxytetrabromo-phthalimide and copolymerizations with tri-n-butyltin acrylate and methacrylate. European Polymer Journal, **28**, 555–559 (1992). DOI: 10.1016/0014-3057(92)90133-M

[4] Dharia J. R., Pathak C. P., Babu G. N., Gupta S. K.: Organotin polymers. I. Copolymerization on tributyltin methacrylate with (hydroxy) alkyl methacrylates. Journal of Polymer Science Part A, Polymer Chemistry, **26**, 595–599 (1988). DOI: 10.1002/pola.1988.080260222

[5] Gielen M., Davies A. G., Pannell K., Tiekink E.: Tin chemistry: Fundamentals, frontiers, and applications. Wiley, Weinheim (2004).

[6] Otera J.: Transesterification. Chemical Reviews, **93**, 1449–1470 (1993). DOI: 10.1021/cr00020a004

[7] Otera J.: Toward ideal (trans)esterification by use of fluorous distannoxane catalysts. Accounts of Chemical Research, **37**, 288–296 (2004). DOI: 10.1021/ar030146d

[8] Barot G., Shahi K. R., Roner M. R., Carraher C. E.: Synthesis, structural characterization, and ability to inhibit cancer growth of a series of organotin poly(ethylene glycols). Journal of Inorganic and Organometallic Polymer and Materials, **17**, 595–603 (2007). DOI: 10.1007/s10904-007-9158-8

[9] Pruchnik F. P., Bańbula M., Ciunik Z., Latocha M., Skop B., Wilczok T.: Structure, properties and cytostatic activity of tributyltin carboxylates. Inorganica Chimica Acta, **356**, 62–68 (2003). DOI: 10.1016/S0020-1693(03)00475-4

[10] Tsagatakis J. K., Chaniotakis N. A., Damoun S., Geerlings P., Bouhdid A., Gielen M., Verbruggen I., Biesemans M., Martins J. C., Willem R.: Tributyl- and triphenyltin benzoates, phenylacetates, and cinnamates as anion carriers: An electrochemical assessment coupled to structural NMR studies and AM1 calculations. Helvetica Chimica Acta, **82**, 531–542 (1999).
DOI: 10.1002/(SICI)1522-2675(19990407)82:4<531::AID-HLCA531>3.0.CO;2-5

[11] Angiolini L., Biesemans M., Carreti D., Salatelli E., Willem R.: Synthesis and characterization of polystyrenes containing side-chain tributyltin carboxylate moieties linked to the aromatic ring through a 1,2-ethylene spacer. Polymer, **41**, 3913–3924 (2000).
DOI: 10.1016/S0032-3861(99)00648-5

[12] Angiolini L., Caretti D., Salatelli E., Mazzocchetti L., Willem R., Biesemans M.: Synthesis and characterization of new functional polystyrenes containing tributyltin carboxylate moieties linked to the aromatic ring by a trimethylene spacer. Journal of Inorganic and Organometallic Polymer and Materials, **18**, 236–245 (2008).
DOI: 10.1007/s10904-007-9166-8

[13] Subramanian R. V., Somasekharan K. N.: Polymers for controlled release of organotin toxin. Journal of Macromolecular Science, Part A: Pure and Applied Chemistry, **16**, 73–93 (1981).
DOI: 10.1080/00222338108082043

[14] Garg B. K., Corredor J., Subramanian V.: Copolymerization of Tri-n-butyltin acrylate and tri-n-butyltin methacrylate monomers with vinyl monomers containing functional groups. Journal of Macromolecular Science, Part A: Pure and Applied Chemistry, **11**, 1567–1601 (1977).
DOI: 10.1080/00222337708063077

[15] Ghanem N. A., Messiha N. N., Abd-El Malek M. M., Ikladious N. E., Shaaban A. F.: New terpolymers with pendent organotin moieties as antifouling coatings. Journal of Coatings Technology, **53**, 57–60 (1981).

[16] Al-Muaikel N. S., Al-Diab S. S., Al-Salamah A. A., Zaid A. M. A.: Synthesis and characterization of novel organotin monomers and copolymers and their antibacterial activity. Journal of Applied Polymer Science, **77**, 740–745 (2000).
DOI: 10.1002/(SICI)1097-4628(20000725)77:4<740::AID-APP4>3.0.CO;2-P

[17] Ahmad S., Ali S., Shahzadi S., Ahmed F., Khan K. M.: New complexes of organotin(IV) 2-(N-maleoylamino)-2-methylpropanoate: Synthesis, spectroscopic characterization and biological activity. Turkish Journal of Chemistry, **29**, 299–308 (2005).

[18] Amarego W. F. F., Chai C. L. L.: Purification of laboratory chemicals. Butter Worth, Oxford (2003).

[19] Gaina V., Gaina C.: Bismaleimides and biscitraconimides with bisallyl groups. High Performance Polymers, **19**, 160–174 (2007).
DOI: 10.1177/0954008306072497

[20] Rich D. H., Gasellchen P. D., Tong A., Cheung A., Buckner C. K.: Alkylating derivatives of amino acids and peptides. Synthesis of N-maleoylamino acids, [1-(N-maleoylglycyl)cysteinyl]oxytocin, and [1-(N-maleoyl-11-aminoundecanoyl) cysteinyl]oxytocin. Effects on vasopressin-stimulated water loss from isolated toad bladder. Journal of Medicinal Chemistry, **18**, 1004–1010 (1975).
DOI: 10.1021/jm00244a011

[21] Dalil H., Biesemans M., Teeenstra M., Willem R., Angiolini L., Salatelli E., Caretti D.: A novel approach to soluble polystyrenes functionalized by tri-n-butyltin carboxylates. Macromolecular Chemistry and Physics, **201**, 1266–1272 (2000).
DOI: 10.1002/1521-3935(20000801)201:12<1266::AID-MACP1266>3.0.CO;2-O

[22] Angiolini L., Salatelli E., Caretti D., Biesemans M., Dalil H., Willem R., Chaniotakis N. A., Gouliaditi E., Perdikaki K.: Synthesis and characterization of polymeric derivatives containing grafted triorganotin cinnamates with electrochemical chloride response. Macromolecular Chemistry and Physics, **203**, 219–229 (2002).
DOI: 10.1002/1521-3935(20020101)203:1<219::AID-MACP219>3.0.CO;2-C

[23] Dalil H., Biesemans M., Willem R., Angiolini L., Salatelli E., Caretti D., Chaniotakis N. A., Perdikaki K.: Soluble polystyrenes functionalized by triorgano[(1-oxoalkyl)oxy]stannanes (triorganotin carboxylates): Synthesis, structure, and anion-recognition characteristics. Helvetica Chimica Acta, **85**, 852–866 (2002).
DOI: 10.1002/1522-2675(200203)85:3<852::AID-HLCA852>3.0.CO;2-M

[24] Gaina C., Gaina V., Cristea M.: Poly(urethane-urea) varnishes containing tributhyltin groups. Journal of Inorganic and Organometallic Polymer and Materials, **19**, 157–165 (2009).
DOI: 10.1007/s10904-008-9230-z

eXPRESS Polymer Letters Vol.3, No.6 (2009) 359–365
Available online at www.expresspolymlett.com
DOI: 10.3144/expresspolymlett.2009.45

Synergistic effects of iron powder on intumescent flame retardant polypropylene system

X. L. Chen, C. M Jiao, Y. Wang*

College of Environment and Safety Engineering, Qingdao University of Science and Technology, Qingdao, Shandong 266042, P R China

Received 14 February 2009; accepted in revised form 30 March 2009

Abstract. The effects of iron powder as a synergistic agent on the flame retardancy of intumescent flame retardant polypropylene composites (IFR-PP) were studied. The thermogravimetric analysis (TGA) and cone calorimeter (CONE) were used to evaluate the synergistic effects of iron powder (Fe). The TGA data showed that Fe could enhance the thermal stability of the IFR-PP systems at high temperature and effectively increase the char residue formation. The CONE results revealed that Fe and IFR could clearly change the decomposition behavior of PP and form a char layer on the surface of the composites, consequently resulting in efficient reduction of the flammability parameters, such as heat release rate (HRR), mass loss (ML), Mass loss rate (MLR), total heat release (THR), carbon monoxide and so on. Thus, a suitable amount of Fe plays a synergistic effect in the flame retardancy of IFR composites.

Keywords: *polymer composites, flame retardant, combustion, polypropylene*

1. Introduction

Polypropylene (PP) is used in many fields, such as automobiles, furniture, electronic casings, interior decoration, and architectural material. However, due to its chemical constitution, the polymer is easily flammable and so flame retardancy becomes an important requirement for PP. Traditionally, halogen containing compounds, alone or in conjunction with antimony trioxide, are the main flame retardants for PP. However, the use of these flame retardants has been limited for the consideration of life safety and environmental problems [1]. Therefore, it is worthwhile to investigate the halogen-free flame retardation of PP. The compounds used as halogen-free flame retardants in PP include metal hydroxides, phosphorus-containing compounds, phosphorus and nitrogen-containing compounds, etc. Furthermore, metal hydroxides are widely used as flame retardant additives in polypropylene, but the high loading destroys the mechanical properties of polymeric materials [2–5].

In recent years, intumescent flame retardant (IFR) approach [6–12] was well known as a new generation of flame retardants in polypropylene and other polyolefins for some of their merits, such as very low smoke and toxic gases produced during burning, and antidripping property, which conform to the tendency of flame retardants' development. However, it has also some drawbacks compared with bromine-containing flame retardants [13], such as low thermal stability. In order to enhance the flame retardancy, new intumescent flame retardant systems have been found [14–17], which has high flame retardant efficiency and good water resistance ability; and synergistic agents have been used in IFR systems, such as zeolites [18, 19], montmorillonite [20, 21], organoboron siloxane [22, 23], and some transitional metal oxides and

*Corresponding author, e-mail: xlchen@qust.edu.cn

metal compounds [24–27]. Many researches have shown that synergistic agents can effectively increase the strength and stability of char layer [18, 28], and promote catalyzing the reactions among IFR components in IFR-PP systems.

Iron compounds can be used as flame retardant synergists [29–31]. Carty and co-workers have studied the effects of antimony(III) oxide and basic iron(III) oxide on the flammability and thermal stability of a tertiary polymer blend [29]. Cai and co-workers have studied the catalyzing carbonization function of ferric chloride based on acrylonitrile-butadiene-styrene copolymer/organophilic montmorillonite nanocomposites [30]. Zhang and co-workers have studied the influence of Fe-MMT on the fire retarding behavior and mechanical property of (ethylene-vinyl acetate copolymer/magnesium hydroxide) composite [31]. Up to now, iron powder has not been reported to improve the flame retardance of plastics.

In this work, iron powder is selected to investigate the synergistic effect in PP-IFR composites, it is used in an IFR system consisting of ammonium polyphosphate (APP) and pentaerythritol (PER). Thermogravimetric analysis (TGA) and cone calorimeter (CONE) are used to evaluate the synergistic effect of Fe in PP-IFR systems.

2. Experimental results

2.1. Materials

Polypropylene (F401) was provided by Yangzi Petroleum Chemical Company. APP and PER was supplied by Hefei Keyan Institute of Chemical Engineering; the intumescent flame retardant (IFR) was obtained with the mass ratio of APP and PER is 3:1. Iron powder (Fe), with the particle size of 80~150 nm, supplied from the First Reagent Co. of Shanghai, was used as received. The formulations are given in Table 1.

Table 1. Formulations of flame retarded PP composites

Sample code	PP [%]	IFR [%]	Fe [%]	LOI	UL 94
PP0	100.0	–	–	18.0	No rating
PP1	70.0	30.0	–	31.0	V-0
PP2	70.0	29.0	1.0	32.5	V-0
PP3	70.0	28.0	2.0	32.0	V-0
PP4	70.0	27.0	3.0	32.0	V-0
PP5	70.0	25.0	5.0	31.8	V-0

2.2. Preparation of samples

All samples were prepared on a two-roll mill at a temperature range of 170–175°C for 15 min. After mixing, the samples were hot-pressed under 10 MPa for 5 min at about 175°C into sheets of suitable thickness and size for analysis.

2.3. Measurements

2.3.1. Limiting oxygen index (LOI)

Limiting oxygen index (LOI) was measured according to ASTM D 2863. The apparatus used was an HC-2 oxygen index meter (Jiangning Analysis Instrument Company, China). The specimens used for the test were of dimensions 100×6.5×3 mm^3.

2.3.2. UL 94 testing

The vertical test was carried out on a CFZ-2-type instrument (Jiangning Analysis Instrument Company, China) according to the UL 94 test standard. The specimens used were of dimensions 130×13×3 mm^3.

2.3.3. Cone calorimeter

The cone calorimeter (Stanton Redcroft, UK) tests were performed according to ISO 5660 standard procedures. Each specimen of dimensions 100×100×3 mm^3 was wrapped in aluminium foil and exposed horizontally to an external heat flux of 35 kW/m^2.

2.3.4. Thermogravimetry (TG)

Each sample (approx. 10 mg) in powder form was examined in open vitreous silica pans under nitrogen flow on a STA 409C TGA apparatus (Netzsch Company, Germany) with crucible sample holders, at a heating rate of 10°C/min.

3. Results and discussion

3.1. LOI and UL 94 rating

The LOI and UL 94 tests are widely used to evaluate flame retardant properties of materials and to screen flame retardant formulations. Table 1 lists the related LOI and UL 94 data obtained from different loadings of iron powder. It can be seen from

Table 1 that the LOI value of PP1 containing 30.0 wt% IFR increases rapidly to 31.0 from 18.0 of original PP without any additive. The LOI values of samples (PP1 to PP2) increase to 32.5 with 1.0 wt% loading of Fe powder in the formulation. Then, the LOI decreases with the addition of iron powder. And, the LOI value of PP5 decreases to 31.8 when the loading of iron powder reaches to 5.0 wt%. This above result also gives the evidence that the 1.0 wt% iron powder has the best synergist effect with IFR in the PP blends. The results obtained from the UL 94 tests show that all the samples pass the UL 94 test.

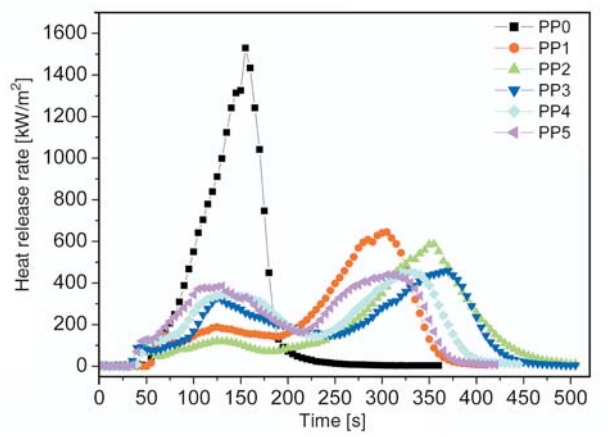

Figure 1. Heat release rate curves of flame retardant PP at a flux of 35 kW/m²

3.2. Cone calorimeter study

The cone calorimeter is one of the most effective bench scale methods for studying the flammability properties of materials. The heat release rate (HRR), particularly the peak HRR, has been found to be the most important parameter for evaluating fire safety [29, 32–35]. The flammability properties of flame retardant PP composites have been studied using cone calorimeter. Although intumescent flame retardant is commonly used for PP for fire safety materials, sometimes the high loading can deteriorate the mechanical properties of materials. It is necessary, therefore, to develop novel synergistic flame-retardant systems with high efficiency and acceptable environmental impact.

In this study, Fe is added into PP/IFR composites as synergist. The flammability properties were evaluated with cone calorimeter experiments. In the flame retardant PP/IFR/Fe composites, the mass fraction of IFR and Fe was 30 wt%. The HRR curves are shown in Figure 1. A synergistic effect can be seen between IFR and Fe. Figure 1 shows that when 30 wt% IFR was added to pure PP, the peak HRR was 650 kW/m². When the 1 wt% IFR was substituted with Fe (PP2), the curves show that the peak HRR of the sample was 591 kW/m². It should be noted that the time for peak HRR moves from 304 s (PP0) to 353 s (PP1). When the Fe loading is raised to 2 wt%, the peak HRR of PP3 can further reduced to 461 kW/m². Also, the time for peak HRR delays to 368 s. It is very interesting that there is peak HRR when the burning time is about 124 s. This phenomenon can be explained that proper Fe can promote the formation of good carbon char residue, which can isolate heat and oxygen from flame zone to the substrate and barrier combustible gas degraded from the substrate from flame. With the addition of Fe, the peak HRR can be further decreased, but the decline rates have been not obvious. And, the time for peak HRR shortens with the loading of Fe from PP3 to PP5. Furthermore, the first peak HRR increases with the addition of Fe from PP2 to PP5. This can be explained that high loading of Fe on the surface can be oxidized, giving off a lot of heat, which leads the first peak HRR increases. Another reason may be that the iron powder in the bottom of the sample can catalyze PP depolymerisation, which results in many combustible gases.

The primary parameter which was responsible for HRR of the samples filled with IFR is the mass loss rate (MLR) during combustion, which was significantly reduced compared with those values observed for the pure polymer. Figure 2 shows that the MLR decreased in the order of PP2>PP1>PP3>PP4>

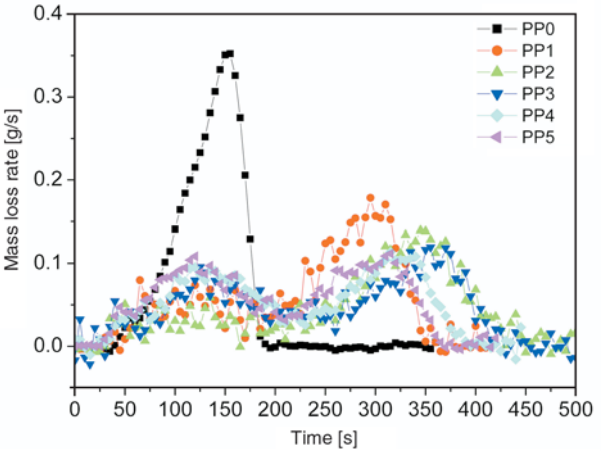

Figure 2. Mass loss rate curves of flame retardant PP at a flux of 35 kW/m²

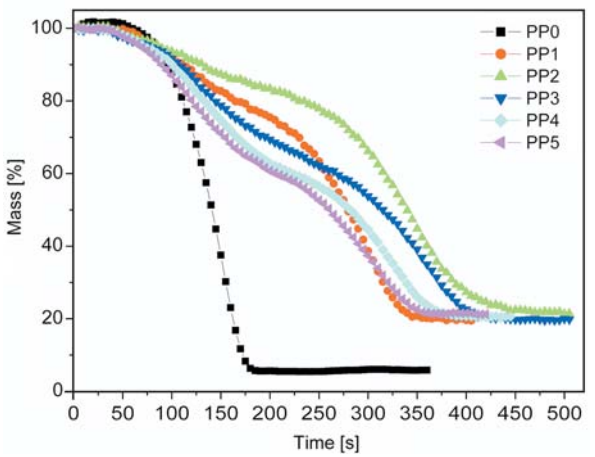

Figure 3. Mass curves of flame retardant PP at a flux of 35 kW/m^2

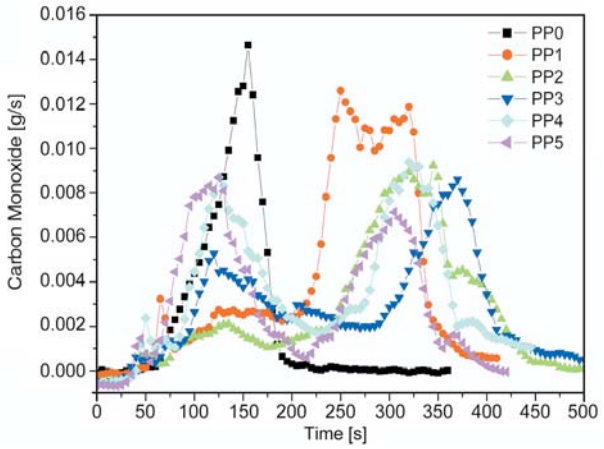

Figure 4. Carbon monoxide curves of flame retardant PP at a flux of 35 kW/m^2

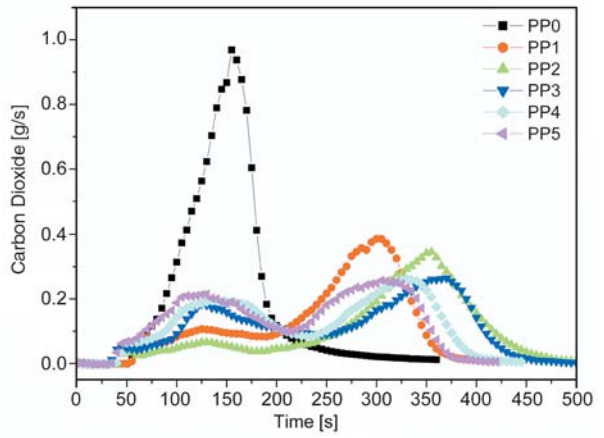

Figure 5. Carbon dioxide curves of flame retardant PP at a flux of 35 kW/m^2

PP5>PP0 between 0 and 200 s, and the MLR decreased in the order of PP5>PP4>PP3>PP2>PP1 between 200 and 450 s. This trend is the same as those of the HRR in the cone calorimeter (Figure 1). These similarities indicate that the mechanism of the observed reduction in HRR and also in MLR depends mainly on the condensed phase process instead of the gas phase process.

Figure 3 shows the weight of the char residues. During combustion, proper Fe may promote the IFR to carbonization on the surface of the burning composite creating a physical protective barrier on the surface of material. From Figure 3, it can be seen that the mass loss of PP2 is much less than that of the other sample, which can be showed that a dense protective barrier formed on the sample. It can explain the fact that the heat release rate of PP2 is the lowest one among all the samples. The physical process of the layers reassembling would act as a protective barrier in addition to the intumescent shield and can thus limit the oxygen diffusion to the substrate or give a less disturbing low volatilization rate.

Figure 4 and Figure 5 show the CO and CO_2 produced from PP and flame retardant PP under a heat flux of 35 kW/m^2. The incomplete combustion of flame retardant composite systems can be seen in the CO production rate. From Figure 4, it can be seen that the CO production rate of PP2 is the lowest one among all the flame retardant samples. Furthermore, the first peak of the CO production rate increases and the second peak of the CO production rate decreases with the addition of Fe. This phenomenon can be explained by that metallic Fe can promote the formation of carbon char residue, which can block heat. So the combustible gases on the surface of the sample can complete combustion. With the addition of Fe, the first peak of the CO production rate increases. This phenomenon may be that iron promotes a depolymerisation process. Many combustible gases cause incomplete combustion. However, the second peak of the CO production rate decreases with the addition of Fe. This can be illustrated that more iron powder is added, more iron oxides will be formed, which can oxidize CO into CO_2.

The CO_2 production rates of the flame retardant systems significantly decrease at the time between 220 and 470 s, because the dense and compact char structure formed on the surface of the sample. However, in the time between 0 and 200 s, only the CO_2 production rate of PP2 is lower than PP1. Furthermore, the CO_2 production rate increases with

the addition of Fe from PP2 to PP5. It can be explained that higher loading of Fe can lead more heat release (Figure 1). So a large number of combustible gases released, and reacted with oxygen to form carbon dioxide.

3.3. Thermogravimetric (TG) analysis

Figure 6 shows the TG curves of the pure PP and its flame retardant composites. It is clearly seen that all flame retardant PP composites decompose early in comparison with PP, which begins to decompose at about 399°C. However, at a temperature higher than 419°C, the FR PP composites are more thermally stable than PP. For example, PP almost decomposes completely at 500°C, whereas the undecomposed parts at the same temperature for PP1, PP2, PP3, PP4 and PP5 are 14.4, 15.4, 17.6, 18.6 and 19.5%, respectively. The above results showed that IFR has very good carbonization performance. The phenomenon that the char residue increases with the addition of iron powder can be illustrated that the quality of iron powder will only increase rather than decrease during combustion. The amount of residue of the FR PP composites at 600°C is still higher than 12.7%. The char residue increases with the addition of Fe. The reason may be that the reaction between Fe and oxygen can lead the mass increased, and Fe or Fe oxide can catalyze PP or intumescent flame retardant to form char residue. Fe oxide on the surface of the char residue can protect the underlying substrate from further decomposition.

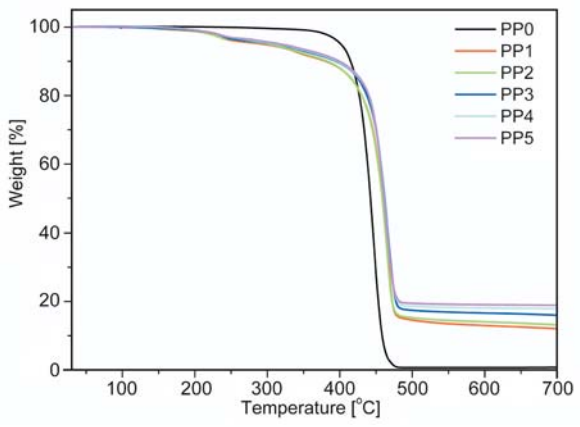

Figure 6. Thermal analysis curves of flame retardant PP

4. Conclusions

Flame retardant polypropylene composites were prepared by melt blending starting from APP, PER and Fe with the polymer matrix. The incorporation of Fe into IFR (APP+PER) leads to a remarkable influence on charring of PP formulations as revealed by TGA and CONE data. Cone data gives a measure of the size of the fire. It is confirmed that Fe acts as an effective additive functioning as flame retardant synergist. There is a synergistic effect occurred when Fe and IFR are both present in polypropylene composites.

Acknowledgements

The National Natural Science Foundation of China (No. 50876048) is gratefully acknowledged.

References

[1] Sen A. K., Mukherjee B., Bhattacharya A. S., Sanghi L., De K., P. P., Bhowmick A. K.: Preparation and characterization of low-halogen and nonhalgoen fire-resistant low-smoke (FRLS) cable sheathing compound from blends of functionalized polyolefins and PVC. Journal of Applied Polymer Science, **43**, 1673–1684 (1991).
DOI: 10.1002/app.1991.070430910

[2] Wittek T., Tanimoto T.: Mechanical properties and fire retardancy of bidirectional reinforced composite based on biodegradable starch resin and basalt fibres. Express Polymer Letters, **2**, 810–822 (2008).
DOI: 10.3144/expresspolymlett.2008.94

[3] Sanchez-Olivares G., Sanchez-Solis A., Camino G., Manero O.: Study on the combustion behavior of high impact polystyrene nanocomposites produced by different extrusion processes. Express Polymer Letters, **2**, 569–578 (2008).
DOI: 10.3144/expresspolymlett.2008.69

[4] Plentz R. S., Miotto M., Schneider E. E., Forte M. S. M. C., Mauler R. S., Nachtigall S. M. B.: Effect of a macromolecular coupling agent on the properties of aluminum hydroxide/PP composites. Journal of Applied Polymer Science, **101**, 1799–1805 (2006).
DOI: 10.1002/app.23558

[5] Hong C. H., Lee Y. B., Bae J. W., Jho J. Y., Nam B. U., Chang D-H., Yoon S. H., Lee K. J.: Tensile properties and stress whitening of polypropylene/polyolefin elastomer/magnesium hydroxide flame retardant composites for cable insulating application. Journal of Applied Polymer Science, **97**, 2311–2318 (2005).
DOI: 10.1002/app.21776

[6] Li B., Xu M. J.: Effect of a novel charring-foaming agent on flame retardancy and thermal degradation of intumescent flame retardant polypropylene. Polymer Degradation and Stability, **91**, 1380–1386 (2006). DOI: 10.1016/j.polymdegradstab.2005.07.020

[7] Riva A., Camino G., Fomperie L., Amiqouët P.: Fire retardant mechanism in intumescent ethylene vinyl acetate compositions. Polymer Degradation and Stability, **82**, 341–346 (2003). DOI: 10.1016/S0141-3910(03)00191-5

[8] Le Bras M., Bourbigot S., Christelle D., Siat C., Le Tallec Y.: New intumescent formulations of fire-retardant polypropylene-discussion of the free radical mechanism of the formation of carbonaceous protective material during the thermo-oxidative treatment of the additives. Fire and Materials, **20**, 191–203 (1996). DOI: 10.1002/(SICI)1099-1018(199607)20:4<191::AID-FAM577>3.0.CO;2-S

[9] Almeras X., Le Bras M., Hornsby P., Bourbigot S., Marosi Gy., Keszei S., Poutch F.: Effect of fillers on the fire retardancy of intumescent polypropylene compounds. Polymer Degradation and Stability, **82**, 325–331 (2003). DOI: 10.1016/S0141-3910(03)00187-3

[10] Almeras X., Le Bras M., Poutch F., Bourbigot S., Marosi G., Anna P.: Effect of fillers on fire retardancy of intumescent polypropylene blends. Macromolecular Symposia, **198**, 435–447 (2003). DOI: 10.1002/masy.200350837

[11] Chen Y. H., Wang Q.: Preparation, properties and characterizations of halogen-free nitrogen-phosphorous flame-retarded glass fiber reinforced polyamide 6 composite. Polymer Degradation and Stability, **91**, 2003–2013 (2006). DOI: 10.1016/j.polymdegradstab.2006.02.006

[12] Weil E. D., Levchik S.: Current practice and recent commercial developments in flame retardancy of polyamides. Journal of Fire Sciences, **22**, 251–264 (2004). DOI: 10.1177/0734904104040546

[13] Camino G., Grassie N., McNeill I. C.: Influence of the fire retardant, ammonium polyphosphate on the thermal degradation of poly(methyl methacrylate). Journal of Polymer Science Part A: Polymer Chemistry, **16**, 95–106 (1978). DOI: 10.1002/pol.1978.170160110

[14] Li B., Xu M. J.: Effect of a novel charringe-foaming agent on flame retardancy and thermal degradation of intumescent flame retardant. Polymer Degradation and Stability, **91**, 1380–1386 (2006). DOI: 10.1016/j.polymdegradstab.2005.07.020

[15] Allen D. W., Edwyn C., Shiel L. E.: Structure-property relationships in intumescent fire retardant derivatives of 4-hydroxymethyl-2,6,7-trioxa-1-phosphabicyclo[2,2,2]octane-1-oxide anderton. Polymer Degradation and Stability, **45**, 399–408 (1994). DOI: 10.1016/0141-3910(94)90210-0

[16] Hu X-P., Li Y-L., Wang Y-Z.: Synergistic effect of the charring agent on the thermal and flame retardant properties of polyethylene. Macromolecular Materials and Engineering, **289**, 208–212 (2004). DOI: 10.1002/mame.200300189

[17] Almeras X., Dabrowski F., Le Bras M., Delobel R., Bourbigot S., Marosi G., Anna P.: Using polyamide 6 as charring agent in intumescent polypropylene formulations. II. Thermal degradation. Polymer Degradation and Stability, **77**, 315–323 (2002). DOI: 10.1016/S0141-3910(02)00066-6

[18] Demir H., Arkiş E., Balköse D., Ülkü S.: Synergistic effect of natural zeolites on flame retardant additives. Polymer Degradation and Stability, **89**, 478–483 (2005). DOI: 10.1016/j.polymdegradstab.2005.01.028

[19] Bourbigot S., Le Bras M., Delobel R., Bréant P., Tremillon J. M.: 4A zeolite synergistic agent in new flame retardant intumescent formulations of polyethylenic polymers-study of the effect of the constituent monomers. Polymer Degradation and Stability, **54**, 275–287 (1996). DOI: 10.1016/S0141-3910(96)00055-9

[20] Tang Y., Hu Y., Wang S. F., Gui Z., Chen Z. Y., Fan W. C.: Intumescent flame retardant-montmorillonite synergism in polypropylene-layered silicate nanocomposites. Polymer International, **52**, 1396–1400 (2003). DOI: 10.1002/pi.1270

[21] Tang Y., Hu Y., Li B. G., Liu L., Wang Z. Z., Chen Z. Y., Fan W. C.: Polypropylene/montmorillonite nanocomposites and intumescent, flame-retardant montmorillonite synergism in polypropylene nanocomposites. Journal of Polymer Science Part A: Polymer Chemistry, **42**, 6163–6173 (2004). DOI: 10.1002/pola.20432

[22] Ravadits I., Tóth A., Marosi G., Márton A., Szép A.: Organosilicon surface layer on polyolefins to achieve improved flame retardancy through an oxygen barrier effect. Polymer Degradation and Stability, **74**, 419–422 (2001). DOI: 10.1016/S0141-3910(01)00179-3

[23] Marosi G., Márton A., Anna P., Bertalan G., Marosföi B., Szép A.: Ceramic precursor in flame retardant systems. Polymer Degradation and Stability, **77**, 259–265 (2002). DOI: 10.1016/S0141-3910(02)00057-5

[24] Estevao L. R. M., Le Bras M., Delobel R., Nascimento R. S. V.: Spent refinery catalyst as a synergistic agent in intumescent formulations: Influence of the catalyst's particle size and constituents. Polymer Degradation and Stability, **88**, 444–455 (2005). DOI: 10.1016/j.polymdegradstab.2004.11.016

[25] Wu Q., Qu B. J.: Synergistic effects of silicotungistic acid on intumescent flame-retardant polypropylene. Polymer Degradation and Stability, **74**, 255–261 (2001). DOI: 10.1016/S0141-3910(01)00155-0

[26] Liu Y., Wang Q.: Catalytic action of phospho-tungstic acid in the synthesis of melamine salts of pentaerythritol phosphate and their synergistic effects in flame retarded polypropylene. Polymer Degradation and Stability, **91**, 2513–2519 (2006).
DOI: 10.1016/j.polymdegradstab.2006.03.009

[27] Li Y., Li B., Dai J., Jia H., Gao S..: Synergistic effects of lanthanum oxide on a novel intumescent flame retardant polypropylene system. Polymer Degradation and Stability, **93**, 9–16 (2008).
DOI: 10.1016/j.polymdegradstab.2007.11.002

[28] Li J. M., Wilkie C. A.: Improving the thermal stability of polystyrene by Friedel-Crafts chemistry. Polymer Degradation and Stability, **57**, 293–299 (1997).
DOI: 10.1016/S0141-3910(97)00013-X

[29] Zanetti M., Camino G., Thomann R., Mülhaupt R.: Synthesis and thermal behaviour of layered silicate-EVA nanocomposites. Polymer, **42**, 4501–4507 (2001).
DOI: 10.1016/S0032-3861(00)00775-8

[30] Cai Y. B., Hu Y., Song L., Xuan S. Y., Zhang Y., Chen Z. Y., Fan W. C.: Catalyzing carbonization function of ferric chloride based on acrylonitrile-butadiene-styrene copolymer/organophilic montmorillonite nanocomposites. Polymer Degradation and Stability, **92**, 490–496 (2007).
DOI: 10.1016/j.polymdegradstab.2006.08.029

[31] Zhang Y., Hu Y., Song L., Wu J., Fang S. L.: Influence of Fe-MMT on the fire retarding behavior and mechanical property of (ethylene-vinyl acetate copolymer/magnesium hydroxide) composite. Polymers for Advanced Technologies, **19**, 960–966 (2008).
DOI: 10.1002/pat.1059

[32] Zanetti M., Kashiwagi T., Falqui L., Camino G.: Cone calorimeter combustion and gasification studies of polymer layered silicate nanocomposites. Chemistry of Materials, **14**, 881–887 (2002).
DOI: 10.1021/cm011236k

[33] Gilman J. W., Jackson C. L., Morgan A. B., Harris R., Manias J. E., Giannelis E. P., Wuthenow M., Hilton D., Phillips S. H.: Flammability properties of polymer-layered-silicate nanocomposites. Polypropylene and polystyrene nanocomposites. Chemistry of Materials, **12**, 1866–1873 (2000).
DOI: 10.1021/cm0001760

[34] Chiu S-H., Wang W-K.: Dynamic flame retardancy of polypropylene filled with ammonium polyphosphate, pentaerythritol and melamine additives. Polymer, **39**, 1951–1955 (1998).
DOI: 10.1016/S0032-3861(97)00492-8

[35] Dabrowski F., Le Bras M., Cartier L., Bourbigot S.: The use of clay in an EVA-based intumescent formulation. Comparison withthe intumescent formulation using polyamide-6 clay nanocomposite as carbonisation agent. Journal of Fire Sciences, **19**, 219–241 (2001).

eXPRESS Polymer Letters Vol.3, No.6 (2009) 366–375
Available online at www.expresspolymlett.com
DOI: 10.3144/expresspolymlett.2009.46

Starch-based completely biodegradable polymer materials

D. R. Lu, C. M. Xiao, S. J. Xu*

College of Material Science and Engineering of Huaqiao University, Quanzhou, 362021, P. R. China

Received 21 February 2009; accepted in revised form 30 March 2009

Abstract. Starch is a natural polymer which possesses many unique properties and some shortcoming simultaneously. Some synthetic polymers are biodegradable and can be tailor-made easily. Therefore, by combining the individual advantages of starch and synthetic polymers, starch-based completely biodegradable polymers (SCBP) are potential for applications in biomedical and environmental fields. Therefore it received great attention and was extensively investigated. In this paper, the structure and characteristics of starch and some synthetic degradable polymers are briefly introduced. Then, the recent progress about the preparation of SCBP via physical blending and chemical modification is reviewed and discussed. At last, some examples have been presented to elucidate that SCBP are promising materials for various applications and their development is a good solution for reducing the consumption of petroleum resources and environmental problem.

Keyword: *biodegradable polymers, starch, biopolymer, preparation, application*

1. Introduction

As well known, synthetic polymer materials have been widely used in every field of human activity [1] during last decades, i.e. post-Staudinger times. These artificial macromolecular substances are usually originating from petroleum and most of the conventional ones are regarded as non-degradable. However, the petroleum resources are limited and the blooming use of non-biodegradable polymers has caused serious environmental problems. In addition, the non-biodegradable polymers are not suitable for temporary use such as sutures. Thus, the polymer materials which are degradable and/or biodegradable have being paid more and more attention since 1970s.

Both synthetic polymers and natural polymers that contain hydrolytically or enzymatically labile bonds or groups are degradable. The advantages of synthetic polymers are obvious, including predictable properties, batch-to-batch uniformity and can be tailored easily [2]. In spite of this, they are quite expensive. This reminds us to focus on natural polymers, which are inherently biodegradable [3] and can be promising candidates to meet different requirements.

Among the natural polymers, starch is of interest. It is regenerated from carbon dioxide and water by photosynthesis in plants [4]. Owing to its complete biodegradability [5], low cost and renewability [6], starch is considered as a promising candidate for developing sustainable materials. In view of this, starch has been receiving growing attention since 1970s [7, 8]. Many efforts have been exerted to develop starch-based polymers for conserving the petrochemical resources, reducing environmental impact and searching more applications [9–11]. In this paper, the status of preparation and applications of starch-based completely biodegradable (SCBP) polymers is reviewed and presented.

*Corresponding author, e-mail: congmingxiao@hqu.edu.cn

2. Structure and properties of starch

Starch is mainly composed of two homopolymers of D-glucose [8]: amylase, a mostly linear α-D(1, 4')-glucan and branched amylopectin, having the same backbone structure as amylose but with many α-1, 6'-linked branch points (Figure 1). There are a lot of hydroxyl groups on starch chains, two secondary hydroxyl groups at C-2 and C-3 of each glucose residue, as well as one primary hydroxyl group at C-6 when it is not linked. Evidently, starch is hydrophilic. The available hydroxyl groups on the starch chains potentially exhibit reactivity specific for alcohols. In other words, they can be oxidized and reduced, and may participate in the formation of hydrogen bonds, ethers and esters [12].

Starch has different proportions of amylose and amylopectin ranging from about 10–20% amylose and 80–90% amylopectin depending on the source [13]. Amylose is soluble in water and forms a helical structure [14]. Starch occurs naturally as discrete granules since the short branched amylopectin chains are able to form helical structures which crystallize. Starch granules exhibit hydrophilic properties and strong inter-molecular association via hydrogen bonding formed by the hydroxyl groups on the granule surface.

Owing to its hydrophilicity, the internal interaction and morphology of starch will be readily changed by water molecules, and thereby its glass transition temperature (T_g), the dimension and mechanical properties depend on the water content. T_g of native starch can be as low as 60 to 80°C when the weight fraction of water is in the range 0.12 to 0.14, which allows starch to be successfully injection moulded to obtain thermoplastic starch polymers in the presence of water [15]. On the other hand, the hydrophilicity of starch can be used to improve the degradation rate of some degradable hydrophobic polymers, which will be shown in 3.1.1.

Starch is totally biodegradable in a wide variety of environments. It can be hydrolyzed into glucose by microorganism or enzymes, and then metabolized into carbon dioxide and water [16]. It is worth noting that carbon dioxide will recycle into starch again by plants and sunshine. Starch itself is poor in processability, also poor in the dimensional stability and mechanical properties for its end products [17]. Therefore, native starch is not used directly.

3. Preparation of starch-based biodegradable polymers

To improve the properties of starch, various physical or chemical modifications of starch such as blending, derivation and graft copolymerization have been investigated.

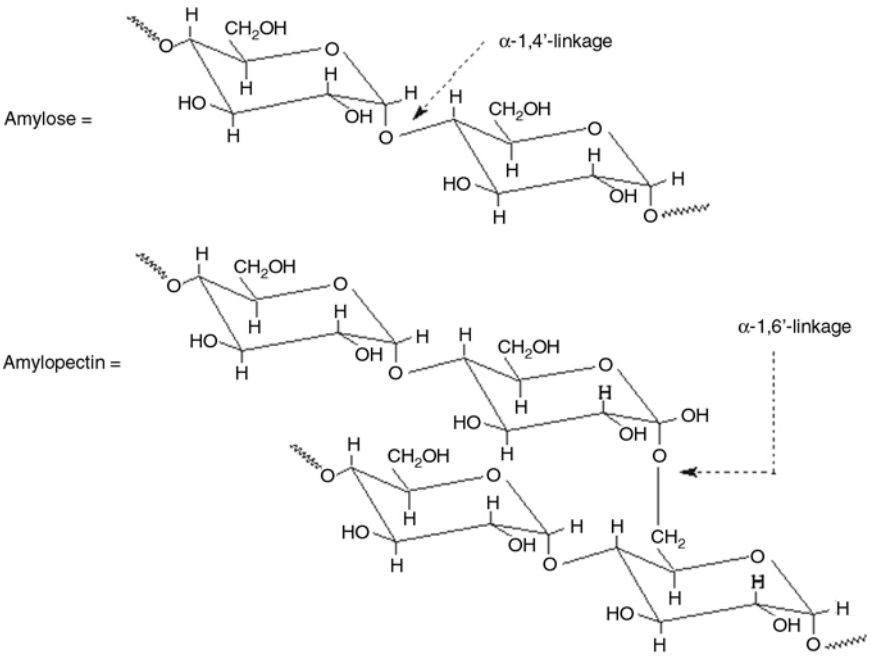

Figure 1. Molecular structure of starch

3.1. Physical blends

3.1.1. Blend with synthetic degradable polymers

At first, starch was adopted as a filler of polyolefin by Griffin [18] and its concentrations is as low as 6–15%. Attempts to enhance the biodegradability of the vinyl polymers have been investigated by incorporating starch to a carbon-carbon backbone matrix [19]. In all these cases starch granules were used to increase the surface area available for attack by microorganisms. However, such a system is partially biodegradable and not acceptable from an ecological point of view. Thus, the blends of starch and polyolefin will not be mentioned any more in this article.

To prepare completely biodegradable starch-based composites by this strategy, biodegradable polymers are assumed. Usually, the components to blend with starch are aliphatic polyesters, polyvinyl alcohol (PVA) and biopolymers. The commonly used polyesters are poly(β-hydroxyalkanoates) (PHA), obtained by microbial synthesis, and polylactide (PLA) or poly(ε-caprolactone) (PCL), derived from chemical polymerization. The goal of blending completely degradable polyester with low cost starch is to improve its cost competitiveness whilst maintaining other properties at an acceptable level [20, 21].

PLA is one of the most important biodegradable polyesters with many excellent properties and has been widely applied in many fields, especially for biomedical one. PLA possesses good biocompatibility and processability, as well as high strength and modulus. However, PLA is very brittle under tension and bend loads and develops serious physical aging during application. Moreover, PLA is a much more expensive material than the common industrial polymers [22].

Many efforts have been made to develop PLA/starch blends to reduce total raw materials cost and enhance their degradability. The major problem of this blend system is the poor interfacial interaction between hydrophilic starch granules and hydrophobic PLA. Mechanical properties of blends of PLA and starch using conventional processes are very poor because of incompatibility [23]. In order to improve the compatibility between hydrophilic starch granules and hydrophobic PLA, glycerol, formamide, and water are used alone or combined as plasticizers to enhance the dispersion and the interfacial affinity in thermoplastic starch (TPS)/PLA blends. In the presence of water and other plasticizers including glycerol, sorbitol, urea, and formamide [24], the strong intermolecular and intramolecular hydrogen bonds in starch can be weakened.

To improve the compatibility between PLA and starch, suitable compatibilizer should be added. Besides, gelatinization of starch is also a good method to enhance the interfacial affinity. Starch is gelatinized to disintegrate granules and overcome the strong interaction of starch molecules in the presence of water and other plasticizers, which leads to well dispersion [25, 26]. The glass transition temperature and mechanical properties of TPS/PLA blend depend on its composition and the content of plasticizer as well (Table 1), indicating the compatibility between PLA and TPS is low but some degree of interaction is formed [26].

PCL is another important member of synthetic biodegradable polymer family. It is linear, hydrophobic, partially crystalline polyester, and can be slowly degraded by microbes [27–29]. Blends between starch and PCL have been well documented in the literatures [30–35]. The weakness of pure starch materials including low resilience, high moisture sensitivity and high shrinkage has been overcome by adding PCL to starch matrix even at low PCL concentration. Blending with PCL, the

Table 1. Thermal and mechanical properties of thermoplastic starch/polylactide (TPS/PLA) blends

Content of TPS [wt%]	T_g [°C]		Tensile Strength [MPa]	Elongation at Break [%]
	PLA	TPS		
100 (TPS1)[a]	–	10	3.4	152.0
90 (TPS1)	47	NF[b]	2.9	48.8
75 (TPS1)	53	NF	4.8	5.7
100 (TPS2)[a]	–	43	19.5	2.8
90 (TPS2)	NF	NF	14.1	1.3
75 (TPS2)	NF	NF	12.0	0.9
0	58	–	68.4	9.4

[a]the content of glycerol and water in TPS1 and TPS2 are 18 and 12, 10 and 16 wt% respectively

[b]T_g value is not found in the literature

Table 2. Thermal and mechanical properties of thermoplastic starch/polycaprolactone (TPS/PCL) blends

Content of TPS [wt%]	T_g [°C]		Tensile Strength [MPa]	Elongation at Break [%]
	PCL	TPS		
100 (TPS1)[a]	–	8.4	3.3	126.0
75 (TPS1)	31.0		5.9	62.6
100 (TPS2)[a]	–	43.4	21.4	3.8
75 (TPS2)	41		10.5	2.0
60 (TPS2)	NF[b]		9.0	2.4
0	–61.5	–	14.2	>550.0

[a]the content of glycerol and water in TPS1 and TPS2 are 18 and 12, 10 and 16 wt% respectively
[b]T_g value is not found in the literature

impact resistance and the dimensional stability of native starch is improved significantly. The glass transition temperature and mechanical properties of TPS/PCL blend are varied with its composition and the content of plasticizer (Table 2) [32]. As can be seen, TPS/PCL blend is similar to TPS/PLA blend in both the compatibility and the role of components.

PCL/starch blends can be further reinforced with fiber and nano-clay respectively. Moreover, the other properties of the blends such as hydrolytic stability, degradation rate, and compatibilization between PCL and starch are also improved [34, 35].

PVA is a synthetic water-soluble and biodegradable polymer [36]. PVA has excellent mechanical properties and compatibility with starch. PVA/starch blend is assumed to be biodegradable since both components are biodegradable in various microbial environments. The biodegradability of blends consisting of starch, PVA, glycerol and urea is performed by bacteria and fungi isolated from the activated sludge of a municipal sewage plant and landfill, which indicate that microorganisms consumed starch and the amorphous region of PVA as well as the plasticizers [37]. Meanwhile, the blend is expected to exhibit good mechanical and process properties [38, 39]. Owing to the strong interaction among hydroxyl groups on PVA and starch chains, all the T_g of the starch/PVA blends of different compositions are lower than that of PVA. The excellent compatibility of two components make the tensile strength of the blend increases with increasing PVA concentration, and the elongation at break of the blend is almost kept constant [37].

In addition, PVA can be used to enhance the compatibility of starch/PLA blends. Because both starch and PVA are polyols, starch will form continuous phase with PVA during blending. As a result, the mechanical properties of the starch/PLA blends are improved in the presence of PVA [40]. As for the blend system without PVA, starch acts as filler in the PLA continuous matrix. PLA acts as the main load-bearing phase because of the weak interaction between starch and PLA.

3.1.2. Blend with biopolymers

Natural polymers such as chitosan and cellulose and their derivatives are inherently biodegradable, and exhibit unique properties. A number of investigations have been devoted to study the blend of them with starch.

Starch and chitosan are abundant naturally occurring polysaccharide. Both of them are cheap, renewable, non-toxic, and biodegradable [41]. The starch/chitosan blend exhibits good film forming property, which is attributed to the inter- and intramolecular hydrogen bonding that formed between amino groups and hydroxyl groups on the backbone of two components. The mechanical properties, water barrier properties, and miscibility of biodegradable blend films are affected by the ratio of starch and chitosan [42].

Extrusion of the mixture of corn starch and microcrystalline cellulose in the presence or absence of plasticizers (polyols) is used to produce edible films [43]. By increasing the content of the cellulose component, the rupture strength is increased, whereas the elongation at break and the permeability of films for water vapor are decreased. Starch can form thermodynamically compatible blend films with water-soluble carboxymethylcellulose (CMC) when the starch content is below 25 mass% [44]. Such films are biodegradable in presence of microorganisms.

Starch-based nanocomposite film is obtained by casting the mixture of plasticized starch and flax cellulose nanocrystals. The mechanical properties

and water resistance are greatly improved. The tensile strength of nanocomposite and unreinforced films are 498.2 and 11.9 MPa respectively [45].

3.2. Chemical derivatives

One problem for starch-based blends is that starch and many polymers are non-miscible, which leads to the mechanical properties of the starch/polymer blends generally become poor. Thus, chemical strategies are taken into consideration.

Chemical modifications of starch are generally carried out via the reaction with hydroxyl groups in the starch molecule [46]. The derivatives have physicochemical properties that differ significantly from the parent starch but the biodegradability is still maintained. Consequently, substituting the hydroxyl groups with some groups or chains is an effective means to prepare starch-based materials for various needs.

Graft copolymerization is an often used powerful means to modify the properties of starch. Moreover, starch-g-polymer can be used as an effective compatibilizer for starch-based blends [47–49].

PCL and PLA are chemically bonded onto starch and can be used directly as thermoplastics or compatibilizer. The graft-copolymers starch-g-PCL and starch-g-PLA can be completely biodegraded under natural conditions and exhibit improved mechanical performances. To introduce PCL or PLA segments onto starch, the ring opening graft polymerization of ε-caprolactone or L-lactide with starch is carried out [17, 31, 50, 51].

Starch-g-poly(vinyl alcohol) can be prepared via the radical graft copolymerization of starch with vinyl acetate and then the saponification of the starch-g-poly(vinyl acetate). Starch-g-PVA behaves good properties of both components such as processability, hydrophilicity, biodegradability and gelation ability [52–56].

Starch can be easily transformed into an anionic polysaccharide via chemical functionalization [57]. For instance, a carboxylic derivative of starch, maleic starch half-ester acid (MSA), has been prepared via the esterification of starch with maleic anhydride in the presence of pyridine [58]. MSA is an anionic polyelectrolyte, consequently it can perform ionic self-assembly with chitosan in aqueous solution and forms a polysaccharide-based polyelectrolyte complex [59].

4. Applications of starch-based biodegradable polymers

4.1. In food industry

Food packaging and edible films are two major applications of the starch-based biodegradable polymers in food industry.

The requirements for food packaging include reducing the food losses, keeping food fresh, enhancing organoleptic characteristics of food such as appearance, odor, and flavor, and providing food safety [60]. Traditional food packaging materials such as LDPE have the problem of environmental pollution and disposal problems [61]. The starch-based biodegradable polymers can be a possible alternative for food packaging to overcome these disadvantages and keep the advantages of traditional packaging materials. However, the components in the conventional starch-based polymer packaging materials are not completely inert. The migration of substances into the food possibly happens, and the component that migrates into food may cause harm for the human body. In view of this, new starch-based packaging materials are being developed. For instance, a starch/clay nanocomposite food packaging material is developed, which can offer better mechanical property and lower migration of polymer and additives [62].

Starch-based edible films are odorless, tasteless, colorless, non-toxic, and biodegradable. They display very low permeability to oxygen at low relative humidity [63] and are proposed for food product protection to improve quality and shelf life without impairing consumer acceptability [64].

In addition, starch can be transformed into a foamed material by using water steam to replace the polystyrene foam as packaging material. It can be pressed into trays or disposable dishes, which are able to dissolve in water and leave a non-toxic solution, then can be consumed by microbic environment [65].

Evidently, the starch-based biodegradable polymers are attractive for food industry and will make great progress in the future.

4.2. In agriculture

Starch-based biodegradable polymers have found three major applications in agriculture: the covering of greenhouse, mulch film and fertilizers con-

trolled release materials [66]. The consumption of agriculture films is abundant. Generally, the disposal methods of tradition films are landfill, recycling or burning. But they are time-consuming, not economic and lead to environmental pollution [67]. On the other hand, the utilization efficiency of fertilizers is the key element of the development of agricultural productions. However, due to surface runoff, leaching and vaporization, the fertilizers escape to environment to cause diseconomy and environmental problems [68, 69].

The development of starch-based biodegradable polymers offers a possibility to overcome the mentioned problems. They can be used as the fertilizers controlled release matrices to release the fertilizers slowly or in controlled way. As a result, the loss of fertilizers and environment pollution can be avoided or reduced [50, 70].

After using, starch-based films can be ploughed into soil and disposed directly. Moreover, no toxic residues formed after the degradation of starch-based biodegradable polymers [71, 72]. Thus, the development of starch-based materials for agriculture applications is being continued. For example, to enhance the mechanical properties and solvent or gas resistance, starch-based biodegradable materials are mixed with some nano-grade additives such as TiO_2, layered silicate and MMT to form bionanocomposites [73–75].

4.3. In medical field

Starch-based biodegradeable polymers have some advantages to be medical polymer materials [76–81]:

a) good biocompatibility
b) biodegradable and its degradation products are non-toxic
c) proper mechanical properties
d) degradation as requirement

Starch-based biodegradeable polymers have been widely investigated in bone tissue engineering. Starch-based biodegradable bone cements can provide immediate structural support and degrade from the site of application. Moreover, they can be combined with bioactive particles, which allow new bone growth to be induced in both the interface of cement-bone and the volume left by polymer degradation [82]. In addition, starch-based biodegradeable polymer can also be used as bone tissue engineering scaffold [83].

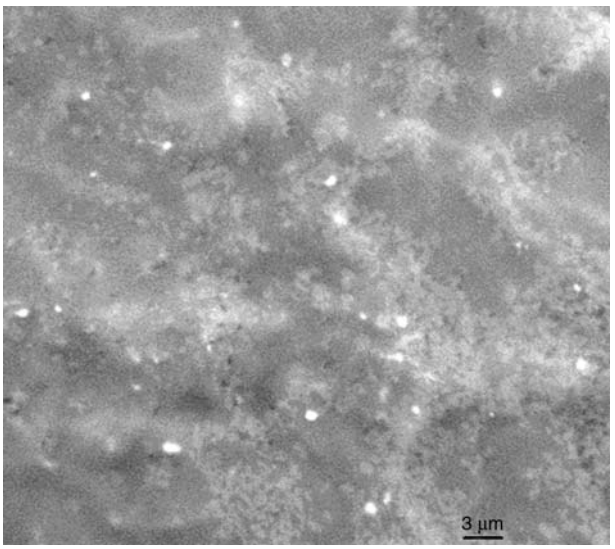

Figure 2. SEM photograph of strach-g-PVA/HA hydrogel (scale bar 3 μm)

Starch-based biodegradable polymers, in the form of microsphere or hydrogel, are suitable for drug delivery [84, 85]. There is no need for surgical removal of the device after drug depletion.

The unique properties, such as hydrophilicity, permeability, biocompatibility, and to some extent similar to soft biological systems, of starch-based hydrogels make them useful for various biomedical applications [86]. The 3D structure of starch-based hydrogels enable them absorb and reserve a plenty of water and keep good enough mechanical property at the same time. Starch-based hydrogels have received growing interest for biomedical applications. In our lab, physically cross-linked starch-g-PVA and starch-g-PVA/hydroxyapatite hydrogel are obtained via repeated freezing/thawing circles, and hydroxyapatite (HA) can be well dispersed in such a matrix (Figure 2) [55, 87]. The water content in the fresh starch-g-PVA/HA hydrogel is comparable to that of PVA/HA hydrogel, and the dried starch-g-PVA/HA films can re-adsorb water soon and reach swelling equilibrium within 12 minutes.

5. Conclusions

Starch is renewable from carbon dioxide, water and sunshine. It is biodegradable, cheap and to be physical or chemical modified easily. This means someday it is unnecessary to rely on petroleum to

prepare polymers, people may 'plant' polymers of suitable performances from the earth, and the environmental problems will be no longer as severe as today. At present and in the near future, different physical and chemical approaches are effective strategies to develop starch-based completely biodegradable polymers of appropriate biocompatibility, degradation rate and physical properties for various applications.

References

[1] Vert M., Santos I. D., Ponsart S., Alauzet N., Morgat J-L., Coudance J., Garreau H.: Degradable polymers in a living environment: Where do you end up? Polymer International, **51**, 840–844 (2002).
DOI: 10.1002/pi.903

[2] Nair L. S., Laurencin C. T.: Biodegradable polymers as biomaterials. Progress in Polymer Science, **32**, 762–798 (2007).
DOI: 10.1016/j.progpolymsci.2007.05.017

[3] Chiellini E., Solaro R.: Biodegradable polymeric materials. Advanced Materials, **4**, 305–313 (1996).
DOI: 10.1002/adma.19960080406

[4] Teramoto N., Motoyama T., Yosomiya R., Shibata M.: Synthesis, thermal properties, and biodegradability of propyl-etherified starch. European Polymer Journal, **39**, 255–261 (2003).
DOI: 10.1016/S0014-3057(02)00199-4

[5] Araújo M. A., Cunha A., Mota M.: Enzymatic degradation of starch-based thermoplastic compounds used in protheses: Identification of the degradation products in solution. Biomaterials, **25**, 2687–2693 (2004).
DOI: 10.1016/j.biomaterials.2003.09.093

[6] Zhang J-F., Sun X. Z.: Mechanical properties of PLA/starch composites compatibilized by maleic anhydride. Biomacromolecules, **5**, 1446–1451 (2004).
DOI: 10.1021/bm0400022

[7] Griffin G. J. L.: Starch polymer blends. Polymer Degradation and Stability, **45**, 241–247 (1994).
DOI: 10.1016/0141-3910(94)90141-4

[8] Pareta R., Edirisinghe M. J.: A novel method for the preparation of starch films and coatings. Carbohydrate Polymer, **63**, 425–431 (2006).
DOI: 10.1016/j.carbpol.2005.09.018

[9] Park J. S., Yang J. H., Kim D. H., Lee D. H.: Degradability of expanded starch/PVA blends prepared using calcium carbonate as the expanding inhibitor. Journal of Applied Polymer Science, **93**, 911–919 (2004).
DOI: 10.1002/app.20533

[10] Schwach E., Avérous L.: Starch-based biodegradable blends: Morphology and interface properties. Polymer International, **53**, 2115–2124 (2004).
DOI: 10.1002/pi.1636

[11] Stepto R. F. T.: Understanding the processing of thermoplastic starch. Macromolecular Symposia, **245–246**, 571–577 (2006).
DOI: 10.1002/masy.200651382

[12] Tomasik P., Schilling C. H.: Chemical modification of starch. Advances in Carbohydrate Chemistry and Biochemistry, **59**, 175–403 (2004).
DOI: 10.1016/S0065-2318(04)59005-4

[13] Ramesh M., Mitchell J. R., Harding S. E.: Amylose content of rice starch. Starch, **51**, 311–313 (1999).
DOI: 10.1002/(SICI)1521-379X(199909)51:8/9<311::AID-STAR311>3.0.CO;2-E

[14] Wallace R. A., King J. L., Sanders G. P.: Biology- The science of life. Goodyear Publishing Company, California (1981).

[15] Stepto R. F. T.: The processing of starch as a thermoplastic. Macromolecular Symposia, **201**, 203–212 (2003).
DOI: 10.1002/masy.200351123

[16] Primarini D., Ohta Y.: Some enzyme properties of raw starch digesting amylases from *streptomyces* sp. No. 4. Starch, **52**, 28–32 (2000).
DOI: 10.1002/(SICI)1521-379X(200001)52:1<28::AID-STAR28>3.0.CO;2-J

[17] Choi E-J., Kim C-H., Park J-K.: Synthesis and characterization of starch-*g*-polycaprolactone copolymer. Macromolecules, **32**, 7402–7408 (1999).
DOI: 10.1021/ma981453f

[18] Griffin G. J. L.: Biodegradable synthetic resin sheet material containing starch and a fatty material. U.S. Patent: 4016117, USA (1977).

[19] Bikiaris D., Prinos J., Koutsopoulos K., Vouroutzis N., Pavlidou E., Frangis N., Panayiotou C.: LDPE/plasticized starch blends containing PE-g-MA copolymer as compatibilizer. Polymer Degradation and Stability, **59**, 287–291 (1998).
DOI: 10.1016/S0141-3910(97)00126-2

[20] Mani R., Bhattacharya M.: Properties of injection moulded blends of starch and modified biodegradable polyesters. European Polymer Journal, **37**, 515–526 (2001).
DOI: 10.1016/S0014-3057(00)00155-5

[21] Ratto J. A., Stenhouse P. J., Auerbach M., Mitchell J., Farrell R.: Processing, performance and biodegradability of a thermoplastic aliphatic polyester/starch system. Polymer, **40**, 6777–6788 (1999).
DOI: 10.1016/S0032-3861(99)00014-2

[22] Jun C. L.: Reactive blending of biodegradable polymers: PLA and starch. Journal of Polymers and the Environment, **8**, 33–37 (2000).
DOI: 10.1023/A:1010172112118

[23] Wang N., Yu J. G., Chang P. R., Ma X.: Influence of formamide and water on the properties of thermoplastic starch/poly(lactic acid) blends. Carbohydrate Polymers, **71**, 109–118 (2008).
DOI: 10.1016/j.carbpol.2007.05.025

[24] Wang N., Yu J. G., Ma X. F.: Preparation and characterization of compatible thermoplastic dry starch/poly(lactic acid). Polymer Composites, **29**, 551–559 (2008).
DOI: 10.1002/pc.20399

[25] Park J. W., Im S. S., Kim S. H., Kim Y. H.: Biodegradable polymer blends of poly(L-lactic acid) and gelatinized starch. Polymer Engineer and Science, **40**, 2539–2550 (2000).
DOI: 10.1002/pen.11384

[26] Martin O., Avérous L.: Poly(lactic acid): Plasticization and properties of biodegradable multiphase systems. Polymer, **42**, 6209–6219 (2001).
DOI: 10.1016/S0032-3861(01)00086-6

[27] Scott G., Gilead D.: Degradable polymers: Principles and applications. Chapman and Hall, London (1995).

[28] Pitt C. G., Gratzl M. M., Jeffcoat A. R., Zweidinger R. A., Schindler A.: Sustained drug delivery systems II: Factors affecting release rates from poly(ε-caprolactone) and related biodegradable polyesters. Journal of Pharmaceutical Sciences, **68**, 1534–1538 (1979).
DOI: 10.1002/jps.2600681219

[29] Li S. M., Espartero J. L., Foch P., Vert M.: Structural characterization and hydrolytic degradation of Zn metal initiated copolymer of L-lactide and ε-caprolactone. Journal of Biomaterials Science, Polymer Edition, **8**, 165–187 (1997).
DOI: 10.1163/156856296X00237

[30] Vikman M., Hulleman S. H. D., van der Zee M., Myllärinen P., Feil H.: Morphology and enzymatic degradation of thermoplastic starch-polycaprolactone blends. Journal Applied Polymer Science, **74**, 2594–2604 (1999).
DOI: 10.1002/(SICI)1097-4628(19991209)74:11<2594::AID-APP5>3.0.CO;2-R

[31] Dubois P., Krishnan M., Narayan R.: Aliphatic polyester grafted starch-like polysaccharides by ring-opening polymerization. Polymer, **40**, 3091–3100 (1999).
DOI: 10.1016/S0032-3861(98)00110-4

[32] Averous L., Moro L., Dole P., Fringant C.: Properties of thermoplastic blends: Starch-polycaprolactone. Polymer, **41**, 4157–4167 (2000).
DOI: 10.1016/S0032-3861(99)00636-9

[33] Singh R. P., Pandey J. K., Rutot D., Degée Ph., Dubois Ph.: Biodegradation of poly(ε-caprolactone)/starch blends and composites in composting and culture environments: The effect of compatibilization on the inherent biodegradability of the host polymer. Carbohydrate Research, **338**, 1759–1769 (2003).
DOI: 10.1016/S0008-6215(03)00236-2

[34] di Franco C. R., Cyras V. P., Busalmen J. P., Ruseckaite R. A., Vázquez A.: Degradation of polycaprolactone/starch blends and composites with sisal fibre. Polymer Degradation and Stability, **86**, 95–103 (2004).
DOI: 10.1016/j.polymdegradstab.2004.02.009

[35] Vertuccio L., Gorrasi G., Sorrentino A., Vittoria V.: Nano clay reinforced PCL/starch blends obtained by high energy ball milling. Carbohydrate Polymers, **75**, 172–179 (2009).
DOI: 10.1016/j.carbpol.2008.07.020

[36] Chiellini E., Corti A., D'Antone S., Solaro R.: Biodegradation of poly(vinyl alcohol) based materials. Progress in Polymer Science, **28**, 963–1014 (2003).
DOI: 10.1016/S0079-6700(02)00149-1

[37] Tudorachi N., Cascaval C. N., Rusu M., Pruteanu M.: Testing of polyvinyl alcohol and starch mixtures as biodegradable polymeric materials. Polymer Testing, **19**, 785–799 (2000).
DOI: 10.1016/S0142-9418(99)00049-5

[38] Lawton J. W.: Effect of starch type on the properties of starch containing films. Carbohydrate Polymers, **29**, 203–208 (1996).
DOI: 10.1016/0144-8617(96)00028-8

[39] Haschke H., Tomka I., Keilbach A.: Systematic investigations on the biological degradability of packing material III. New polyvinylalcohol-starch-acetal films (in German). Monatshefte für Chemie/ Chemical Monthly, **12**, 487–507 (1998).
DOI: 10.1007/PL00000106

[40] Ke T., Sun X. S.: Starch, poly(lactic acid), and poly(vinyl alcohol) blends. Journal of Polymers and the Environment, **11**, 7–14 (2003).
DOI: 10.1023/A:1023875227450

[41] Zhai M. L., Zhao L., Yoshii F., Kume T.: Study on antibacterial starch/chitosan blend film formed under the action of irradiation. Carbohydrate Polymer, **57**, 83–88 (2004).
DOI: 10.1016/j.carbpol.2004.04.003

[42] Bourtoom T., Chinnan M. S.: Preparation and properties of rice starch-chitosan blend biodegradable film. LWT-Food Science and Technology, **41**, 1633–1641 (2008).
DOI: 10.1016/j.lwt.2007.10.014

[43] Psomiadou E., Arvanitoyannis I., Yamamoto N.: Edible films made from natural resources; Microcrystalline cellulose (MCC), methylcellulose (MC) and corn starch and polyols-Part 2. Carbohydrate Polymer, **31**, 193–204 (1996).
DOI: 10.1016/S0144-8617(96)00077-X

[44] Suvorova A. I., Tyukova I. S., Trufanova E. I.: Biodegradable starch-based polymeric materials. Russian Chemical Reviews, **69**, 451–459 (2000).
DOI: 10.1070/RC2000v069n05ABEH000505

[45] Cao X., Chen Y., Chang P. R., Muir A. D., Falk G.: Starch-based nanocomposites reinforced with flax cellulose nanocrystals. Express Polymer Letters, **2**, 502–510 (2008).
DOI: 10.3144/expresspolymlett.2008.60

[46] Bao J. S., Xing J., Phillips D. L., Corke H.: Physical properties of octenyl succinic anhydride modified rice, wheat, and potato starches. Journal of Agricultural and Food Chemistry, **51**, 2283–2287 (2003).
DOI: 10.1021/jf020371u

[47] Kiatkamjornwong S., Mongkolsawat K., Sonsuk M.: Synthesis and property characterization of cassava starch grafted poly[acrylamide-*co*-(maleic acid)] superabsorbent via γ-irradiation. Polymer, **43**, 3915–3924 (2002).
DOI: 10.1016/S0032-3861(02)00224-0

[48] Chen L., Qiu X. Y., Xie Z. G., Hong Z. K., Sun J. R., Chen X. S., Jing X. B.: Poly(L-lactide)/starch blends compatibilized with poly(L-lactide)-g-starch copolymer. Carbohydrate Polymers, **65**, 75–80 (2006).
DOI: 10.1016/j.carbpol.2005.12.029

[49] Choi E-J., Kim C-H., Park J-K.: Structure-property relationship in PCL/starch blend compatibilized with starch-g-PCL copolymer. Journal of Polymer Science Part B: Polymer Physics, **37**, 2430–2438 (1999).
DOI: 10.1002/(SICI)1099-0488(19990901)37:17<2430::AID-POLB14>3.0.CO;2-4

[50] Chen L., Xie Z. G., Zhuang X. L., Chen X. S., Jing X. B.: Controlled release of urea encapsulated by starch-g-poly(L-lactide). Carbohydrate Polymers, **72**, 342–348 (2008).
DOI: 10.1016/j.carbpol.2007.09.003

[51] Xu Q., Kennedy J. F., Liu L. J.: An ionic liquid as reaction media in the ring opening graft polymerization of ε-caprolactone onto starch granules. Carbohydrate Polymers, **72**, 113–121 (2008).
DOI: 10.1016/j.carbpol.2007.07.031

[52] Fanta G. F., Burr R. C., Doane W. M., Russell C. R.: Graft polymerization of vinyl acetate onto starch. Saponification to starch-g-poly(vinyl alcohol). Journal of Applied Polymer Science, **23**, 229–240 (1979).
DOI: 10.1002/app.1979.070230121

[53] Simi C. K., Abraham T. E.: Hydrophobic grafted and crosslinked starch nanoparticles for drug delivery. Bioprocess and Biosystems Engineering, **30**, 173–180 (2007).
DOI: 10.1007/s00449-007-0112-5

[54] Samaha S. H., Nasr H. E., Hebeish A.: Synthesis and characterization of starch-poly(vinyl acetate) graft copolymer and their saponified form. Journal of Polymer Research, **12**, 343–353 (2005).
DOI: 10.1007/s10965-004-7937-2

[55] Xiao C. M., Yang M. L.: Controlled preparation of physical cross-linked starch-g-PVA hydrogel. Carbohydrate Polymer, **64**, 37–40 (2006).
DOI: 10.1016/j.carbpol.2005.10.020

[56] Zhu Z. F., Zhuo R. X.: Slow release behavior of starch-g-poly(vinyl alcohol) matrix for 2,4,5-trichlorophenoxyacetic acid herbicide. European Polymer Journal, **37**, 1913–1919 (2001).
DOI: 10.1016/S0014-3057(01)00055-6

[57] Grote C., Lazik W., Heinze T.: Tartaric acid starch ether: A novel biopolymer-based polyelectrolyte. Macromolecular Rapid Communications, **24**, 927–931 (2003).
DOI: 10.1002/marc.200300042

[58] Xiao C. M., Ye J.: Preparation of the carboxylic derivates of starch with maleic anhydride. Chinese Journal of Applied Chemistry, **22**, 643–646 (2005).

[59] Xiao C. M., Fang F.: Ionic self-assembly and characterization of a polysaccharide-based polyelectrolyte complex of maleic starch half-ester acid with chitosan. Journal of Applied Polymer Science, **112**, 2255–2260 (2009).
DOI: 10.1002/app.29763

[60] Zhao R. X., Torley P., Halley P. J.: Emerging biodegradable materials: Starch- and protein-based bio-nanocomposites. Journal of Material Science, **43**, 3058–3071 (2008).
DOI: 10.1007/s10853-007-2434-8

[61] Ozdemir M., Floros J. D.: Active food packaging technologies. Critical Reviews in Food Science and Nutrition, **44**, 185–193 (2004).
DOI: 10.1080/10408690490441578

[62] Avella M., de Vlieger J. J., Errico M. E., Fischer S., Vacca P., Volpe M. G.: Biodegradable starch/clay nanocomposite films for food packaging applications. Food Chemistry, **93**, 467–474 (2005).
DOI: 10.1016/j.foodchem.2004.10.024

[63] The D. P., Debeaufort F., Voilley A., Luu D.: Biopolymer interactions affect the functional properties of edible films based on agar, cassava starch and arabinoxylan blends. Journal of Food Engineering, **90**, 548–558 (2009).
DOI: 10.1016/j.jfoodeng.2008.07.023

[64] Flores S., Haedo A. S., Campos C., Gerschenson L.: Antimicrobial performance of potassium sorbate supported in tapioca starch edible films. European Food Research Technology, **225**, 375–384 (2007).
DOI: 10.1007/s00217-006-0427-5

[65] Siracusa V., Rocculi P., Romani S., Rosa M. D.: Biodegradable polymers for food packaging: A review. Trends in Food Science and Technology, **19**, 634–643 (2008).
DOI: 10.1016/j.tifs.2008.07.003

[66] Dilara P. A., Briassoulis D.: Degradation and stabilization of low-density polyethylene films used as greenhouse covering materials. Journal of Agricultural Engineering Research, **76**, 309–321 (2000).
DOI: 10.1006/jaer.1999.0513

[67] Bohlmann G., Toki G.: Chemical economics handbook. SRI International, Menlo Park (2004).

[68] Dave A. M., Mehta M. H., Aminabhavi T. M., Kulkarni A. R., Soppimath K. S.: A review on controlled release of nitrogen fertilizers through polymeric membrane devices. Polymer-Plastics Technology and Engineering, **38**, 675–711 (1999).
DOI: 10.1080/03602559909351607

[69] Guo M., Liu M., Zhan F., Wu L.: Preparation and properties of a slow-release membrane-encapsulated urea fertilizer with superabsorbent and moisture preservation. Industrial and Engineering Chemistry Research, **44**, 4206–4211 (2005).
DOI: 10.1021/ie0489406

[70] Kumbar S. G., Kulkarni A. R., Dave A. M., Aminabha T. M.: Encapsulation efficiency and release kinetics of solid and liquid pesticides through urea formaldehyde crosslinked starch, guar gum, and starch + guar gum matrices. Journal of Applied Polymer Science, **82**, 2863–2866 (2001).
DOI: 10.1002/app.2141

[71] Malinconico M., Immirzi B., Massenti S., La Mantia F. P., Mormile P., Petti L.: Blends of polyvinylalcohol and functionalised polycaprolactone. A study on the melt extrusion and post-cure of films suitable for protected cultivation. Journal of Materials Science, **37**, 4973–4978 (2002).
DOI: 10.1023/A:1021058810774

[72] Scott G.: 'Green' polymers. Polymer Degradation and Stability, **68**, 1–7 (2000).
DOI: 10.1016/S0141-3910(99)00182-2

[73] Scarascia-Mugnozza G., Schettini E., Vox G., Malinconico M., Immirzi B., Pagliara S.: Mechanical properties decay and morphological behaviour of biodegradable films for agricultural mulching in real scale experiment. Polymer Degradation and Stability, **91**, 2801–2808 (2006).
DOI: 10.1016/j.polymdegradstab.2006.02.017

[74] Wang Y-Z., Yang K-K., Wang X-L., Zhou Q., Zheng C-Y., Chen Z-F.: Agricultural application and environmental degradation of photo-biodegradable polyethylene mulching films. Journal of Polymers and the Environment, **12**, 7–10 (2004).
DOI: 10.1023/B:JOOE.0000003122.71316.8e

[75] Yew S. P., Tang H. Y., Sudesh K.: Photocatalytic activity and biodegradation of polyhydroxybutyrate films containing titanium dioxide. Polymer Degradation and Stability, **91**, 1800–1807 (2006).
DOI: 10.1016/j.polymdegradstab.2005.11.011

[76] Marques A. P., Reis R. L., Hunt J. A.: The biocompatibility of novel starch-based polymers and composites: In vitro studies. Biomaterials, **23**, 1471–1478 (2002).
DOI: 10.1016/S0142-9612(01)00272-1

[77] Mendes S. C., Reis R. L., Bovell Y. P., Cunha A. M., van Blitterswijk C. A., de Bruijn J. D.: Biocompatibility testing of novel starch-based materials with potential application in orthopaedic surgery: A preliminary study. Biomaterials, **22**, 2057–2064 (2001).
DOI: 10.1016/S0142-9612(00)00395-1

[78] Azevedo H. S., Gama F. M., Reis R. L.: In vitro assessment of the enzymatic degradation of several starch based biomaterials. Biomacromolecules, **4**, 1703–1712 (2003).
DOI: 10.1021/bm0300397

[79] Defaye J., Wong E.: Structural studies of gum arabic, the exudate polysaccharide from acacia senegal. Carbohydrate Research, **150**, 221–231 (1986).
DOI: 10.1016/0008-6215(86)80018-0

[80] Reddy S. M., Sinha V. R., Reddy D. S.: Novel oral colon-specific drug delivery systems for pharmacotherapy of peptides and nonpeptide drugs. Drugs of Today, **35**, 537–580 (1999).

[81] Sinha V. R., Kumria R.: Polysaccharides in colon-specific drug delivery. International Journal of Pharmaceutics, **224**, 19–38 (2001).
DOI: 10.1016/S0378-5173(01)00720-7

[82] Boesel L. F., Mano J. F., Reis R. L.: Optimization of the formulation and mechanical properties of starch based partially degradable bone cements. Journal of Materials Science: Materials in Medicine, **15**, 73–83 (2004).
DOI: 10.1023/B:JMSM.0000010100.07715.eb

[83] Gomes M. E., Sikavitsas V. I., Behravesh E., Reis R. L., Mikos A. G.: Effect of flow perfusion on the osteogenic differentiation of bone marrow stromal cells cultured on starch-based three-dimensional scaffolds. Journal of Biomedical Materials Research Part A, **67**, 87–95 (2003).
DOI: 10.1002/jbm.a.10075

[84] Balmayor E. R., Tuzlakoglu K., Marques A. P., Azevedo H. S., Reis R. L.: A novel enzymatically-mediated drug delivery carrier for bone tissue engineering applications: Combining biodegradable starch-based microparticles and differentiation agents. Journal of Material Science: Materials in Medicine, **19**, 1617–1623 (2008).
DOI: 10.1007/s10856-008-3378-5

[85] Reis A. V., Guilherme M. R., Moia T. A., Mattoso L. H. C., Muniz E. C., Tambourgi E. B.: Synthesis and characterization of a starch-modified hydrogel as potential carrier for drug delivery system. Journal of Polymer Science Part A: Polymer Chemistry, **46**, 2567–2574 (2008).
DOI: 10.1002/pola.22588

[86] Peppas N. A., Bures P., Leobandung W., Ichikawa H.: Hydrogels in pharmaceutical formulations. European Journal of Pharmaceutics and Biopharmaceutics, **50**, 27–46 (2000).
DOI: 10.1016/S0939-6411(00)00090-4

[87] Gao Y. K., Xiao C. M.: Preparation and characterization of starch-g-PVA/nano-hydroxyapatite complex hydrogel. Journal of Wuhan University of Technology-Materials Science Edition, **20**, 58–59 (2005).

eXPRESS Polymer Letters Vol.3, No.6 (2009) 376–384
Available online at www.expresspolymlett.com
DOI: 10.3144/expresspolymlett.2009.47

Synergistic effects of zinc borate and aluminium trihydroxide on flammability behaviour of aerospace epoxy system

C. Formicola[1,3], A. De Fenzo[1,3], M. Zarrelli[1,3], A. Frache[2] , M. Giordano[1,3], G. Camino[2]*

[1]IMCB – Institute of Composite and Biomedical Materials, CNR – Research National Council, P E. Fermi 1, Portici 80055, Italy
[2]Department of Materials Science and Chemical Engineering Politecnico di Torino, Via Teresa Michel 5,15100 Alessandria, Italy
[3]IMAST – Technological District on Polymeric and Composite Materials Engineering, P E. Fermi 1, Portici 80055, Italy

Received 5 March 2009; accepted in revised form 3 April 2009

Abstract. The flame retardancy of mono-component epoxy resin (RTM6), widely used for aerospace composites, treated with zinc borate (ZB), aluminium trihydroxide (ATH) and their mixtures at different concentrations have been investigated by morphological and thermal characterization. Cone calorimeter data reveal that combustion behaviour, heat release rate peak (PHRR) and heat release rate average (HRR Average) of RTM6 resin decrease substantially when synergistic effects of zinc borate and aluminium trihydroxide intervene. Thermogravimetric (TGA) results and analysis of the residue show that addition higher than 20% w/w of ZB, ATH, and their mixture greatly promotes RTM6 char formation acting as a barrier layer for the fire development. Depending upon the different used flame additives, SEM micrographs indicate that the morphology of residual char could vary from a compact amalgam-like structure, for the RTM6+ZB system, to a granular structure, characterized by very small particles of degraded resin and additive for the ATH.

Keywords: *thermosetting resins, fire retardancy, zinc borate, aluminium trihydroxide, cone calorimeter*

1. Introduction

Zinc borate is an effective inorganic flame retardant and it possesses characteristic properties of flame retardancy (FR), smoke suppression, promoting charring, etc. [1, 2] particularly important according to new fire standards. Zinc borate is commonly used as multifunctional flame retardant in combination with other halogenated or halogen-free flame retardant systems to boost FR properties [3, 4]. Its efficacy depends upon the type of halogen source (aliphatic versus aromatic) and the used polymer. The zinc borate can generally display synergistic effects with antimony oxide in fire retardancy. In the presence of aluminium trihydroxide (ATH) or magnesium hydroxide ($Mg(OH)_2$), this synergy can be augmented significantly [5]. Previous studies [6–11] have demonstrated that there are major advantages in using a combination of zinc borates with other flame retardants in several kinds of polymers (EVA, PVC, Polyamides, etc…). Furthermore, various authors [13–20] analyzed the fire and smoke behaviours of zinc borate and its synergist effect only in thermoplastic systems or in thermosetting bi-component matrices.

In this work, the synergistic effect of zinc borate and aluminium trihydroxide on the flame retardancy, smoke suppression, and thermal degradation behaviour of a monocomponent epoxy resin

*Corresponding author, e-mail: cristina.formicola@imcb.cnr.it

(RTM6) is investigated. The considered epoxy system is widely used in primary and secondary composite structures within the aerospace sector (Arianne 5 and Airbus A380 [12]) for which fire behaviour represents an important feature upon the final application. The fire retardancy of different samples, characterized by various concentrations of each additive and their combinations is exploited by cone calorimeter, TG-DTG and SEM analysis.

2. Experimental section

2.1. Materials and processing

The epoxy resin used is a commercially available pre-hardened epoxy-amine system labelled RTM6. The system was provided by Hexcel Composites (Duxford, UK). The ultra fine zinc borate ($2ZnO\ 3B_2O_3\ 3.5H_2O$) and the aluminium trihydroxide ($Al(OH)_3$) were supplied respectively by Joseph Storey & Co. (UK) and by Dadco (UK). The composites were prepared by mixing the epoxy resin with ZB and ATH both separately and in combination. For the separate mixtures 5, 10, 20, 30 and 40% w/w were used while for the combination they were mixed at 1:1 ratio in mass at 10, 20, 30 and 40% w/w. The mixing was performed by using a Heidolph RZR mechanical stirring equipment. The samples were prepared by mixing RTM6 with ZB and ATH for 10 min at 1050 rpm and 10 min at 2000 rpm. Obtained mixture was then degassed for 30 min at 90°C under vacuum to eliminate entrapped air and absorbed humidity. The final liquid mixture was then poured in aluminium mould and cured by a two stage temperature profile (160 and 180°C respectively for 90 and 120 min) according to the curing schedule sheet of the neat epoxy resin. Preliminary TGA scans on neat additives were also performed to evaluate their maximum degradation temperatures. It was found that zinc borate and aluminium trihydroxide degraded respectively at 436 and 299°C well below the set curing conditions.

2.2. Methods

Cone calorimeter tests were performed using a Fire Testing Technology Ldt. equipment according to the ASTM E1354-04 procedure. Samples, with nominal dimensions of 100×100×7 mm^3, were tested horizontally under an incident flux of 50 kW/m^2. This level was chosen as it corresponds to the evolved heat during a fire. Thermogravimetric analysis was carried out using a TGA 2950 by TA Instruments. All measurements were conducted under nitrogen flow, with a sample weight of about 7±0.5 mg; for each test the heating rate was 10°C/min from ambient to 800°C. The precision on the temperature measurements during each scan, according to the calibration procedure was ± 0.5°C in the range 30–400°C and ±1°C in the range 400–800°C. SEM and optical micrographs of additive powder, composites and residuals were taken respectively by an 1450VP LEO SEM microscopy and an optical Olimpus BX51 Instruments.

3. Results and discussion

3.1. SEM and optical microscopy

Multiple locations on different samples were observing by optical and SEM microscopy to verify the level of dispersion. Figure 1 reports a 10X optical micrograph of 20% w/w zinc borate and epoxy system, showing a uniform distribution through the matrix. At all considered concentrations either for ZB and ATH, the powder is well dispersed into the epoxy matrix maintaining also its original grain size as also confirmed by Figures 2a and 2b, where SEM micrographs, respectively of ZB as-received and RTM6/ZB mixing at 20% w/w are reported. An appreciable uniformity of filler within the hosting matrix where observed on all loaded samples for both ZB and ATH filler.

In order to study the synergistic effects of zinc borate with aluminium trihydroxide, samples of composite of RTM6 and ZB/ATH, dispersed at

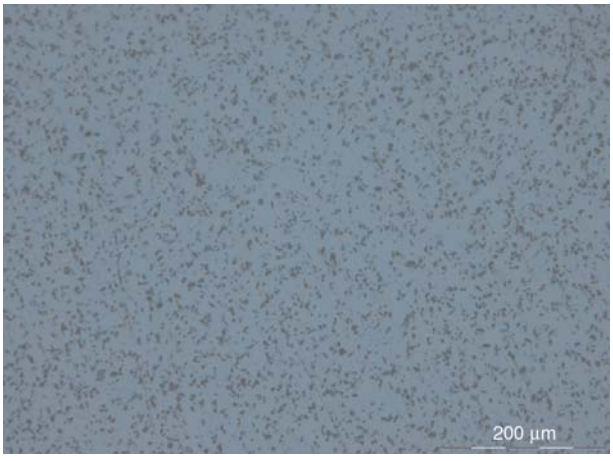

Figure 1. Optical microscopy of zinc borate dispersed into the epoxy resin (200 µm)

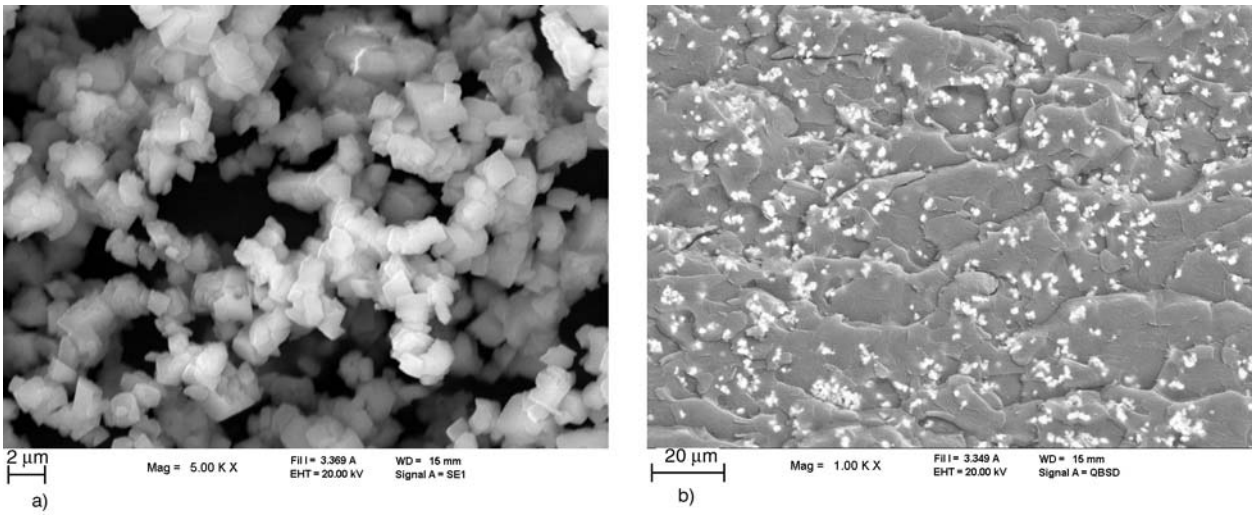

Figure 2. Scanning electron micrograph of zinc borate powder (a) and scanning electron micrograph of composites of RTM6 and ZB 20% w/w (b)

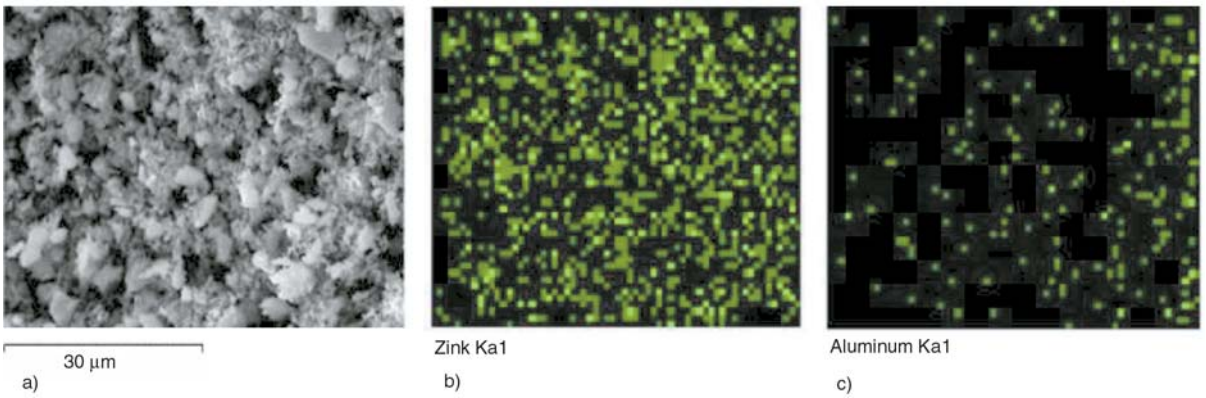

Figure 3. Mapping of ZB/ATH sample dispersed into the epoxy resin

total concentration of 20% w/w, were mapped by SEM. The presence of ZB and ATH, consistently found together within the same area of the sample, lead to the reasonable conclusion that an interaction between the two additives could be assumed (Figure 3). This conclusion is also confirmed by experimental TGA data compared with the corresponding calculated curves as reported in following paragraph.

3.2. Thermogravimetric analysis

Thermogravimetric analysis (TGA) and derivative signal (DTG) represent a quantitative methodology useful to analyze the stability of materials. TGA scans were performed on all composite samples for each concentration. TGA theoretical curves (calculated curves) were then computed and compared to experimentally obtained thermographs to further understand the synergist effect of ZB and ATH on the degradation behaviour of the RTM6 epoxy system.

Analysis of the TGA curves and their DTG signals reveals that onset temperature, which corresponds to the value at 5% of weight loss, are augmented significantly in the case of 30 and 40% w/w content for both mixtures, RTM6/ATH and RTM6/ZB. According to Table 1, in fact, measured values for onset and maximum temperatures fall within the same range, if the error bar is considered; thus highlighting the substantial inefficiency of the filler to act as flame retardant. As expected, it is neces-

Table 1. TGA values of treated RTM6 with ATH and ZB at different concentrations

Sample	T_{onset}	T_{max}	Sample	T_{onset}	T_{max}
RTM6 neat	327±5	389±4			
ATH 5%	332±3	395±3	ZB 5%	342±3	380±2
ATH 10%	325±5	393±3	ZB 10%	348±4	382±4
ATH 20%	321±5	392±4	ZB 20%	352±5	388±3
ATH 30%	360±4	411±2	ZB 30%	368±3	418±5
ATH 40%	368±5	413±3	ZB 40%	379±3	426±4

sary to add a high weight content of filler to induce an active retardant effect to the degradation process of the hosting material.

In the case of ATH, the presence of the additives increases the onset temperature due to the decomposition reaction [$2Al(OH)_3 \rightarrow Al_2O_3 + 3H_2O$] which takes place between 220 and 400°C. ATH decomposition is an endothermic reaction, which, ATH absorbs about 1 kJ/g of heat. The main endothermic peak of the reaction occurs at about 300°C, which means that the reaction is absorbing the most heat at a temperature below the service degradation temperature level of most polymers. Another important aspect of the reaction is the release of water vapour formed from the hydroxyl group bonded with aluminium. This water is released into the flame hindering the combustion process by diluting the concentration of flammable evolving gases and restricting the access of oxygen through the composite surface. An added benefit of the decomposition reaction is that no toxic or corrosive gases are produced unlike some other flame retardant compounds are present. ATH also operates as a heat sink extending the time to reach the polymer decomposition temperature. ATH has a higher heat capacity than most organic resins, enabling it to absorb heat and promoting a 'cooling' effect of the host polymer. It is believed that another mechanism of ATH is the formation of a refractory layer of Al_2O_3 following the decomposition of the ATH. The efficiency of the aluminium oxide layer with the consistency and thickness needed to be an effective thermal barrier is strictly depended upon the ATH content [21]. ZB acts as flame retardant in both condensed and gas phases of the combustion process. At elevated temperatures, this compounds decomposes, releasing crystallization water molecules (about 15% by weight of water in the temperature range of 290–450°C) which dilutes the concentration of H radicals and organic volatiles in the flame, reducing its temperature. After decomposition, the residual borate retained in the decomposed polymer will form a vitreous-like layer that slows the permeation of volatile compounds through the surface and restricts them from entering the gas phase [21].

Analysis of onset temperatures evaluated by TGA scans, lead to the main conclusion that both types of fillers do not enhance significantly the start of degradation process below a specific concentration,

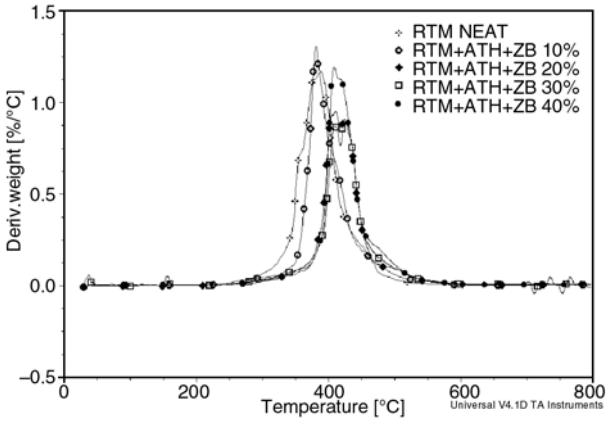

Figure 4. DTG curves of RTM6/ATH/ZB system at different percentage

Table 2. TGA values of treated RTM6 with ZB+ATH at different concentrations

Sample	T_{onset} [°C]	T_{max} [°C]
RTM6 neat	327±5	389±4
RTM6+ZB+ATH (10%wt)	345±4	381±4
RTM6+ZB+ATH (20%wt)	352±4	417±4
RTM6+ZB+ATH (30%wt)	365±3	428±3
RTM6+ZB+ATH (40%wt)	375±5	434±5

as expected. Different observations can be made by analysing the TGA results of RTM6 and a combination amount of ZB and ATH. The synergy between the ZB and ATH was investigated on four different percentages (10, 20, 30 and 40% w/w with 1:1 ratio in mass) and the corresponding DTG curves are reported in Figure 4. Table 2 reports the onset and maximum degradation temperatures for all concentrations considered of ATH/ZB loaded samples according to the thermogravimetry. It can be noticed that small variations are found for both parameters if the filler content is lower than 20% w/w (i.e. 10% w/w of ATH and 10% w/w of ZB); whereas, for higher weight content (i.e. higher than 15% w/w for each filler) appreciable increase of both temperature levels are found. The combination of these two types of flame retardant reduces the overall concentration level needed to achieve a higher flammability resistance; thus, minimising the risk of adverse effects, such as mechanical property degradation and density increase of the hosting materials. The analysis of experimental TGA and DTG curves with a law of mixture based model, hereby referred as calculated curves, could be very useful to proof the synergistic effect of flame retardancy associated with a combined amount respect to the percentage used of stand-

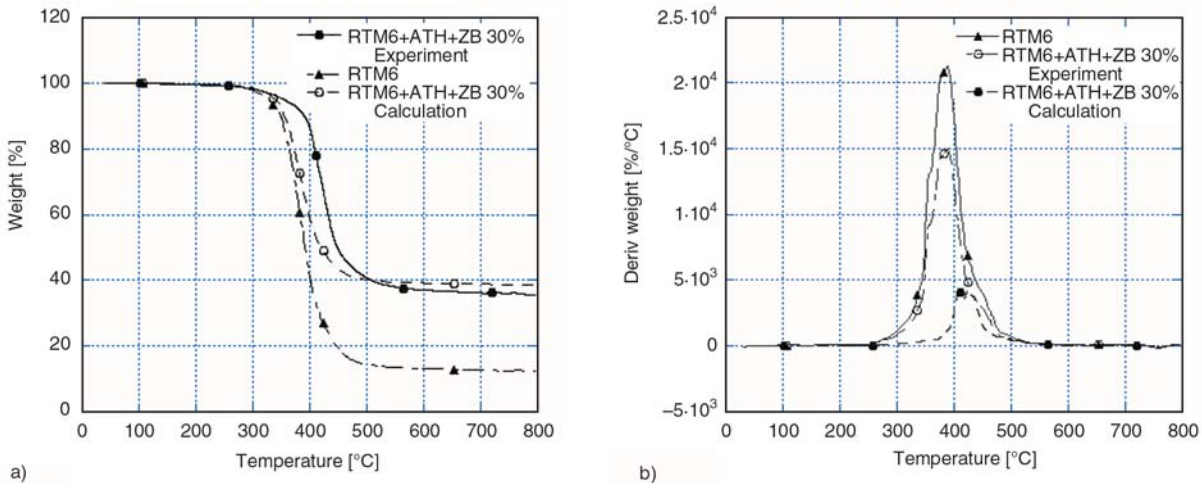

Figure 5. Experimental and calculated TGA (a) and DTG (b) curves for 30 wt%RTM6/ATH/ZB

alone filler. Calculated and experimental TG-DTG curves have been superimposed in Figure 5 for the 30% w/w ZB/ATH amount. Experimental curves are shifted to higher temperatures if compared with their corresponding calculated curves; therefore a superposition effect of flame retardancy due to the presence of each filler is not able to model accurately the experimental results. A synergic mechanism due to the combined amount of fillers can be assumed to occur on the degradation behaviour of the overall loaded system. Similar results were also obtained for all other considered total concentrations, leading to analogous results. The synergistic effect due to the presence of both, ZB and ATH, is quantified by substantial the increase of the onset and maximum degradation temperatures, respectively of 50 and 40°C for the highest total percentage compared with the neat epoxy system.

It can be concluded that the addition of ZB and ATH synergistically retards the degradation behaviour of neat matrix system enhancing the flame retardancy of the overall hosting system at lower concentration respect to the stand alone filler loading.

3.3. Cone calorimeter test

Cone calorimeter represents a small-scale testing configuration which provides important correlating parameters with real fire scenario; data obtained from cone calorimeter can provide plentiful information on fire scenario behaviour of a specific material [22, 23]. Figures 6a and 6b report the HRR curves over three different tests, respectively for the neat epoxy and loaded systems along with their average. The values provided by cone calorimeter are mainly: Time To Ignition (TTI), which corresponds to the period that a combustible material can withstand when exposure to a constant radiant heat flux before igniting and undergoing sustained flaming combustion; Heat Release Rate peak (PHRR) and average (HRR average) are a quantitative

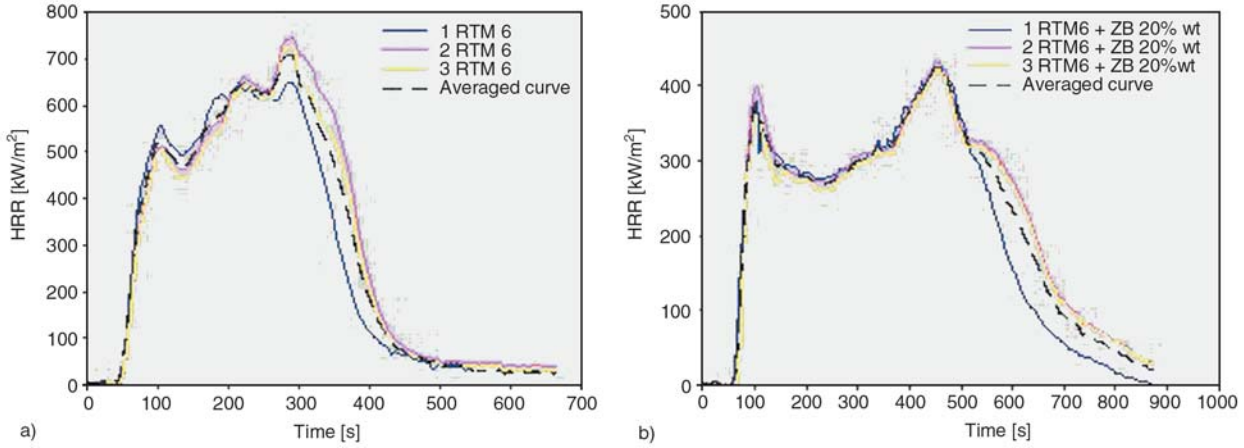

Figure 6. HRR curves for neat epoxy (a) and RTM6 loaded with 20% w/w of zinc borate (b)

Table 3. Main cone calorimeter parameters evaluated for RTM6 epoxy with ZB and ATH at different concentrations

Sample	TTI [s]	ΔTTI [s]	PHRR [kW/m²]	HRR Average [kW/m²]	ΔPHRR [kW/m²]
RTM6	43±2	–	702±3	382±4	–
RTM6+ZB 5%	44±5	5	682±2	354±3	20
RTM6+ZB 10%	48±4	1	523±3	265±2	179
RTM6+ZB 20%	49±3	6	428±2	251±4	274
RTM6+ZB 30%	58±2	14	396±3	193±3	306
RTM6+ZB 40%	63±2	20	315±2	148±2	387
RTM6+ATH 5%	33±6	–10	815±4	413±2	–113
RTM6+ATH 10%	41±3	8	728±4	383±2	–26
RTM6+ATH 20%	52±3	9	510±5	368±3	192
RTM6+ATH 30%	64±2	21	468±5	324±1	234
RTM6+ATH 40%	93±2	50	453±2	193±2	249
RTM6+ZB+ATH 10%	52±2	9	679±3	337±2	23
RTM6+ZB+ATH 20%	52±3	9	468±2	285±3	234
RTM6+ZB+ATH 30%	55±3	12	431±1	249±2	271
RTM6+ZB+ATH 40%	87±2	44	437±4	74±3	265

measures of the amount of thermal energy released by a material per unit area when exposed to a fire radiating at constant heat flux (or temperature).

The cone calorimeter data reported in Table 3 are averaged over three replicate experiments. The HRR value is considered the single most important fire reaction property as it represents the most valuable indicator of the fire hazard for a combustible material.

For the RTM6/ZB compound, data show that the presence of the filler at 5, 10 and 20% w/w does not change substantially neither the time to ignition or the heat release rate peak values. Instead, the presence of zinc borate at higher concentrations (30, 40% w/w) improves flame retardant behaviour of the neat resin system as supported by the recorded values of PHRR and HRR average which increase respectively by 15 and 20 kW/m².

The accentuate peak for the ZB 5% w/w curve, around 300 s, could be attribute to a local instability of the heat flux during the test which lead to a wider cracked area and therefore, a localised combustion growth. In Figure 7a the HRR curves of RTM6/ZB are characterised by an increased time period up to 1200 s in the case of 40% w/w content, with a progressive flatness of the curve height at highest content. Decreasing values for the PHRR and HRR average may be correlated with the decomposition of the filler and the formation of a protective glassy char layer over the surface of sample, during the combustion process (Figure 7b). The consistency of this formed layer, inevitably, reduces oxygen absorption and limits the permeation of volatile compounds through the surface of the fired system.

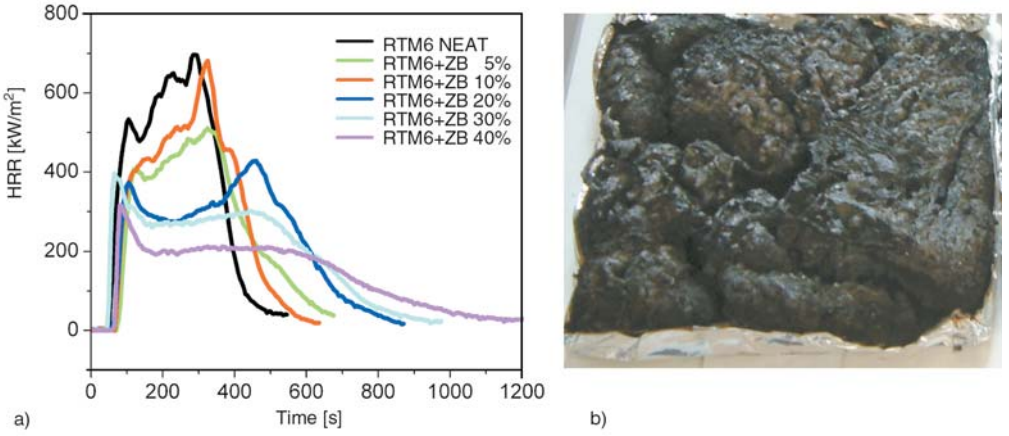

Figure 7. HRR curves of RTM6/ZB at different concentrations (a) and RTM6/ZB at 40% w/w residue (b)

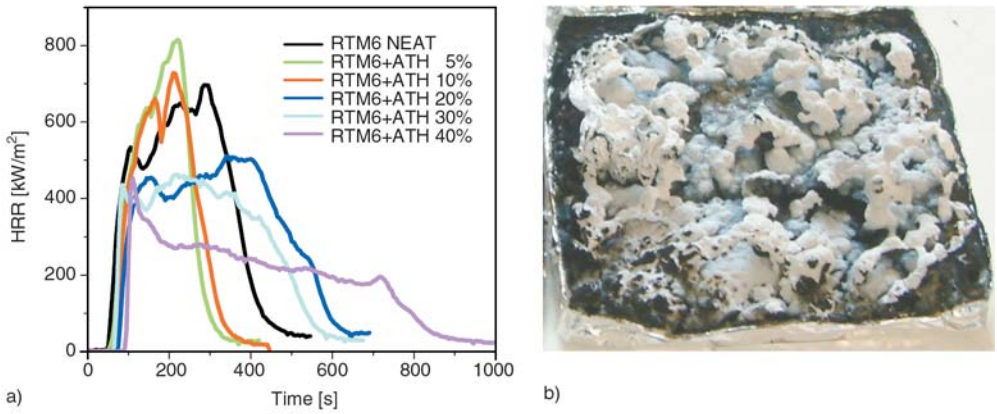

Figure 8. HRR curves of RTM6/ATH at different concentrations (a) and RTM6/ATH at 40% w/w residue (b)

In the case of ATH filler, it was found that the presence of the micro-sized particles has a detrimental effect at lower concentrations compared with the neat epoxy system (Figure 8a). The two curves, in fact, are characterised by a higher peak value and a slight left shifting, probably due to the presence of filler which breaks the continuity of the hosting system providing a more opened morphology of the char for the propagation of the flame. Analysis of cone calorimetry results indicates that the HRR peak of the RTM6/ATH system is reduced from 815 to 510 kW/m^2, respectively for the 5 and 20% w/w and this value is further reduced with rising of filler concentration to 453 kW/m^2 for the maximum content of 40% w/w. The filler effect on HRR averaged values is also very noticeable varying of about 50% for the highest filler content (193 kW/m^2) compared with the unloaded epoxy (382 kW/m^2). For ATH content higher than 20% w/w the material behaviour is affected by the presence of the filler with more evidence: flattening the curve and reducing the averaged HRR. In Figure 8b the image of the residue 40% w/w RTM6/ATH system with the whitish surface characteristic of the aluminium trihydroxide is reported. A visual inspection of the final residual sample reports the presence of the char layer (Figures 7b and 8b) characterised by a different morphology. Analysis of SEM micrographs on residual of system of epoxy resin, zinc borate and aluminium trihydroxide indicates that char topography varies from a compact like-amalgam structure for the RTM6/ZB (Figure 9a) to a granular porous-like structure characterized by very small particles of additive along with some residual carbon from the resin for the ATH mixture (Figure 9b).

Different conclusions can be drawn in the case of ATH and ZB mixture filler content. The synergistic effect of these two additives becomes effective with a weight content of both fillers higher than 10%. In fact, the averaged HHR undergoes a slight drop from 382 kW/m^2 for the epoxy resin to

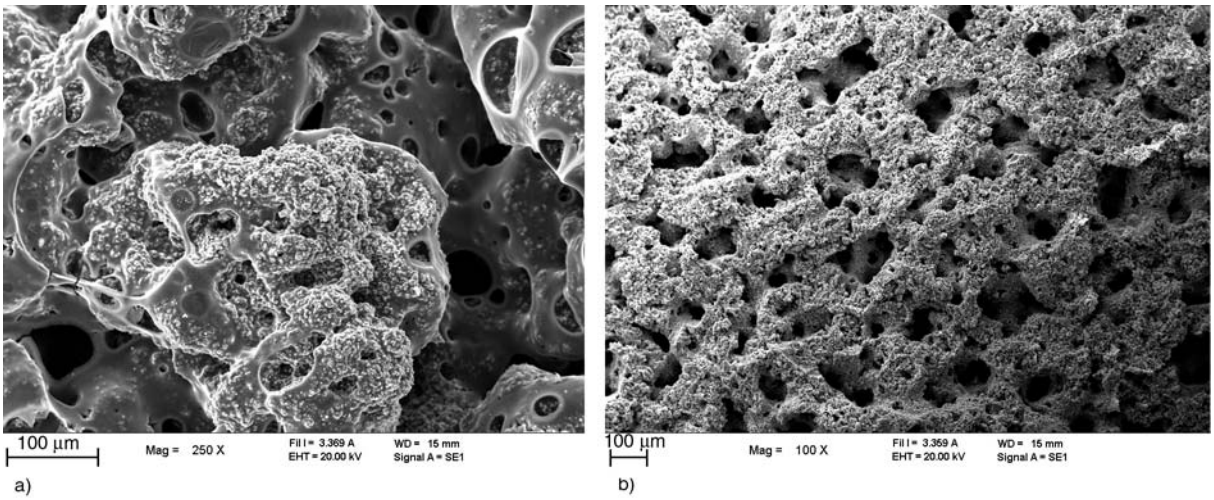

Figure 9. SEM micrographs of residual samples of RTM6/ZB 20 wt% (a)and of RTM6/ATH 20 wt% (b)

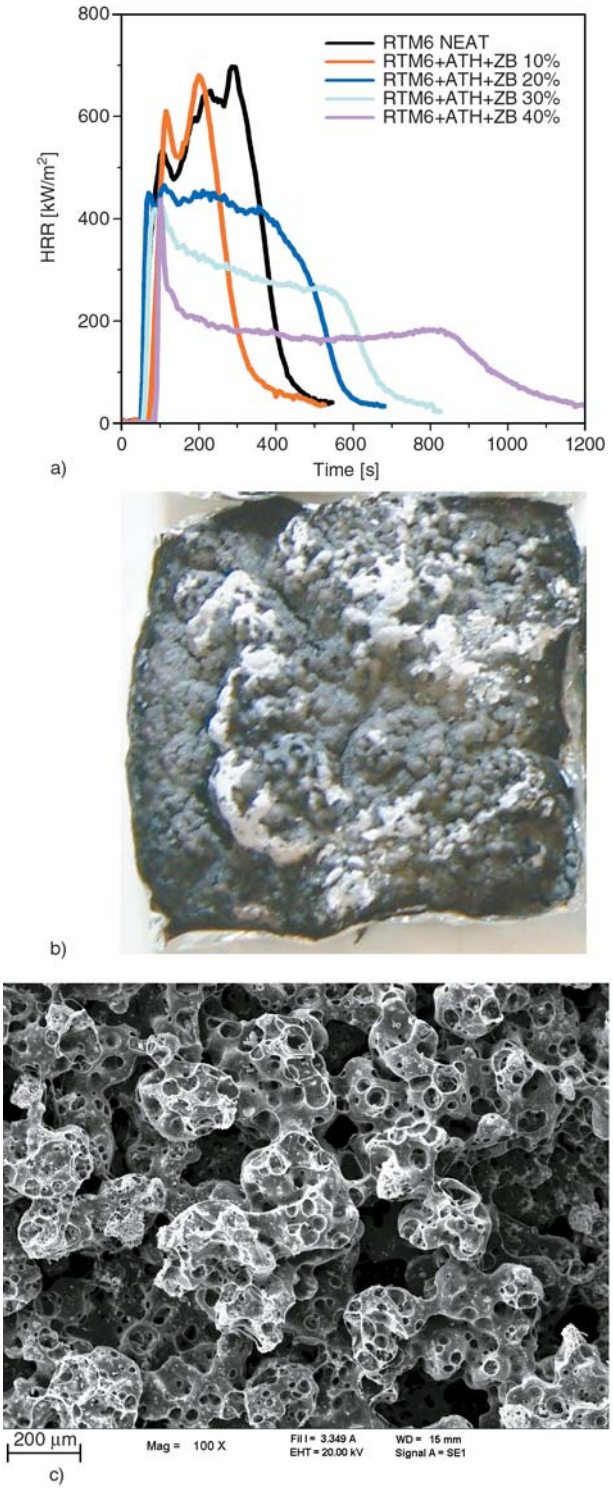

Figure 10. HRR curves of RTM6/ZB/ATH system at different concentrations (a), RTM6/ZB/ATH system residue (b) and SEM of residual samples of RTM6/ZB/ATH system (c)

285 kW/m^2 for system RTM6/ZB/ATH 20% w/w, with a further reduction to 249 and 74 kW/m^2, respectively for the 30 and 40% w/w of RTM6/ZB/ATH (Figure 10a). This indicates that the concentration of the each filler can be lowered in the case of ATH/ZB mixture loading if compared with the corresponding single filler system due to the synergistic effect associated with the presence of both additives. Comparing the ΔTTI and the HRR average values for RTM6/ZB 20% w/w, RTM6/ATH 20% w/w and RTM6/ZB/ATH system at 40% w/w, the filler synergy improves significantly the flame retardancy, respectively from 6 to 9 to 44 s; and from 251 to 368 to 74 kW/m^2. An optical image and an SEM micrograph of residual samples of RTM6/ZB/ATH are reported respectively in Figures 10b and 10c. The char is characterised by an amalgam structure due to ZB filler and a porous whitish morphology typical of the ATH residue is clearly showed by the SEM photo.

4. Conclusions

The synergistic effect of zinc borate and aluminium trihydroxide on flammability behaviour of monocomponent epoxy resin has been studied in this work. Cone calorimeter experiments and results, obtained by thermogravimetric analysis, report clearer evidence that content of zinc borate and aluminium trihydroxide higher that 20% w/w makes the neat resin system resistant to flame. Moreover a combination of the two fillers, at lower specific content, will affect synergistically the flammability behaviour of the neat system minimising the risk of adverse effects of original materials. Characteristic parameters, obtained by cone calorimeter tests, such as PHRR, HRR average and TTI reach higher values, indicating improved fire behaviour. The synergistic effect of zinc borate with aluminium trihydroxide on the RTM6 epoxy resin can be reasonably proved not only comparing the TGA experiential curve with a mixture law based model but also analysing the cone results related with the 20% w/w combined loads. Scanning electron micrographs indicate that the synergist flame retardant effects of these additives results from the excellent quality of char which compromises the ZB and ATH char morphology enduring the oxidation at high temperatures slowing, at same time, the degradation of epoxy resin.

References

[1] Giùdice C. A., Benitez J. C: Zinc borates as flame-retardant pigments in chlorine-containing coatings. Progress in Organic Coatings, **42**, 82–88 (2001).
DOI: 10.1016/S0300-9440(01)00159-X

[2] Nazare S., Kandola B. K., Horrocks A. R.: Smoke, CO, and CO_2 measurements and evaluation using different fire testing techniques for flame retardant unsaturated polyester resin formulations. Journal of Fire Sciences, **26**, 215–242 (2008).
DOI: 10.1177/0734904107087818

[3] Wu Z., Shu W., Hu Y.: Synergist flame retarding effect of ultrafine zinc borate on LDPE/IFR system. Journal of Applied Polymer Science, **103**, 3667–3674 (2007).
DOI: 10.1002/app.25575

[4] Maurer O.: New reactive, halogen-free flame retardant system for epoxy resins. Polymer Degradation and Stability, **88**, 70–73 (2005).
DOI: 10.1016/j.polymdegradstab.2004.01.027

[5] Shen K. K., Kochesfahani S., Jouffret F.: Zinc borates as multifunctional polymer additives. Polymers for Advanced Technology, **19**, 469–474 (2008).
DOI: 10.1002/pat.1119

[6] Bourbigot S., Le Bras M., Leeuwendal R., Shen K. K., Schubert D.: Recent advances in the use of zinc borates in flame retardancy of EVA. Polymer Degradation and Stability, **64**, 419–425 (1999).
DOI: 10.1016/S0141-3910(98)00130-X

[7] Kim S.: Flame retardancy and smoke suppression of magnesium hydroxide filled polyethylene. Journal of Polymer Science Part B: Polymer Physics, **41**, 936–944 (2003).
DOI: 10.1002/polb.10453

[8] Ning Y., Guo S.: Flame-retardant and smoke-suppressant properties of zinc borate and aluminium trihydrate-filled rigid PVC. Journal of Applied Polymer Science, **77**, 3119–3127 (2000).
DOI: 10.1002/1097-4628(20000929)77:14<3119::AID-APP130>3.0.CO;2-N

[9] Wu S., Cong P., Yu J., Luo X., Mo L.: Experimental investigation of related properties of asphalt binders containing various flame retardants. Fuel, **85**, 1298–1304 (2006).
DOI: 10.1016/j.fuel.2005.10.014

[10] Bourbigot S., Le Bras M., Duquesne S., Rochery M.: Recent advances for intumescent polymers. Macromolecular Materials and Engineering, **289**, 499–511 (2004).
DOI: 10.1002/mame.200400007

[11] Bourbigot S., Duquesne S.: Fire retardant polymers: Recent developments and opportunities. Journal of Materials Chemistry, **17**, 2283–2300 (2007).
DOI: 10.1039/b702511d

[12] Griffiths B.: SETEC 01/-06: The SAMPE Europe Toulouse Conference. High Performance Composites, **14**(11), 22–23 (2006).

[13] Carpentier F., Bourbigot S., Le Bras M., Delobel R., Foulon M.: Charring of fire retarded ethylene vinyl acetate copolymer-magnesium hydroxide/zinc borate formulations. Polymer Degradation and Stability, **69**, 83–92 (2000).
DOI: 10.1016/S0141-3910(00)00044-6

[14] Genovese A., Shanks R. A.: Structural and thermal interpretation of the synergy and interactions between the fire retardants magnesium hydroxide and zinc borate. Polymer Degradation and Stability, **92**, 2–13 (2007).
DOI: 10.1016/j.polymdegradstab.2006.10.006

[15] Hu Z. S., Dong J. X., Chen G. X.: Study on anti wear and reducing friction additive of nanometer ferric oxide. Tribology International, **31**, 355–360 (1998).
DOI: 10.1016/S0301-679X(98)00042-5

[16] Diagne M., Guèye M., Vidal L., Tidjani A.: Thermal stability and fire retardant performance of photo-oxidized nanocomposites of polypropylene-graft-maleic anhydride/clay. Polymer Degradation and Stability, **89**, 418–426 (2005).
DOI: 10.1016/j.polymdegradstab.2005.01.032

[17] Xie R. C., Qu B. J.: Expandable graphite systems for halogen-free flame-retarding of polyolefins. I. Flammability characterization and synergistic effect. Journal of Applied Polymer Science, **80**, 1181–1189 (2001).
DOI: 10.1002/app.1202

[18] Shen K. K., Olson E.: Recent advances on the use of borates as fire retardants in polymers. Sixteenth Annual BCC Conference on Flame Retardancy, Stamford, USA, 286–288 (2005).

[19] Zhang S., Horrocks A. R.: A review of flame retardant polypropylene fibres. Progress in Polymer Science, **28**, 1517–1538 (2003).
DOI: 10.1016/j.progpolymsci.2003.09.001

[20] Samyn F., Bourbigot S., Duquesne S., Delobel R.: Effect of zinc borate on the thermal degradation of ammonium polyphosphate. Thermochimica, **456**, 134–144 (2007).
DOI: 10.1016/j.tca.2007.02.006

[21] Mouritz A. P., Gibson A. G.: Fire properties of polymer composites materials. Springer, Berlin (2006).

[22] Franchini M. C., Fabbri P., Frache A., Ori G., Messori M., Siligardi C., Ricci A.: Bentonite-based organoclays as innovative flame retardant agents for SBS copolymer. Journal of Nanoscience and Nanotechnology, **8**, 6316–6324 (2008).
DOI: 10.1166/jnn.2008.379

[23] Schartel B., Hull T. R.: Development of fire-retarded materials – Interpretation of cone calorimeter data. Fire and Materials, **31**, 327–354 (2007).
DOI: 10.1002/fam.949

eXPRESS Polymer Letters Vol.3, No.6 (2009) 385–399
Available online at www.expresspolymlett.com
DOI: 10.3144/expresspolymlett.2009.48

A critical analysis of the models connecting molecular mass distribution and shear viscosity functions

*L. Macskási**

Scientific Society of Mechanical Engineering, Fő utca 68, H-1027 Budapest, Hungary

Received 15 January 2009; accepted in revised form 9 April 2009

Abstract. Thermoplastics having various short and long-chain branches, characterized by the melt index measured at the processing temperature – according to their average molecular mass – can be processed using universal principles, independently of their chemical composition. The average molecular mass is the result of a molecular mass distribution, being the fingerprint of the chemical synthetic technology. The actual shape of the shear viscosity function aiming at the quantitative characterization of viscous flow, containing material-dependent parameters, depends on the ratio of high and low molecular mass fractions, the width of the molecular mass distribution function and on the number of short and long chain branches. This publication deals with the critical analysis of the mathematical methods of transforming these two curves of basic importance into each other.

Keywords: *rheology, molecular mass, molecular mass distribution, shear viscosity function, direct and indirect transformation model*

1. Introduction

1.1. Establishing a research hypothesis

Table 1 shows the stations of the technical-scientific quest during which a plastic product is made by cooling and shaping a melt produced by melting a polymer mass in the plastics processing industry. There are three separate, well-defined research areas: polymer structure research, testing the viscous flow properties of polymer melts, and testing the processing properties. First two are mainly scientific disciplines, the third is a practice-oriented activity. Our main interest was in establishing mutual relations between them, taking into account especially the works of Bersted [1–3], Malkin and Teishev [4–6], Tuminello and coworkers [7, 8] and Nobile et al. [9], who dealt first with determining the molecular mass distribution functions of thermoplastics from melt viscosity functions.

2. Experimental

2.1. Materials

The materials used in our experiments were
– polystyrenes of Edistir type (Dunasytr Plc, Hungary), samples denoted as PS 1-11
– PVC pellets of various K-values of Ongrolit type, (BorsodChem Plc, Hungary), samples denoted as PVC 1-6
– polypropylene homopolymers of Tipplen type (TVK Plc, Hungary), samples denoted as PP 1-6

The samples are listed in Table 2.

2.2. Test methods

2.2.1. Determining the molecular mass distribution by GPC

The molecular mass of polymers influences their general performance, such as tensile strength, elas-

*Corresponding author, e-mail: macskasi.levente@chello.hu

Table 1. Research hypothesis

A	**Polymers**	AB/BA	B	**Polymer melts**	BC	C	**Processing properties**		
Molecular mass distribution		Mutual correspondence between polymer structure and macroscopically measurable flow properties	Flow curve		Determining melt elasticity (rheological swelling) from shear flow data	Extrusion	Exit pressure		
Molecular mass			Shear viscosity function				Rheological swelling		
Short chain branching			Normal stress curve				Elastic turbulence (melt fracture)		
Long chain branching			Normal viscosity function			Injection molding	Internal pressure in the mold		
Structural studies			**Rheological tests**			**Rheological swelling**	Yes	No	
Gel permeation chromatography			Capillary viscometer			Processing method	Extrusion	Injection molding	
X-ray diffraction			Rotation viscometer			Molecular mass	Medium and high	Low and medium	
Infrared spectroscopy			Extrusiometer			Molecular mass distribution	Wide	Medium	
			Injection mold with built-in sensors			Temperature	Low and medium	High	
			Extensional rheometer			Production rate	Low and medium	High	

Table 2. Carreau parameters obtained by fitting the rheological test results of the polymers studied at 190°C by Equation (6) and the molecular mass distribution constants of Equation (1) obtained from the GPC data

Polymer	**Carreau parameters**				**GPC test data**				**Parameters of the molecular mass distribution curve**		
	η_0 [Pa·s]	λ [s]	M	N	$\bar{M}_m$	$\bar{M}_n$	$\bar{M}_m/\bar{M}_n$	M_{max}	α	σ	μ
EDISTIR polystyrene											
PS-1	23451	0.930	0.771	0.773	162634	64072	2.538	132359	0.026503	0.6305	4.9559
PS-2	18131	0.774	0.760	0.749	157532	58431	2.696	124360	0.026422	0.6860	4.9116
PS-3	11762	0.580	0.983	0.553	160375	62151	2.580	150795	0.026831	0.6444	4.9172
PS-4	43449	1.433	0.891	0.713	176472	71525	2.467	138452	0.027770	0.5758	5.0266
PS-5	23955	0.951	0.825	0.711	189487	88165	2.149	160388	0.025332	0.5200	5.0492
PS-6	48157	2.208	0.777	0.779	158968	58993	2.695	128254	0.023147	0.7882	4.9204
PS-7	41720	1.369	0.763	0.816	131583	59117	2.226	102684	0.028333	0.6216	4.9437
PS-8	13197	0.551	0.873	0.677	150708	55342	2.723	124857	0.027397	0.6978	4.9101
PS-9	61515	2.673	0.865	0.701	187972	95438	2.873	151415	0.027990	0.7419	4.9958
PS-10	39817	1.564	0.816	0.768	150680	55797	2.701	112421	0.026919	0.5917	5.0165
PS-11	77149	4.110	0.714	0.842	150798	53184	2.835	124135	0.029322	0.5970	5.1160
ONGROLIT PVC											
PVC-1 (K=52)	1432	0.861	0.426	0.362	80035	40049	1.998	68941	0.02585	0.5212	4.7364
PVC-2 (K=58)	7824	0.782	0.725	0.575	106986	52384	2.042	89182	0.02634	0.5292	4.8465
PVC-3 (K=64)	19759	0.481	0.988	0.586	145541	68544	2.123	119524	0.02768	0.5722	4.9804
PVC-4 (K=67)	32531	0.636	1.027	0.603	164508	80261	2.050	133922	0.02742	0.5160	5.0522
PVC-5 (K=70)	50453	0.677	1.445	0.483	188065	87418	2.151	160780	0.02919	0.5509	5.1185
PVC-6 (K=77)	167418	0.855	1.028	0.923	253923	114367	2.220	192797	0.02822	0.5481	5.2508
TIPPLEN polypropylene											
PP-1	1491	0.076	0.845	0.679	212850	45274	4.701	110710	0.05481	0.8058	4.9795
PP-2	1470	0.066	0.901	0.672	219166	46200	4.744	118050	0.05740	0.7840	4.9762
PP-3	7479	0.448	0.724	0.791	269912	55980	4.822	158117	0.04550	0.7828	4.9858
PP-4	11009	0.706	0.912	0.618	336073	68097	4.935	188315	0.04519	0.8634	5.1434
PP-5	61349	2.826	1.288	0.468	480786	89048	5.399	319716	0.03139	0.8710	5.1959
PP-6	69067	1.821	1.067	0.570	617606	107993	5.719	526621	0.03371	0.9653	5.3282

ticity modulus, while their molecular mass distribution plays a decisive role in their processing.

In order to determine the molecular mass distribution the polymer is usually dissolved and the so-called size-exclusion chromatogram (or gel permeation chromatogram, GPC) is determined. The are no known solvents for certain polymers (e.g. poly(tetrafluorethylene), poly(ether-ether-ketone)), while other can be studied only at high temperature (polyolefins). Solvent based techniques are usually time consuming not because of the GPC test islef, but because of the dissolution of the polymer sample.

Solutions of about 5 mg/ml concentration were made from PS in tetrahydrofurane and from PVC in cyclohexanone at room temperature, while solutions of about 0.5–1 mg/ml concentration were made from PP in 1,2,4-trichlorobenzene at 160°C, which were filtered on filters with 1 μm pore diameter. Molecular mass distribution curves of PS and PVC samples were measured at room temperature using a *Waters* gel permeation chromatograph (GPC), while the molecular mass distribution of PP samples was determined by a Polymer Laboratories GPC 220 equipment at 160°C. Polystyrene standards were used for calibration in each case.

2.2.2. Determining the shear viscosity function

Modern rheological test equipments (oscillating rheometers and capillary or rotation viscometers) make possible determining the frequency dependence of storage and loss moduli or the flow curves within 20 minutes and 1–2 hours respectively, covering 4 orders of magnitude frequency range or 6–8 orders of magnitude shear rate range respectively. They need neither solvent nor filtering. Therefore, rheological tests are ideally suited for quality control.

Mass and volume flows of the melts were measured using standard capillaries at 190°C, using 1–21.6 kg load. Shear stress, shear rate and shear viscosity values were calculated from the test data.

3. Quantitative description of the molecular mass distribution and critical analysis of determining their maximum shear viscosity

3.1. Mathematical description of the molecular mass distribution determined by GPC method

Characteristic parameters of the distribution curve are determined by the GPC test software, namely the mass- and number average molecular masses and the molecular mass belonging to the maximum of the distribution function.

Mass average molecular mass of the polymers studied was in the range of $100\,000 < (\overline{M}_m) < 600\,000$ their polydispersity was moderate ($2 < \overline{M}_m/\overline{M}_n < 6$). The functional form, i.e. the differential molecular mass distribution was described by the so-called log-normal distribution (Equation (1)):

$$y = \frac{a}{\sigma}\cdot\exp\left[-\frac{1}{2}\cdot\frac{\ln x - \mu}{\sigma^2}\right] \tag{1}$$

which is strictly valid only for linear, monodisperse polymers, mainly for polyethylene [10], but can be used as a good approximation for commercial polymers (e.g. for polypropylene, polystyrene, and PVC samples [11]), provided that they do not contain too many branches and if the polydispersity is not too large. a is a constant characterizing the maximum of the curve, σ is the standard deviation of the distribution, x is the molecular mass, μ is the molecular mass belonging to the maximum of the curve. Using the constants of Equation (1) the polydispersitiy index of the polymer is given by Equation (2):

$$\frac{\overline{M}_m}{\overline{M}_n} = 1 + \left(\frac{\sigma}{\mu}\right)^2 \tag{2}$$

3.2. Critical analysis of the determination of the maximum shear viscosity

The shear viscosity function of polymer melts can be determined by a combined use of rotational and capillary rheometers in a broad shear rate range. Viscosity values close to the zero shear rate can be obtained by the former, while viscosities closer to the values encountered in practice can be obtained by the latter. Depending on the polymer and on the temperature it is possible to measure points at low shear rates (~0.1 s^{-1}) by capillary rheometers, but these are not typical.

The functional relation is usually described by functions containing 2, 3 or 4 parameters, resulting in gradually smaller fitting errors. Equations with 2 parameters cannot handle the Newtonian behavior, which can be described only by equations containing 3–4 parameters. One has to interpret the physical meaning of the parameters and the reality of the maximum viscosity value obtained.

The problem of determining the η_0 values lies in the fact that test data are determined in the so-called non-Newtonian range, and the usual, simpler extrapolation methods do not treat this range adequately.

When describing the shear viscosity as a function of the shear rate by Equation (3):

$$\eta = \frac{1}{a_1\dot{\gamma} + b_1} \tag{3}$$

and linearization $b_1 = 1/\eta_0$ is yielded by the intercept.

Describing the shear viscosity by another function, namely Equation (4):

$$\eta = \frac{(\eta_0)_2}{\dot{\gamma}^{a_2}} \tag{4}$$

After linearization the shear viscosity belonging to $\dot{\gamma} = 1\ s^{-1}$ is the intercept, i.e. $(\ln \eta_0)_2$ and the shear viscosity increases monotonously and continuously with decreasing shear rates which is physically impossible.

When using a three-parameter Equation (5):

$$\eta = \frac{(\eta_0)_3}{(\dot{\gamma} + b_3)^{a_3}} \tag{5}$$

the horizontal section characteristic of the Newtonian range, i.e. the maximum shear viscosity appears in the logarithmic plot, but parameters a_3 and b_3 have no physical meaning.

The Carreau equation originally containing 3 parameters [12] has been modified to contain 4 parameters (see Equation (6)):

$$\eta = \frac{(\eta_0)_4}{[1 + (b_4\dot{\gamma})^{c_4}]^{a_4}} \tag{6}$$

which contains not only the maximum shear viscosity (η_0) but also the relaxation time ($b_4 = \lambda$), as a material constant, a value (c_4) characterizing the molecular mass distribution and a further parameter (a_4) characterizing the non-Newtonian behavior can also be determined from it.

Figure 1 shows the curves fitted to shear viscosity data measured on PS-4 at 190°C. We concluded, that at low shear rates Equation (4), while at high shear rates Equation (3) leads to erroneous conclusions, reflected by the relatively large fitting errors (18.06 and 9.13% respectively). Equations (5) and (6) can be well applied in the whole shear rate range, the fitting errors are only 2.38 and 2.15% respectively.

Carreau parameters of PS, PVC and PP samples determined form 190°C rheological tests are collected in Table 2 together with the parameters of the molecular mass distribution functions determined by GPC.

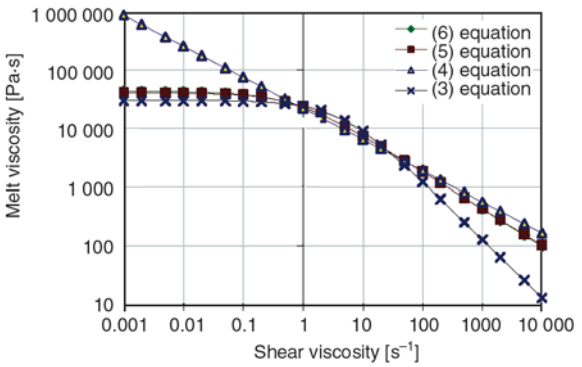

Figure 1. Determining the maximum shear viscosity of sample PS-4 by approximate equations at 190°C

3.3. Relation between the maximum shear viscosity and the mass average molecular mass

3.3.1. Literature data

Calculation the maximum shear viscosity is of great theoretical importance, as it is directly related to the mass average molecular mass of the polymer, as shown by Equation (7) [13–15]:

$$\eta_0 = K_1 \cdot \overline{M}_m^{\alpha} \tag{7}$$

Parameters collected from the literature for HDPE, PS and PP are listed in Table 3. It has to be noted that K_1 parameters were obtained using zero shear viscosities using Poise units.

Figure 2 shows the relations between shear viscosities and mass average molecular masses for our PS,

Table 3. The constants of Equation (7) for various polymers at 190°C

	Polymer	K_1	α	R^2	Reference
Literature data	HDPE	–12.700	3.5200		[16]
	PS	–12.800	3.4000		[17]
	PP	–11.900	3.6900		[18]
Calculated from test data	PS	–32.545	7.0823	0.9964	
	PP	–17.099	3.8211	0.9475	
	PVC	–16.207	3.9698	0.9881	

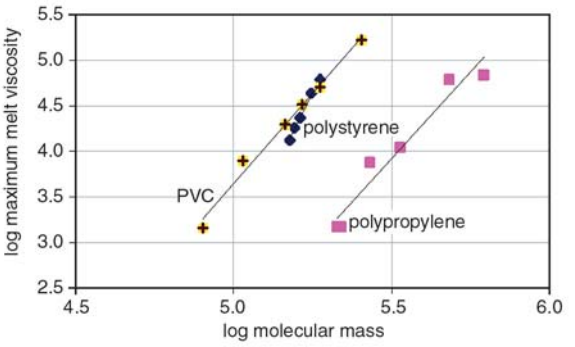

Figure 2. Maximum shear viscosities determined at 190°C plotted against the molecular mass

PP and PVC samples. Zero shear viscosities are given here already in SI units.

The molecular mass range of the PS samples studied covers a very narrow range and, according to Equation (7) the slope is about double of the value obtained from the literature.

The exponent calculated for the polystyrene sample is too high, therefore the calculated molecular masses are far from the GPC results. The reason for this discrepancy is that the shear rated which can be realized in the capillary viscometer is not low enough to obtain a reliable zero shear viscosity by processing the data using the Carreau equation. There are two further methods which, however, require special instrument. Zero shear viscosity can be determined by oscillating rheometry. A third method uses the slope of the steady state of the deformation curve determined by creep experiments at low stresses.

4. A model used for transforming molecular mass distribution curves into shear viscosity functions

4.1. Theory

When establishing the relation between the polymer structure and macroscopically observed properties we started from the obvious fact that shear viscosity depends mainly of the chain length distribution, on the temperature and last, but not least on the shear rate [19, 20].

Bersted in his works [1–3] defined a critical molecular mass M_c, below which the molecular flow is regarded as Newtonian, while above this value the viscosity decreases with the shear rate. The critical molecular mass is essentially related to the Newtonian/non-Newtonian transition in the flow curve, which in its turn is related to the maximum relaxation time. Consequently the onset of the non-Newtonian flow is related to the longest relaxation time of the polymer sample.

Stated otherwise it is assumed that for each shear rate there exists a M_c critical molecular mass. If $M < M_c$ the weight of contribution of molecules to the viscosity is proportional to w_iM_i, while if $M \geq M_c$ the contribution is proportional to their weight fraction, as if their molecular mass were M_c. It is further assumed that the threshold value is independent of the average molecular mass of the sample and of the molecular mass distribution of the whole sample.

4.2. Calculation method

In order to determine the critical molecular mass we start from the well known Equation (4) between maximum shear viscosity (η_0) and mass average molecular mass $\overline{M}_m$ as described in linearized form by Equation (8):

$$\lg \eta(\dot{\gamma}) = K_1 + \alpha \cdot \lg \overline{M}_m \tag{8}$$

where Equation (9) defines the meaning of $\overline{M}_m$:

$$\overline{M}_m = \sum_{i=1}^{c-1} w_i M_i + M_c \sum_{i=c}^{\infty} w_i \tag{9}$$

where w_i is the mass fraction of the i-th component and M_i is the molecular mass of the i-th component. The molecular mass distribution curve has been divided into $i = 54$ discrete points (see Figure 3).

Rheological constants of the studied polymer types were determined form the shear viscosities measured at 190°C using the Carreau equation (see Equation (10)):

$$\eta = \frac{\eta_0}{[1 + (\lambda \cdot \dot{\gamma})^M]^N} \tag{10}$$

wherein η_0 is the maximum shear viscosity in Pa·s units; λ is the relaxation time [sec]; M is a dimensionless constant characterizing the molecular mass distribution, while N is another dimensionless constant characterizing the non-Newtonian behavior. At a given shear rate the 'apparent' molecular masses are calculated from Equation (8), from which the M_c value is calculated using Equation (9).

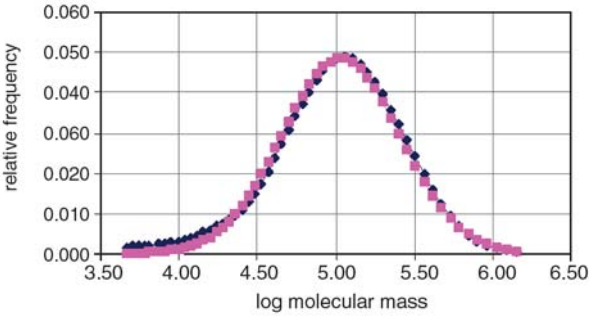

Figure 3. Molecular mass distribution of sample PS-4. 1 – GPC data, 2 – the curve fitted by Equation (1)

Table 4. Calculation of critical molecular mass of sample PS-4

Shear rate [s^{-1}]	Viscosity [Pa·s]	Molecular mass	M_c Critical molecular mass								
			i = 30	i = 33	i = 34	i = 35	i = 36	i = 37	i = 38	i = 39	i = 40
1	18334	205458	307909	372962	403199	439192	482179	534168	597966	677532	777749
10	5921	147352	212793	249068	264817	282740	303060	326200	352689	383174	418180
20	4074	132004	187670	216343	228266	241415	255748	271268	287902	305423	323205
100	1690	101906	138401	152168	156587	160376	162967	163545	160853	152951	136955
1000	477	70237	86561	84643	81166	75106	65343	50198	27171	–7480	–59018
2000	326	62788	74367	68760	63426	55049	42381	23537	–4273	–45216	–105113
5000	197	54138	60209	50318	42827	31761	15718	–7420	–40783	–89033	–158636
10000	134	48396	50809	38074	29152	16300	–1983	–27972	–65023	–118122	–194170

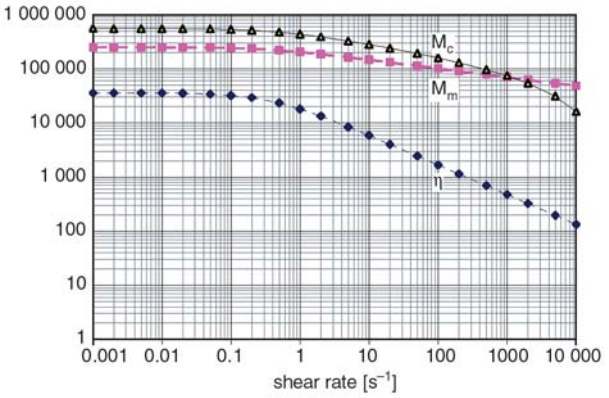

Figure 4. Shear viscosity (η, in Pa·s units), molecular mass (M_m) and critical molecular mass (M_c) of sample PS-4 as a function the shear rate

When determining the M_c values it was observed that after a certain i value M_c becomes negative, which is physically meaningless. Therefore an $i = c$ value was adopted, where a positive M_c was obtained even at the highest shear rate, i.e. $i = 35$ (Table 4).

When plotting the logarithm of the M_c values against the logarithm of the shear rate a monotonically decreasing curve was obtained. Using the slope of the latter the following Equation (11) was used to calculate the M_c values:

$$M_c = M_{c,0} \cdot \dot{\gamma}^{-1/4} \tag{11}$$

where $M_{c,0} = 320\,000$ is used for PS [1].

A serious drawback of Equation (11) is that it approximates the measured shear viscosity function only in the non-Newtonian rage, but it cannot be used to calculate the Newtonian range. We tried to eliminate this deficiency first by a relation of $M_c = a/(\dot{\gamma} + b)$ but a good result was obtained only by using a relation of $M_c = A/[1 + (B \cdot \dot{\gamma})^C]^D$ (see Figure 4).

4.3. Results and discussion

The molecular mass distribution is transformed into the shear viscosity function in the following way:

(1) knowing the average molecular mass and the molecular mass distribution curve of the polymer one calculates $A = M_c$ at zero shear rate using Equation (12):

$$A = M_{c(\dot{\gamma}=0)} = \frac{\overline{M}_m - \sum_{i=1}^{c-1} w_i M_i}{\sum_{i=c}^{\infty} w_i} \tag{12}$$

for an $i = c$ value as close as possible to the average molecular mass.

(2) then the points of the shear viscosity function are calculated using Equation (13):

$$\eta = \exp\left\{K_1 + \alpha \cdot \lg\left[\sum_{i=1}^{c-1} w_i M_i + \frac{A}{(B \cdot \dot{\gamma}^C + 1)^D} \cdot \sum_{i=c}^{\infty} w_i\right]\right\} \tag{13}$$

Table 5 summarizes the data obtained from the GPC curves of the PS, PVC and PP samples, the constants of the measured and calculated shear viscosity functions and their deviations. Relative differences, $\sum_i 100 \cdot [(|\eta_{measured} - \eta_{calculated}|)/\eta_{measured}]$ are mostly within 10%.

5. Model used to determine molecular mass distribution of thermoplastic polymers from dimensionless rheological data

5.1. Theory

Having discussed the direct problem (i.e. the determination of the flow curve from a known molecular mass distribution) in Chapter 4 the following question is asked: is it possible to calculate the molecu-

Table 5. Parameters of the measured and calculated shear viscosity functions of the polymers tested and their relative differences

Polymer	GPC curve			Shear viscosity function (measured)				Shear viscosity function (calculated)				Rel. diff. [%]
	i = c	$\sum_{i=c}^{\infty} w_i$	$\sum_{i=1}^{c-1} w_i M_i$	η [Pa·s]	λ [s]	M [–]	N [–]	A	B	C	D	
EDISTIR polystyrene												
PS-1	36	0.2991	47019	23451	0.930	0.771	0.773	517979	0.2059	0.5658	0.8393	8.093
PS-2	34	0.3896	40387	18131	0.774	0.760	0.749	429558	0.2289	0.4765	0.9533	13.247
PS-3	34	0.3661	44471	11762	0.580	0.983	0.553	377485	0.1500	0.5198	1.0569	6.852
PS-4	35	0.3714	42342	43449	1.433	0.891	0.713	590576	0.3540	0.4137	1.0686	8.244
PS-5	29	0.4685	40725	23955	0.951	0.825	0.711	397664	0.2447	0.4614	1.0153	6.392
PS-6	34	0.4877	32162	48157	2.208	0.777	0.779	512694	0.4319	0.4058	0.9238	6.029
PS-7	36	0.2954	49504	41720	1.369	0.763	0.816	699714	0.2205	0.4054	1.4811	8.838
PS-8	34	0.3842	38520	13197	0.551	0.873	0.677	390846	0.1582	0.4974	1.0616	6.545
PS-9	34	0.4143	43666	61515	2.673	0.865	0.701	647189	0.3035	0.3638	1.4798	8.619
PS-10	36	0.3242	47493	39817	1.564	0.816	0.768	638157	0.2900	0.4514	1.1377	10.236
PS-11	26	0.3502	54752	77149	4.110	0.714	0.842	635773	0.2645	0.4005	1.4376	10.369
average								530694	0.2593	0.4510	1.1323	
ONGROLIT PVC												
PVC-1	38	0.1093	52452	1432	0.8613	0.4262	0.3618	210222	0.1614	0.3754	1.3456	1.905
PVC-2	32	0.3014	39808	7824	0.7817	0.7252	0.5751	253643	0.2355	0.5238	0.6539	4.033
PVC-3	29	0.4116	37204	19759	0.4814	0.9878	0.5859	265778	0.1747	0.6005	0.6584	5.677
PVC-4	28	0.4598	36431	32531	0.6361	1.0273	0.6028	285609	0.6165	0.5507	0.7320	6.480
PVC-5	27	0.4941	35451	50453	0.6770	1.4448	0.4833	303241	0.1922	0.8042	0.4917	9.247
PVC-6	24	0.6382	25541	167418	0.8545	1.0281	0.9231	360242	0.2748	0.5590	0.8721	11.649
average								279789	0.2759	0.5689	0.7923	
TIPPLEN polypropylene												
PP-1	32	0.2207	71954	1491	0.0762	0.8454	0.6795	591533	0.04397	0.6027	1.0503	4.206
PP-2	32	0.2271	71143	1470	0.0655	0.9006	0.6720	574811	0.03294	0.6099	1.2131	4.708
PP-3	34	0.2010	112249	7479	0.4478	0.7236	0.7911	980237	0.03764	0.5296	1.3421	2.860
PP-4	31	0.3464	79132	11009	0.7061	0.9115	0.6180	768597	0.19658	0.4688	0.9415	6.047
PP-5	31	0.4442	87236	61349	2.8264	1.2884	0.4681	1066568	0.30630	0.3872	1.1782	11.270
PP-6	30	0.4604	112572	69067	1.8207	1.0668	0.5705	988648	0.23650	0.4343	1.2560	9.704
average								828399	0.14230	0.5054	1.1635	

lar mass distribution from the shear viscosity function? This so-called 'inverse problem' is regarded as 'ill-defined' by Malkin and Teishev [4–6], Tuminello and coworkers [7, 8] and Nobile et al. [9]. Although molecular mass distribution curves calculated from low amplitude dynamic oscillation tests have been published in the literature, the algorithm has not been published [21, 22].

Typical industrial polymers are polydisperse, i.e. they can be regarded as mixtures of monodisperse fractions. Flow curves/shear viscosity functions of monodisperse polymer melts can be described by Equation (14):

$$\eta(\dot{\gamma}) = \begin{cases} \eta_0 & \text{if} \quad \tau \le \tau_s \quad \text{or} \quad \dot{\gamma} \le \dot{\gamma}_s \\ \dfrac{\tau_s}{\dot{\gamma}} & \text{if} \quad \tau > \tau_s \quad \text{or} \quad \dot{\gamma} > \dot{\gamma}_s \end{cases} \tag{14}$$

where η_0 is the maximum shear viscosity, τ_s the critical shear stress and $\dot{\gamma}_s = \tau_s/\eta_0$ is the critical shear rate depending on the molecular mass of the high molecular mass fractions.

The molecular mass dependence of η_0 is given by Equation (7) wherein K and α are constants (α = 3.4–3.5). The critical shear rate can be calculated by Equation (15):

$$\dot{\gamma}_s = \frac{\tau_s}{\eta_0(M)} = \frac{\tau_s}{K\overline{M}^{\alpha}} \tag{15}$$

Equation (15) is strictly valid only for monodisperse polymers, for polydisperse samples mass average molecular mass $\overline{M}_m$ should be used. For a binary mixture of homodisperse polymers with M_1 and M_2 ($M_1 > M_2$) Friedman and Porter [23] introduced the following Equation (16):

$$\eta_{0,combination} = K\overline{M}_m^{\alpha} = (w_1\eta_{0,1}^{1/\alpha} + w_2\eta_{0,1}^{1/\alpha})^{\alpha} \tag{16}$$

where $\eta_{0,1}$ and $\eta_{0,2}$ are Newtonian viscosities and w_1, w_2 are the mass fractions of the components.

The flow curve/viscosity function of the binary mixture can be expressed by Equation (17):

$$\eta(\dot{\gamma}) = \begin{cases} K(w_1 M_1 + w_2 M_2)^{\alpha} & \text{if} \quad \dot{\gamma} \le \dfrac{\tau_s}{K M_1^{\alpha}} \quad (17a) \\ \left[w_1 \left(\dfrac{\tau_s}{\dot{\gamma}} \right)^{1/\alpha} + w_2 K^{1/\alpha} M_2 \right]^{\alpha} & \text{if} \quad \dfrac{\tau_s}{K M_1^{\alpha}} \le \dot{\gamma} \le \dfrac{\tau_s}{K M_2^{\alpha}} \quad (17b) \\ \dfrac{\tau_s}{\dot{\gamma}} & \text{if} \quad \dot{\gamma} \ge \dfrac{\tau_s}{K M_2^{\alpha}} \quad (17c) \end{cases}$$

This approximation has been generalized by Nobile et al. [9] for a continuous molecular mass distribution as shown by Equation (18):

$$\eta(\dot{\gamma}) = \left[\int_0^{M(\dot{\gamma})} (K M^a)^{1/\alpha} f(M) \mathrm{d}M + \left(\frac{\tau_s}{\dot{\gamma}} \right)^{1/\alpha} \int_{M(\dot{\gamma})}^{\infty} f(M) \mathrm{d}M \right]^{\alpha} \quad (18)$$

where $f(M)$ is the molecular mass distribution function.

The first member of Equation (18) corresponds to the second member of Equation (17b) while its second member corresponds to the first member of Equation (17b). The first member of Equation (18) represents the Newtonian flow, while its second member is related to those high molecular mass fractions, which take part in the non-Newtonian flow.

In order to solve the inverse problem three dimensionless variables are needed, namely

– dimensionless shear viscosity according to Equation (19):

$$Y = \left[\frac{\eta(\dot{\gamma})}{\eta_0} \right]^{1/\alpha} \quad (19)$$

– dimensionless shear rate according to Equation (20):

$$X = \left(\frac{\dot{\gamma}}{\dot{\gamma}_s} \right)^{1/\alpha} \quad (20)$$

– and dimensionless molecular mass according to Equation (21):

$$m = \frac{1}{X} = \frac{M}{\overline{M}_m} \quad (21)$$

where the molar masses belonging to certain shear rates should be used instead of M, as shown by Equation (22):

$$M = \frac{10^{\frac{1}{\alpha}(\lg \eta_0 + K)}}{\left(\dfrac{\lambda \dot{\gamma}}{k} \right)^{1/\alpha}} \quad (22)$$

where η_0 is the maximum shear viscosity, K is a constant characterizing the polymer, λ is the relaxation time, $\dot{\gamma}$ is the actual shear rate and $k = 1$.

Without presenting the derivation the solution of the inverse problem is given by Equation (23):

$$f\left(\frac{1}{X} \right)_{\frac{1}{X}=m} = -\left(X^4 \frac{\mathrm{d}^2 Y}{\mathrm{d}X^2} + 2X^3 \frac{\mathrm{d}Y}{\mathrm{d}X} \right) \quad (23)$$

5.2. Calculation of the molecular mass distribution

Equation (23) can be made appropriate for calculations if the Carreau equation modified by us is inserted into Equation (24):

$$Y = \frac{1}{[1 + (kX^{\alpha})^M]^{N/\alpha}} \quad (24)$$

then it is derived twice with respect to X as shown in Equation (25):

$$\frac{\mathrm{d}^2 Y}{\mathrm{d}X^3} = MNk^M X^{\alpha M - 2} \cdot \frac{M(N+\alpha)k^M X^{\alpha M} - (\alpha M - 1)(1 + k^M X^{\alpha M})}{(1 + k^M X^{\alpha M})^{(N/\alpha + 2)}} \quad (25)$$

Using Equation (25) the frequency of each molecular mass in any polymer sample can be determined as a function of the shear rates used in the rheologi-

cal test if the Carreau constants (λ, M, N), and the constants of the given polymer (k and α) are known.

5.3. Results and discussion. Comparison of calculated and measured molecular mass distributions

GPC curves are usually taken at points equally distributed along the log (molecular mass) axis, therefore it would be useful to distribute uniformly the test points along a logarithmic scale for melt viscosity tests too. The latter is hampered by the fact that even with up-to-date capillary rheometers one can take 6–8 (10) test point pairs (depending on the conditions). Intermediate points in the measured shear rate interval can be estimated by interpolation using the fitted shear viscosity function. A major problem is that in the case of $\dot{\gamma} < 0.1$ s^{-1} test are impossible, or even if one can measure 1–2 points for low viscosity melts, the scatter of parallel points will be unacceptably high. The same is true for tests at $\dot{\gamma} > 100$ s^{-1} where short test times do not allow the establishment of stationary flow. Additionally one cannot maintain the constant test temperature because of fictional heating. Thus the shear viscosity function must be extrapolated above and below the tested interval in order to estimate the high and low molecular mass branches of the molecular mass distribution function.

We could not describe the breadth of the distribution using the algorithm developed for the indirect problem. For a long time the Carreau parameters were blamed for this failure, but without success. Later we concentrated on the effect of varying k and especially α which brought us closer to the solution of the problem.

The lack of success was due to the improper exponent value in equation $\eta_0 = K\overline{M}_m^{\alpha}$. We stuck too much to the $\alpha = 3.4$ regarded as universal in the literature which made impossible the approximately correct prediction of the molecular mass distribution. If a smaller α value is chosen, the lower (high molecular mass) and higher (low molecular mass) portions of the distribution function can be approximated with acceptable error. The irregular double peak still remains in the central range, which has been published in ref. [22] too.

The problem mentioned above is related to the accuracy of shear viscosity determination, which can be illustrated by the $\ln \eta_0 - \overline{M}_m$ relation. The sensitivity of η_0 to the molecular mass at infinite shear rate is unity ($\alpha = 1.0$), while at zero shear viscosity it is much higher ($\alpha = 3.4$). At 190°C, depending on the polymer the lowest shear rate, from where extrapolation to zero shear viscosity is performed is 0,5–20 s^{-1} therefore the empirically found values of $2 < \alpha \leq 3.4$ seem to be logical.

Figures 5–7 show the calculated and experimental molecular mass distribution curves (the latter are determined by GPC). The shape of the calculated curves deviates considerably from the experimental ones, and the mentioned anomaly appears on all of them. Serious discrepancies are found in the relative frequencies. In the case of the PVC-4 sample, however, a very good agreement was found.

$\overline{M}_m$, $\overline{M}_n$ and $\overline{M}_m/\overline{M}_n$ values calculated from rheological tests and from the GPC are summarized in Table 6. It has been concluded that the model approximates well the original molecular mass distribution. Unfortunately the same cannot be said of mass and number average molecular masses. Both values are underestimated in most cases, the calcu-

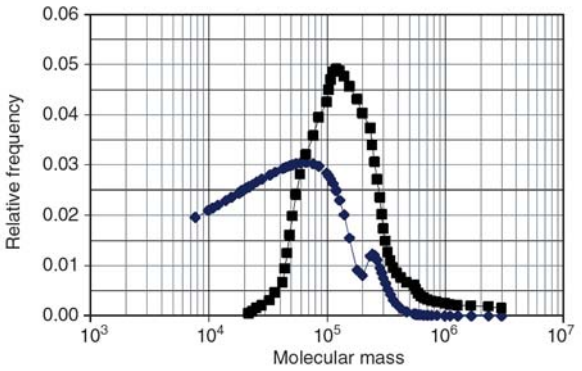

Figure 5. Comparison of calculated (♦) and measured (GPC, ■) molecular mass distribution curves of sample PS-4

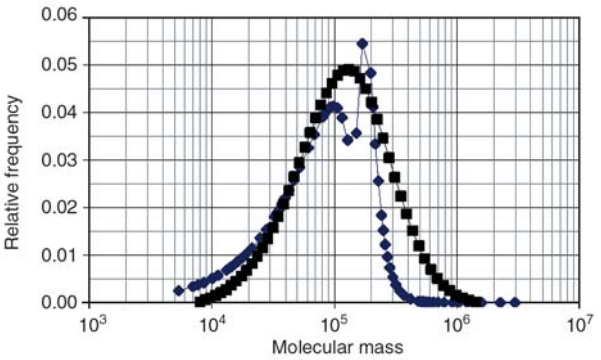

Figure 6. Comparison of calculated (♦) and measured (GPC, ■) molecular mass distribution curves of sample PVC-4

Table 6. Comparison of measured and calculated molecular mass distributions of polystyrene, PVC and polypropylene

Polymer type	Calculated from rheological tests (k = 1)				Obtained form GPC tests			Relative difference* [%]		
	α	$\overline{M}_m$	$\overline{M}_n$	$\overline{M}_m/\overline{M}_n$	$\overline{M}_m$	$\overline{M}_n$	$\overline{M}_m/\overline{M}_n$	$\overline{M}_m$	$\overline{M}_n$	$\overline{M}_m/\overline{M}_n$
EDISTIR polystyrene										
PS–1	2.50	73977	26623	2.779	162634	64072	2.538	–54.51	–58.45	9.48
PS–2	2.60	75399	29189	2.583	157532	58431	2.696	–52.14	–50.05	–4.19
PS–3	2.65	74803	29948	2.498	160375	62151	2.580	–53.36	–51.81	–3.19
PS–4	2.70	79243	32754	2.419	176472	71525	2.467	–55.10	–54.21	–1.93
PS–5	2.80	78929	34608	2.281	189487	88165	2.149	–58.35	60.75	6.13
PS–6	2.50	64685	23279	2.779	158968	58993	2.695	–59.31	–60.54	3.11
PS–7	2.85	83002	37403	2.219	131583	59117	2.226	–36.92	–36.73	–0.31
PS–8	2.50	77018	27718	2.779	150708	55342	2.723	–48.90	–49.92	2.04
PS–9	2.45	63067	21815	2.891	187972	65458	2.873	–66.45	–66.67	0.63
PS–10	2.55	71360	26662	2.676	150680	55797	2.701	–52.64	–52.22	–0.91
PS–11	2.50	57951	20856	2.779	150798	53184	2.835	–61.57	–60.79	–1.99
ONGROLIT PVC										
PVC-1	3.40	53566	28208	1.899	80035	40049	1.998	–33.07	–29.57	–4.96
PVC-2	2.80	77283	36622	2.110	106986	52384	2.042	–27.76	–30.09	3.34
PVC-3	2.55	91487	43707	2.093	145541	68544	2.123	–37.14	–36.24	–1.40
PVC-4	2.55	111655	53689	2.080	164508	80261	2.050	–32.13	–33.11	1.45
PVC-5	2.40	116814	53497	2.184	188065	87418	2.151	–37.89	–38.80	1.51
PVC-6	2.30	209115	100680	2.077	253923	114367	2.220	–17.65	–11.97	–6.44
TIPPLEN polypropylene										
PP-1	2.050	155261	34187	4.542	121850	45274	4.701	27.42	–24.49	–3.39
PP-2	2.025	166486	36659	4.541	219166	46200	4.744	–24.04	–20.65	–4.27
PP-3	1.975	116050	23800	4.876	269912	55980	4.822	–57.00	–57.48	1.12
PP-4	1.950	105580	20858	5.062	336073	68097	4.935	–68.58	–69.37	2.57
PP-5	1.900	95560	18162	5.262	480786	89048	5.399	–80.12	–79.60	–2.55
PP-6	1.875	122628	21480	5.709	617606	107993	5.719	–80.14	–80.11	–0.18

*relative difference = 100 · (calculated from rheological tests – obtained from GPC tests)/(obtained from GPC tests)

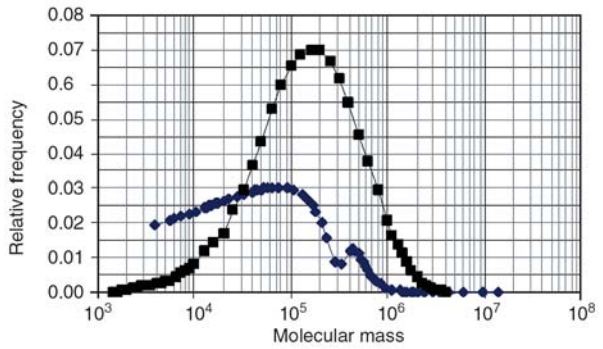

Figure 7. Comparison of calculated (♦) and measured (GPC, ■) molecular mass distribution curves of sample PP-3

lated values are about half – two third of the values obtained form the GPC tests.

5.4. Critical evaluation of the applicability of the model

Table 7. shows how the mass- and number average molecular masses and the distribution itself change with the maximum shear viscosity and with the relaxation time. The data reflect a positive feature of the model, namely

– number average molecular mass ($\overline{M}_n$) increases parallel with the maximum shear viscosity, i.e.

Table 7. Mass- and number average molecular masses and polydispersities obtained form them

As a function of the maximum viscosity (λ = 1.0 s, M = 0.8, N = 0.7)							
η_0 [Pa·s]	12500	15000	17500	20000	22500	25000	30000
$\overline{M}_m$	105805	111634	116812	121491	125773	129732	136878
$\overline{M}_n$	36283	38281	40057	41661	43130	44487	46938
$\overline{M}_m/\overline{M}_n$	2.916						
As a function of the relaxation time (η_0 = 22500 Pa·s, M = 0.8, N = 0.7)							
λ [s]	0.25	0.50	0.75	1.00	1.25	1.50	2.00
$\overline{M}_m$	116771	122194	125498	125773	124263	122262	118476
$\overline{M}_n$	50014	46234	44575	43130	41610	40196	37908
$\overline{M}_m/\overline{M}_n$	2.335	2.643	2.815	2.916	2.986	3.042	3.125

with the mass average molecular mass ($\overline{M}_n$), the distribution remains constant, if the relaxation time (λ) and the Carreau parameters (M and N) remain constant;
– the increase of the relaxation time (λ) results in the broadening of the distribution curve if the maximum shear viscosity (η_0), and the Carreau parameters (M and N) are kept constant.

A negative feature of the model is that by increasing the M parameter of the Carreau equation results in a gradually narrower distribution, i.e. the algorithm handles the breadth of the molecular mass distribution inversely.

6. Prediction of the molecular mass distribution of thermoplastics using a model based on the GEX function

6.1. Theory

The method described in Chapter 5. was based on the double derivation of the experimentally determined shear viscosity function. The integral molecular mass distribution function was obtained by processing the first and second derivatives using the described algorithm. Irregularities of the upper branch of the curve and the fact that by increasing the M parameter of the Carreau equation resulted in narrower distribution, i.e. that the algorithm handled the breadth of the molecular mass distribution inversely, prompted us to try the General Exponential (GEX) function, as suggested by Nobile et al. [9], to describe the molecular mass distribution function. It is to be noted, however, that only monomodal distributions with a single peak can be described by the GEX function, shown in Equation (26):

$$f_{GEX}(M;\, a, b, M_0) = \frac{b}{M_0 \Gamma\left(\frac{a+b}{b}\right)} \cdot \left(\frac{M}{M_0}\right)^a \cdot e^{-\left(\frac{M}{M_0}\right)^b} \tag{26}$$

where $\Gamma(x)$ is the gamma function, a and b are constants, M is the mass average molecular mass, M_0 is the reference molecular mass.

The starting point is again the experimentally determined shear viscosity function and the four parameters of the Carreau equation (η_0, λ, M and N) fitted to the experimental points.

The rheological model is defined by a 5-parameter ($\eta_{0,GEX}$, K_{3GEX}, a_{GEX}, b_{GEX} and α_{GEX}) GEX function shown in Equation (28), derived from the assumed form of the molecular mass distribution function (see Equation (27)):

$$\left(\frac{\eta}{\eta_{0,GEX}}\right)^{1/\alpha} = 1 + \frac{\frac{K_3}{\dot{\gamma}^{1/\alpha}} \cdot \Gamma\left(\frac{a+1}{b}, \left[\frac{K_3}{\dot{\gamma}^{1/\alpha}}\right]^b\right) - \Gamma\left(\frac{a+2}{b}, \left[\frac{K_3}{\dot{\gamma}^{1/\alpha}}\right]^b\right)}{\Gamma\left(\frac{a+2}{b}\right)} \tag{27}$$

where $\Gamma(x, y)$ in the incomplete gamma function given by Equation (28):

$$\Gamma(x, y) = \Gamma(x) - \int_0^y t^{x-1} \cdot e^{-t} \mathrm{d}t \tag{28}$$

and $a, b > 0$. Notations introduced by Nobile et al. [9] are used in the equations.

6.2. Calculation of the molecular mass distribution

The parameters are calculated by fitting Equation (27) to the experimental data using nonlinear regression method.

M_1 and M_0 molecular masses necessary for the further calculation are obtained knowing two further parameters – K_1 and K_2 – defined by Equations (29) and (30):

$$M_1 = \left(\frac{\eta_0}{K_1}\right)^{1/\alpha} \tag{29}$$

$$M_0 = \frac{1}{K_3 K_2^{1/\alpha}} \tag{30}$$

Molecular mass data of the distribution function are obtained according to Equation (22) where η_0 is the maximum shear viscosity, K is a polymer-specific constant, λ is the relaxation time, $\dot{\gamma}$ is the actual shear rate and $k = 1$. The corresponding $w(m)_{GEX}$ values are obtained form Equation (26). Of course theses should be normalized according to the $\Sigma w_i m_i = 1$ relation.

The algorithm was tested with PS/PVC/PP samples and it turned out that the calculated distribution curves approximate best those obtained by GPC if $a < b$ and $K_1 = K_2 = 1–2.25$.

6.3. Results and discussion. Comparison of the calculated and measured molecular mass distribution

Figures 8–10 show the molecular mass distribution curves obtained by the GPC method and calculated from shear viscosity function for one PS, PVC a PP sample.

Table 8 presents the constants calculated by the GEX-model for the polymers included in this study, $\overline{M}_m$, $\overline{M}_n$ and $\overline{M}_m/\overline{M}_n$ values, which are compared with those obtained form the GPC tests. Both molecular mass and the distribution values exhibit (with some exceptions) less than 30% deviation, in the majority of the cases the difference is less than 10%. Based on these results we can conclude that using the model suggested by us it is possible (within the mentioned limits) it is possible to predict the molecular mass distribution from the rheological data. Individual constants are valid for each polymer, which cannot be predicted on generalized at the present sate of knowledge.

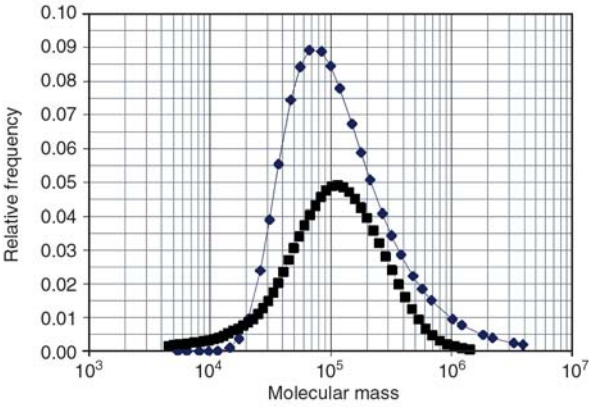

Figure 8. GPC curve of the PS-4 sample (■) and the molecular mass distribution calculated by the GEX function (♦)

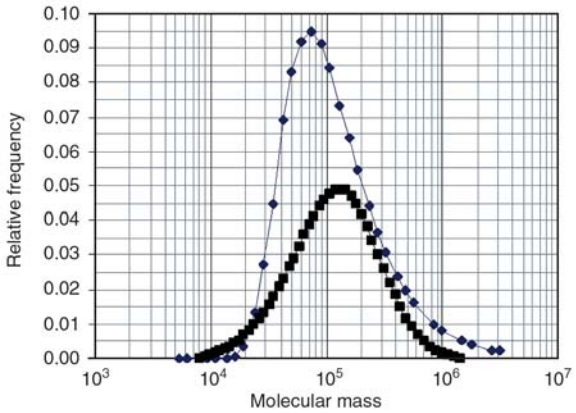

Figure 9. GPC curve of the PVC-4 sample (■) and the molecular mass distribution calculated by the GEX function (♦)

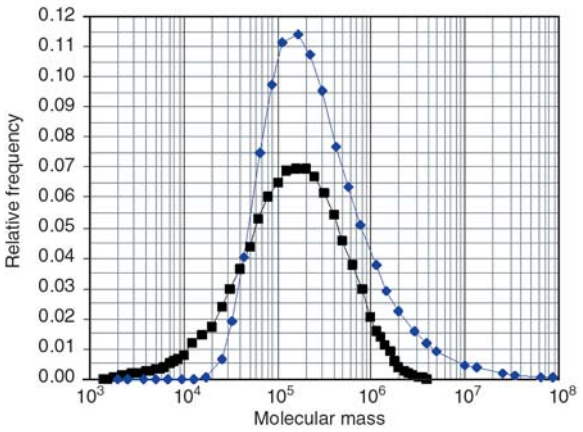

Figure 10. GPC curve of the PP-3 sample (■) and the molecular mass distribution calculated by the GEX function (♦)

6.4. Critical evaluation of the applicability of the model

Taking into account that the breadth of the molecular mass distribution functions of the polymers studied is moderate, it was investigated, whether a systematic variation of the Carreau parameters is reflected in the shape of the GEX distribution function and if yes, how. Therefore four cases were investigated, namely

– η_0 is varied, λ = constant, M = constant, and N = constant;
– λ is varied, η_0 = constant, M = constant and N = constant;
– M is varied, η_0 = constant, λ = constant and N = constant;
– N is varied, η_0 = constant, λ = constant and M = constant.

Positive features of the model are as follows:

(1) The increase/decrease of the maximum shear viscosity shifts the curve upwards/downwards along the molecular mass axis, the width of the distribution curve remains constant.

Table 8. A comparison of the constants of polymers calculated by the GEX model and those obtained from molecular mass distributions calculated from GPC test results

Polymer type	Calculated from the GEX model			Calculated from GPC tests			Relative difference* [%]		
	$\overline{M}_m$	$\overline{M}_n$	$\overline{M}_m/\overline{M}_n$	$\overline{M}_m$	$\overline{M}_n$	$\overline{M}_m/\overline{M}_n$	$\overline{M}_m$	$\overline{M}_n$	$\overline{M}_m/\overline{M}_n$
EDISTIR polystyrene									
PS–1	152776	60371	2.531	162634	64072	2.538	–6.06	–5.78	–0.29
PS–2	157475	52744	2.986	157532	58431	2.696	–0.04	–9.73	10.76
PS–3	171824	50492	3.404	160375	62151	2.580	7.14	–18.76	31.92
PS–4	191971	77761	2.469	176472	71525	2.467	8.78	8.72	0.07
PS–5	194411	61010	3.187	189487	88165	2.149	2.60	–30.80	48.29
PS–6	294751	108468	2.717	158968	58993	2.695	85.42	83.87	0.83
PS–7	156055	77134	2.023	131583	59117	2.226	18.60	30.48	–9.11
PS–8	177085	53343	3.320	150708	55342	2.723	17.50	–3.61	21.91
PS–9	216028	104523	2.067	187972	65438	2.873	14.93	59.73	–28.04
PS–10	150428	72491	2.075	150680	55797	2.701	–0.17	29.92	–23.16
PS–11	150765	88534	1.703	150798	53184	2.835	–0.02	66.47	–39.94
ONGROLIT PVC									
PVC-1	95600	48710	1.963	80035	40049	1.998	19.45	21.63	–1.77
PVC-2	92630	47868	1.935	106986	52384	2.042	–13.42	–8.62	–5.26
PVC-3	144287	55992	2.577	145541	68544	2.123	–0.86	–18.31	21.37
PVC-4	173043	78244	2.212	164508	80261	2.050	5.19	–2.51	7.92
PVC-5	191003	97504	1.959	188065	87418	2.151	1.56	11.54	–8.94
PVC-6	335544	148623	2.258	253923	114367	2.220	32.14	29.95	1.70
TIPPLEN polypropylene									
PP-1	125357	29412	4.262	121850	45274	4.701	2.88	–35.04	–9.34
PP-2	236460	53324	4.434	219166	46200	4.744	7.89	15.42	–6.53
PP-3	274656	63092	4.353	269912	55980	4.822	1.76	12.70	–9.72
PP-4	305930	58660	5.215	336073	68097	4.935	–8.97	–13.86	5.67
PP-5	526139	111638	4.713	480786	89048	5.399	9.43	25.37	–12.71
PP-6	762101	122382	6.227	617606	107993	5.719	23.40	13.32	8.88

*relative difference = 100 · (calculated from rheological tests – obtained from GPC tests)/(obtained from GPC tests)

(2) An increase of the relaxation time results in broader distribution while a decrease leads to a narrower distribution.

(3) Increasing N intensifies the non-Newtonian character and results in a broader distribution, while its decrease causes a more Newtonian character and a narrower distribution function.

Negative characteristics of the model are that

(1) it can predict only narrow and moderately broad ($1.5 < \overline{M}_m/\overline{M}_n < 6$) distributions,

(2) the variation of M does not cause a significant change in the shape of the distribution function.

7. Conclusions

Determining the number- and mass distribution of commercial polystyrene, PVC and polypropylene samples by GPC method the constants of the distribution functions were calculated. From the shear viscosity function measured at 190°C by capillary viscometry the Carreau constants of the polymers were calculated. Equations for the maximum shear viscosity and the mass average molecular mass taken form the literature were compared with our experimental data.

(1) The basic assumption of our model developed to a transform molecular mass distribution to shear viscosity function (direct problem) is that for each shear rate there is a M_c critical molecular mass. At $M < M_c$ the molecules contribute to the shear viscosity according to the w_iM_i product, while at $M \geq M_c$ according to their mass fraction, as if their molecular mass were M_c. It is assumed further that the threshold value is independent of the average molecular mass of the sample and of the molecular mass distribution of the whole sample. Measured and calculated shear viscosity functions of the samples mentioned above agree within 10% error limit.

(2) In order to determine the molecular mass distribution function from the shear viscosity function measured by capillary viscometry (inverse problem) we used the shear viscosity function

of a two component polymer mixture developed by Bersted. Although the breadth of the distribution functions calculated by the modified Carreau equation approximates well the data derived form the GPC curves, the actual shape of the calculated distribution function and the deviation of measured and calculated mass and number average molecular masses is too high, therefore this model was not developed further.

(3) In order to solve the inverse problem, i.e. for the prediction of the molecular mass distribution a model using the so-called GEX (General Exponential) function is suggested. The rheological model derived from the mathematical form of the distribution function assumed by Nobile is described by a 5-parameter GEX function. Having checked the validity of the model with a large number of polymer samples we concluded that it is possible to predict the molecular mass distribution from the rheological data with an accuracy of ±30%. Individual constants are valid for every polymer, which cannot be generalized at our present state of knowledge.

The positive features of the model include that an increase/decrease of the maximum shear viscosity shifts the curve upwards/downwards the distribution function wile the breadth of the distribution remains constant; the increase of the relaxation time leads to a broader, its increase to a narrower distribution; an increase of N increases the non-Newtonian character and broadens the distribution function, while its decrease decreases the non-Newtonian character and narrows down the distribution function.

Negative features of the model include that it can predict only marrow to medium ($1.5 < \overline{M}_m/\overline{M}_n < 6$) distributions and a variation of M does not cause a significant change in the shape of the distribution function.

(4) By solving the inverse problem a fast, but scientifically correct method is available for estimating the molecular mass distribution from macroscopic flow data without recourse to a lengthy dissolution process and a GPC test demanding expensive equipment and considerable experience.

Acknowledgements

The research described here has been performed at the Research Institute for Plastics with the financial support of OTKA T 31898 project 'Relations between polymer structure, molecular mass distribution and viscosity function of thermoplastics'.

References

[1] Bersted B.: An empirical model relating the molecular weight distribution of high-density polyethylene to the shear dependence of the steady shear melt viscosity. Journal of Applied Polymer Science, **19**, 2167–2177 (1975).
DOI: 10.1002/app.1975.070190810

[2] Bersted B.: A model relating the elastic properties of high-density polyethylene melts to the molecular weight distribution. Journal of Applied Polymer Science, **20**, 2705–2714 (1976).
DOI: 10.1002/app.1976.070201008

[3] Bersted B. H., Slee J. D.: A relationship between steady-state shear melt viscosity and molecular weight distribution in polystyrene. Journal of Applied Polymer Science, **21**, 2631–2634 (1977).
DOI: 10.1002/app.1977.070211006

[4] Malkin A. Ya., Teishev A. E.: Is it possible to determine the molecular mass distribution of a polymer in a unique fashion from the flow curve of its melt? Vysokomolekularnye Soedinenia A, **29**, 2230–2234 (1987).

[5] Malkin A. Ya., Teishev A. E.: Method of determination of molecular mass disribution from curves of polymer melt flow. Vysokomolekularnye Soedinenia A, **30**, 175–178 (1988).

[6] Malkin A. Ya., Teishev A. E.: Flow curve – molecular weight distribution: Is the solution of the inverse problem possible? Polymer Engineering Science, **31**, 1590–1596 (1991).
DOI: 10.1002/pen.760312206

[7] Tuminello W. H., Cudré-Maurox N.: Determining molecular weight distributions from viscosity versus shear rate flow curves. Polymer Engineering and Science, **31**, 1496–1507 (1991).
DOI: 10.1002/pen.760312009

[8] Shaw M. T., Tuminello W. H.: A closer look at the *MWD*-viscosity transform. Polymer Engineering and Science, **34**, 159–165 (1994).
DOI: 10.1002/pen.760340213

[9] Nobile M. R., Cocchini F., Lawler J. V.: On the stability of molecular weight distributions as computed from the flow curves of polymer melts. Journal of Rheology, **40**, 363–382 (1996).
DOI: 10.1122/1.550748

[10] Provder T., Kuo C. Y.: Recent advances in size exclusion chromatography. Plenum Press, New York (1983).

[11] Berry G. C., Fox T. G.: The viscosity of polymers and their concentrated solutions. Advances Polymer Science, **5**, 261–357 (1968).
DOI: 10.1007/BFb0050985

[12] Carreau P. J., De Kee D., Daroux M.: An analysis of the viscous behavior of polymeric solutions. The Canadian Journal of ChemicalEngineering, **57**, 135–141 (1979).

[13] Combs R. L., Slonaker D. F., Coover H. W.: Effects of molecular weight distribution and branching on rheological properties of polyolefin melts. Journal of Applied Polymer Science, **13**, 519–534 (1969).
DOI: 10.1002/app.1969.070130312

[14] Gahleitner M., Sobczak R.: Bedeutung der Nullviskositätsbestimmung für das Modellieren von Fliesskurven. Kunststoffe, **79**, 1213–1216 (1989).

[15] Gahleitner M., Bihlmayer G., Sobczak R.: Modifiziertes Carreau-modell. Kunststoffe, **81**, 651–653 (1991).

[16] Mendelson R. A., Bowles W. A., Finger F. L.: Effect of molecular structure on polyethylene melt rheology I: Low-shear behavior. Journal of Polymer Science Part A2: Polymer Physics, **8**, 105–126 (1970).
DOI: 10.1002/pol.1970.160080109

[17] Zosel A.: Der Einfluss von Molekulargewicht und Molekulargewichtsverteilung auf die viskoelastischen Eigenschaften von Polystyrolschmelzen. Rheologica Acta, **10**, 215–224 (1971).
DOI: 10.1007/BF02040445

[18] Frank H. P.: Rheologische Messungen an Polypropylenschmelzen. Rheologica Acta, **5**, 89–93 (1966).

[19] Shroff R. N., Shida M.: Correlation between steady state flow curve and molecular weight distribution for polyethylene melts. Polymer Engineering and Science, **11**, 200–204 (1971).
DOI: 10.1002/pen.760110306

[20] Graessley W. W., Segal L.: Effect of molecular weight distribution on the shear dependence of viscosity in polymer systems. AIChE Journal, **16**, 261–267 (1970).
DOI: 10.1002/aic.690160219

[21] Halász L., Vorster O., Vincze Á.: Relaxation spectrum calculation methods and their use to determine the molecular mass distribution of propylene, ethylene and alfa-olefin copolymers. Progress in Colloid and Polymer Science, **125**, 155–160 (2004).
DOI: 10.1007/b13435

[22] Borg T., Pääkkönen E. J.: Linear viscoelastic models: Part II. Recovery of the molecular weight distribution using viscosity data. Journal of Non-Newtonian Fluid Mechanics, **156**, 129–138 (2009).
DOI: 10.1016/j.jnnfm.2008.07.010

[23] Friedman E. M., Porter R. S.: Polymer viscosity-molecular weight distribution correlation via blending. Transactions of the Society of Rheology, **49**, 493–508 (1975).